

Composition And Pressure Dependent Study Of The Weyl

Semimetal $\text{Mo}_{1-x}\text{W}_x\text{Te}_2$

by
Rabin Dahal

A dissertation submitted to the Department of Physics,
College of Natural Sciences and Mathematics
in partial fulfillment of the requirements for the degree of

Doctor of Philosophy
in Physics

Chair of Committee: Ching-Wu Chu

Committee Member: Zhifeng Ren

Committee Member: Shuo Chen

Committee Member: Pavan R Hosur

Committee Member: Jiming Bao

University of Houston
December 2020

Copyright 2020, Rabin Dahal

ACKNOWLEDGMENTS

I can still vividly remember the day I was accepted to work in the High Pressure and Low Temperature research group. I had great zeal and was very enthusiastic about this opportunity. In the past four years, my research group has provided me with great learning experiences and has helped me grow both professionally and personally. It has been an incredible journey and I feel greatly indebted to everyone who helped me on this journey.

First and foremost, I would like to express my sincere gratitude to my supervisor Dr. Paul C. W. Chu for his continued guidance and supervision throughout my Ph.D. research. Dr. Chu encouraged me to widen the boundaries of my research interests and allowed me to expand my creativity in the field. I am very thankful to the members of my dissertation committee, Dr. Zhifeng Ren, Dr. Shuo Chen, Dr. Pavan Hosur, and Dr. Jiming Bao, whose insightful comments and suggestions have been of immense value for my research work. I would like to give special thanks to Dr. Liangzi Deng for his continuous help and advice throughout the past few years. Dr. Deng taught me the high-pressure DAC technique and helped me during manuscript preparation, as well as generously providing guidance and direction in different aspects of my research. I am also thankful to Dr. Zheng Wu, who guided me in sample preparation and LabVIEW programming and was always willing to help me with setting up experiments. I would like to extend my gratitude to Dr. Melissa Gooch for assisting me in low-temperature techniques and manuscript preparation. I am equally indebted to Dr. Narayan Poudel for teaching me the BeCu clamp cell technique. I would like to thank Troy Christensen for helping me edit my manuscript

and dissertation. I extend my sincere gratitude to our group members Dr. Hung-Cheng Wu, Dr. Hanming Yuan, Dr. Shuyuan Huyan, Dr. Yan-Feng Lyu, Dr. Luke Mastalli-Kelly, Moein Adnani, Samira Daneshmandi, and Trevor Bontke for their warm support and help. Last but not the least, I am forever grateful to my loving family: my parents, for always being my source of inspiration, and my loving wife Sanju, for her unyielding support and love.

ABSTRACT

In this work, the doping and pressure effects on the Weyl semimetal $\text{Mo}_{1-x}\text{W}_x\text{Te}_2$ have been investigated. A series of single crystals of $\text{Mo}_{1-x}\text{W}_x\text{Te}_2$ for $x = 0, 0.10, 0.30, 0.40, 0.50, 0.70, 0.75, 0.90,$ and 1 were synthesized using the self-flux method (for parent compounds MoTe_2 and WTe_2) and the chemical vapor transport method (for doped compounds). The single crystals were then characterized by energy-dispersive X-ray spectroscopy and X-ray diffraction (XRD). Temperature-dependent resistivity measurements at ambient pressure show metallic behavior for all doping levels. Transverse magnetoresistance (MR) measurements show that the parent compounds exhibit large non-saturating MR, which might result from electron-hole compensation, whereas the doped compounds have low MR values, indicating doping-induced electron-hole asymmetry. Doping-dependent resistivity measurements up to 650 K at ambient pressure reveal that the structural transition temperature (T_s) increases linearly with increasing W content in $\text{Mo}_{1-x}\text{W}_x\text{Te}_2$. The observed T_s of MoTe_2 at ambient pressure is 249 K and that of WTe_2 is 613 K. Temperature-dependent synchrotron XRD measurements further confirm the structural transition in WTe_2 at ambient pressure. Pressure was found to continuously suppress the T_s in $\text{Mo}_{0.90}\text{W}_{0.10}\text{Te}_2$, $\text{Mo}_{0.60}\text{W}_{0.40}\text{Te}_2$, and $\text{Mo}_{0.25}\text{W}_{0.75}\text{Te}_2$, and superconductivity emerges in $\text{Mo}_{0.90}\text{W}_{0.10}\text{Te}_2$ and $\text{Mo}_{0.60}\text{W}_{0.40}\text{Te}_2$ above 1.25 K when T_s is suppressed to a lower temperature. Magnetotransport measurements of $\text{Mo}_{0.50}\text{W}_{0.50}\text{Te}_2$ under pressure reveal that, at a critical pressure of 0.9 GPa, the transverse MR is suppressed, the Hall coefficient changes sign, and superconductivity emerges, suggesting a significant reconstruction of the Fermi surface. The superconducting transition temperature (T_c) continuously increases with increasing pressure above 0.9 GPa up to 14.3 GPa.

With further increasing pressure above 14.3 GPa, the T_c remains constant and then begins to decrease monotonically at 17.5 GPa. This work demonstrates that both the structural transition and superconductivity in $\text{Mo}_{1-x}\text{W}_x\text{Te}_2$ are tunable by changing the W composition and physical pressure.

TABLE OF CONTENTS

ACKNOWLEDGMENTS	iii
ABSTRACT	v
LIST OF FIGURES	xii
LIST OF TABLES	xiii
1 Introduction	1
2 Background	5
2.1 Weyl Fermions	5
2.2 Weyl Semimetal	7
2.2.1 Weyl Node and Fermi Arc	9
2.2.2 Chiral Anomaly	11
2.2.3 Positive Transverse Magnetoresistance	16
2.2.4 Symmetry Breaking in Weyl Semimetal	17
2.3 Types of Weyl Semimetal	19
2.4 Transition Metal Dichalcogenides: $\text{Mo}_{1-x}\text{W}_x\text{Te}_2$	19
3 Experimental Methods	23
3.1 Single Crystal Growth	23
3.1.1 Flux Method	23
3.1.2 Chemical Vapor Transport Method	26
3.2 Elemental Composition Analysis	29
3.3 X-ray Diffraction	30
3.4 Transport Measurements	30
3.4.1 Magneto-Transport Measurements	30
3.4.2 High Temperature Resistivity Measurements	31
3.5 High-Pressure Study	33
3.5.1 Beryllium-Copper Clamp Cell	33
3.5.2 Diamond Anvil Cell	38
4 Results	43

4.1	Elemental Analysis using Energy-Dispersive X-ray Spectroscopy . . .	44
4.2	X-ray Diffraction Patterns	46
4.3	Magnetotransport Properties	48
4.4	Structural Transition at Ambient Pressure	53
4.5	High-Pressure Study using Beryllium-Copper Clamp Cell	60
4.6	High-Pressure Study using Diamond Anvil Cell	71
5	Conclusion	79
A	Superconductivity of Lead Under Pressure	82
	Bibliography	85

LIST OF FIGURES

2.1	A Weyl semimetal with two Weyl nodes (blue and red points). A Weyl node can be considered as a magnetic monopole (MMP) in momentum space. The figure is adopted from the reference [1].	10
2.2	ARPES Fermi surface map of the Fermi arcs (a) TaAs [2] (b) NbAs [3].	11
2.3	Illustration of the chiral anomaly of Weyl fermions based on a Landau level spectrum. (Top panel) Equilibrium energy spectrum of the left-handed (L) and right-handed (R) fermions under a magnetic field \mathbf{B} . Empty states with positive energy are shown by gray dots and filled states with negative energy are shown by black dots. (Bottom panel) Same spectrum in the presence of parallel magnetic field \mathbf{B} and electric field \mathbf{E} . The electrons are displaced from their equilibrium position by $\delta k \sim -\mathbf{E}$ resulting the production of left-handed antiparticles and right-handed particles [4].	15
2.4	A 3D Dirac-cone point (DCP) can be driven into two Weyl nodes with opposite chirality by time-reversal symmetry breaking (TRB) or four Weyl nodes by inversion symmetry breaking (ISB) [1].	18
2.5	Two types of Weyl semimetals. In type-I Weyl semimetal, valence band and conduction band form a point like Fermi surface. In type-II WSM, due to the strong tilting of the Weyl cone, a Weyl point appears at the touching point between electron and hole pockets. The figure is adopted from the reference [5].	20
3.1	Schematic of Chemical Vapor Transport (CVT) method with source materials at temperature T_2 and crystal growth zone at T_1	27
3.2	(a) A real picture and (b) schematic drawing of high temperature resistivity measurement probe.	31
3.3	A photograph of the high-pressure beryllium-copper clamp cell. . . .	36
3.4	Schematic drawing of the high-pressure beryllium-copper (BeCu) clamp cell.	37
3.5	(a) A real picture and (b) schematic drawing of diamond anvil cell (DAC).	39

3.6	Schematic drawing of preindented gasket area with a sample, four platinum electrodes, and a Ruby piece. The electrodes are used for resistivity and Hall measurements by the van der Pauw method. . . .	40
3.7	(a) A picture of DAC after connecting with a puck and (b) schematic drawing of the puck connections for van der Pauw resistivity measurement using ACT option from the PPMS. The wires A, B, C, and D are connected to the corresponding platinum electrodes in Figure 3.6.	42
4.1	Plot of nominal composition x vs composition x from EDS measurements for $\text{Mo}_{1-x}\text{W}_x\text{Te}_2$ single crystals. $y = x$ is the reference line passing through the origin. Except for $\text{Mo}_{0.60}\text{W}_{0.40}\text{Te}_2$ and $\text{Mo}_{0.25}\text{W}_{0.75}\text{Te}_2$, the composition from EDS measurement is close to the nominal composition.	45
4.2	(a) X-ray diffraction (XRD) patterns from 10 to 90 degrees, (b) magnified view of the (002) XRD peaks, and (c) lattice parameter (c) vs composition (x) for $\text{Mo}_{1-x}\text{W}_x\text{Te}_2$ single crystals ($x = 0, 0.10, 0.30, 0.40, 0.50, 0.60, 0.70, 0.75, 0.90,$ and 1).	47
4.3	(a) Temperature-dependent resistivity from 300 K down to 2 K and (b) composition-dependent residual resistivity ratio (RRR) ($RRR = \rho(300\text{ K})/\rho(2\text{ K})$) of $\text{Mo}_{1-x}\text{W}_x\text{Te}_2$ for $x = 0, 0.10, 0.30, 0.40, 0.50, 0.60, 0.70, 0.75, 0.90,$ and 1 . The anomaly in the resistivity curve for each of $x = 0$ and 0.10 in (a) corresponds to a structural transition.	49
4.4	Magnetic field effects on WTe_2 with current along the a axis and magnetic field parallel to the c axis. (a) Temperature-dependent resistivity without and with magnetic field of 7 T. (b) Field-dependent MR at 2 K. Inset: quantum oscillations demonstrate the high quality of the crystal.	50
4.5	(a) Temperature-dependent resistivity without and with magnetic field of 7 T and (b) field dependence of MR up to 7 T at 2 K for MoTe_2 with current parallel to a axis and magnetic field perpendicular to ab plane.	51
4.6	Magnetic field effects in single-crystalline $\text{Mo}_{1-x}\text{W}_x\text{Te}_2$. The electric current is applied parallel to the a axis and the magnetic field is along the c axis. (a) Temperature-dependent resistivity without and with magnetic field of 7 T in $\text{Mo}_{0.50}\text{W}_{0.50}\text{Te}_2$. Inset: low-temperature data show that the resistivity increases under field. (b) Field dependence of MR up to 7 T and at 2 K in $\text{Mo}_{1-x}\text{W}_x\text{Te}_2$ for $x = 0.10, 0.30, 0.50, 0.70,$ and 0.90	52

4.7	Temperature-dependent electrical resistivity during cooling and warming cycles for (a) MoTe_2 from 2 K to 300 K and (b) $\text{Mo}_{0.90}\text{W}_{0.10}\text{Te}_2$ from 2 K to 390 K. Insets: anomaly with thermal hysteresis associated with the structural transition from the monoclinic $1T'$ phase to the orthorhombic T_d phase.	55
4.8	Electrical resistivity as a function of temperature during cooling and warming cycles for (a) $\text{Mo}_{0.70}\text{W}_{0.30}\text{Te}_2$ from 2 K to 390 K and (b) $\text{Mo}_{0.50}\text{W}_{0.50}\text{Te}_2$ from room temperature to 470 K. Insets: anomaly with thermal hysteresis associated with the structural transition from the monoclinic $1T'$ phase to the orthorhombic T_d phase.	56
4.9	The plot of electrical resistivity as a function of temperature during cooling and warming cycles for (a) $\text{Mo}_{0.30}\text{W}_{0.70}\text{Te}_2$ from room temperature to 590 K and (b) $\text{Mo}_{0.10}\text{W}_{0.90}\text{Te}_2$ from room temperature to 620 K. Insets: anomaly with thermal hysteresis associated with the structural transition from the monoclinic $1T'$ phase to the orthorhombic T_d phase.	57
4.10	(a) Electrical resistivity as a function of temperature during cooling and warming cycles for WTe_2 from room temperature to 650 K. Insets: anomaly with thermal hysteresis associated with the structural transition from the monoclinic $1T'$ phase to the orthorhombic T_d phase. (b) Variation of structural transition temperature T_s with doping from resistivity measurements of $\text{Mo}_{1-x}\text{W}_x\text{Te}_2$. T_s is defined as the maxima of $d\rho/dT$ during the cooling cycles.	58
4.11	Synchrotron XRD patterns for WTe_2 for 2θ (a) from 5 to 45 degrees and (b) from 13.5 to 17.5 degrees at different temperatures.	59
4.12	High-pressure effects on $\text{Mo}_{0.90}\text{W}_{0.10}\text{Te}_2$. (a) Electrical resistivity as a function of temperature for different pressures in the range of 0–17.71 kbar. Resistivity curves are shifted vertically for clarity. The anomaly in the resistivity corresponds to the structural transition from the monoclinic $1T'$ phase to the orthorhombic T_d phase. Inset: low-temperature data. (b) Pressure-dependent structural and superconductivity transition temperatures (red and blue spheres, respectively).	63
4.13	Temperature-dependent resistivity of $\text{Mo}_{0.90}\text{W}_{0.10}\text{Te}_2$ under (a) 0 kbar, (b) 3.89 kbar, (c) 8.98 kbar, (d) 13.52 kbar, and (e) 17.71 kbar. Anomalies with thermal hysteresis under 0 kbar, 3.89 kbar, 8.98 kbar, and 13.52 kbar are associated with structural transitions.	64

4.14	High-pressure effects on $\text{Mo}_{0.60}\text{W}_{0.40}\text{Te}_2$. (a) Electrical resistivity as a function of temperature for different pressures in the range of 0–16.66 kbar. Resistivity curves are shifted vertically for clarity. The anomaly in the resistivity corresponds to the structural transition from the monoclinic $1T'$ phase to the orthorhombic T_d phase. Inset: low-temperature data. (b) Pressure-dependent structural and superconducting transition temperatures (red and blue spheres, respectively).	65
4.15	Evolution of structural transition under pressure on $\text{Mo}_{0.60}\text{W}_{0.40}\text{Te}_2$. Temperature-dependent resistivity under (a) 0 kbar, (b) 3.28 kbar, (c) 8.35 kbar, (d) 12.50 kbar, and (e) 16.66 kbar. Anomalies with thermal hysteresis under 3.28 kbar, 8.35 kbar, 12.50 kbar, and 16.66 kbar are associated with structural transitions.	66
4.16	(a) Electrical resistivity of single-crystalline $\text{Mo}_{0.25}\text{W}_{0.75}\text{Te}_2$ as a function of temperature for different pressures in the range of 0–17.05 kbar. Resistivity curves are shifted vertically for clarity. (b) Pressure-dependent structural transition temperatures of $\text{Mo}_{0.25}\text{W}_{0.75}\text{Te}_2$.	67
4.17	Temperature-dependent resistivity of $\text{Mo}_{0.25}\text{W}_{0.75}\text{Te}_2$ under (a) 0 kbar, (b) 2.98 kbar, (c) 8.44 kbar, (d) 12.32 kbar, and (e) 17.05 kbar. Anomalies with thermal hysteresis under 12.32 kbar and 17.05 kbar are associated with structural transitions.	68
4.18	(a) Electrical resistance as a function of temperature for $\text{Mo}_{0.50}\text{W}_{0.50}\text{Te}_2$ under pressures ranging from 1.1 to 42.3 GPa. Electrical resistance below 8 K under pressures of (b) 1.1 – 14.3 and (c) 14.3 – 42.3 GPa. Drops in the electrical resistance and zero-resistance behavior are both clearly observed.	73
4.19	Upper critical field (H_{c2}) analysis of the superconducting $\text{Mo}_{0.50}\text{W}_{0.50}\text{Te}_2$. Temperature dependence of electrical resistance under different magnetic fields up to 2 T under (a) 5.9 GPa and (b) 14.3 GPa. (c) H_{c2} as a function of temperature under different pressures. Solid lines are the linear fits of the experimental data.	74
4.20	Magnetic-field-dependent (a) MR and (b) Hall resistivity of $\text{Mo}_{0.50}\text{W}_{0.50}\text{Te}_2$ under different pressures at 10 K.	75
4.21	Phase diagram of $\text{Mo}_{0.50}\text{W}_{0.50}\text{Te}_2$ under pressure. (a) T_c (left axis) and MR at 10 K under magnetic field of 7 T (right axis) plotted against pressure for different runs of pressure loading and unloading. (b) Pressure loading and unloading for pressure-dependent Hall coefficient (R_H) at 10 K.	76

LIST OF TABLES

4.1	Nominal compositions and compositions determined by energy-dispersive X-ray spectroscopy (EDS) for $\text{Mo}_{1-x}\text{W}_x\text{Te}_2$ ($x = 0, 0.10, 0.30, 0.40, 0.50, 0.70, 0.75, 0.90,$ and 1).	45
4.2	Compositions and corresponding structural transition temperature (T_s) values determined by resistivity measurements.	54
4.3	The upper critical field determined by using Werthamer-Helfand-Hohenberg (WHH) approximation at different pressures.	72
A.1	Table showing change in superconducting transition temperature of lead under pressure.	83
A.2	Table A.1 continued.	84

Chapter 1

Introduction

The materials whose properties remain invariant under topological transformation are called topological materials. The recent discovery of exotic properties in topological materials has generated tremendous research interests in this field. Among the different classes of topological materials, topological insulators and topological Weyl semimetals are being extensively studied in experimental condensed matter research [2, 6–9]. In a topological insulator, topological properties are protected by the energy gap in the bulk state. Unlike the topological insulator, Weyl semimetal is no longer constrained by a bulk energy gap that protects the topological nature of the energy bands [1]. Due to this new type of topological nontrivial phase, a Weyl semimetal is a good platform to study and manipulate novel topological quantum states with a promising device application potentials.

Weyl fermions are massless chiral fermions proposed by Herman Weyl in 1929 in high energy physics [10]. For a long time, neutrino was thought as a candidate for massless Weyl fermions. However, after the discovery of the mass of neutrino [11], it

was discarded as a candidate for Weyl fermion. The Weyl fermion as a fundamental particle has not been detected yet in high energy physics [9]. Recently, the concept of Weyl fermions has been applied to condensed matter physics and Weyl fermions as quasiparticles have been detected in semimetals [1]. Weyl fermions can be realized by breaking either time-reversal symmetry or inversion symmetry in Dirac semimetals. A semimetal that contains separated Weyl nodes is called a Weyl semimetal.

A Weyl semimetal contains Weyl nodes with opposite chirality and a Weyl node acts as a momentum space monopole which corresponds to a source or a sink of Berry curvature [12]. Weyl points always come in pairs in a Weyl semimetal otherwise the Berry flux becomes divergent. The Weyl points are stable to weak perturbations and are annihilated only in pairs of opposite charges. The arc connecting the projection of two Weyl nodes on the Fermi surface gives a Fermi arc, which is a hallmark of Weyl semimetal and can be observed experimentally by using angle-resolved photoelectron spectroscopy (ARPES) [2, 13]. Weyl semimetal also displays the chiral anomaly, which leads to a negative longitudinal magnetoresistance (MR) and anomalous Hall effect [5].

The Weyl semimetal can be classified into two types: the type-I Weyl semimetal that respects Lorentz symmetry and the type-II Weyl semimetal that violates the Lorentz symmetry [12]. The type-I Weyl semimetal exhibits ideal Weyl cone where valence band and conduction band touch at a point forming a point-like Fermi surface. However, in type-II Weyl semimetal, the Weyl cone is tilted so that a Weyl point is formed when an electron pocket and a hole pocket intersect at the Fermi surface.

The first experimentally verified Weyl semimetal is TaAs, which has been discovered in 2015 through calculations [14, 15] and observing Fermi arc using ARPES [1, 2, 16]. In the same year, Weyl semimetal state also has been discovered in other TaAs class of materials, namely TaP, NbAs, and NbP [3, 13, 17–21]. Bulk band structure of these TaAs class of materials contains ideal Weyl cones and belongs to type-I Weyl semimetal. After the discovery of the Weyl semimetal state in TaAs class of materials, many other materials have been proposed as a candidate for Weyl semimetals and some of them have been verified experimentally. To further explore the novel properties of already discovered Weyl semimetals and search for a new class of Weyl semimetals are prominent research interests in the current scientific community.

MoTe₂ and WTe₂ are experimentally verified type-II Weyl semimetals [22–25] with interesting physical properties [26, 27]. Both of them show large nonsaturating MR at ambient and dome-shaped superconducting behavior under pressure. The type-II Weyl semimetal state also has been observed in Mo_{1-x}W_xTe₂ for $x = 0.75$ and is predicted to have type-II Weyl semimetal state in other doping levels [28].

At ambient pressure, semimetallic MoTe₂ undergoes a structural transition from monoclinic 1T' phase to orthorhombic T_d phase at ~ 250 K [29, 30]. External pressure suppresses the structural transition temperature (T_s) to a lower temperature and superconducting transition temperature (T_c) increases from 0.10 K at ambient to 8.2 K at 11.7 GPa [31–33]. There are no previous reports of structural nor superconducting transition at ambient pressure in WTe₂. In this work, we have done systematic doping dependent study at ambient pressure for Mo_{1-x}W_xTe₂ and obtained the relation

between doping and T_s . Our high pressure study using BeCu pressure cell established relation between pressure, T_s , and superconductivity for $\text{Mo}_{1-x}\text{W}_x\text{Te}_2$. The study of the magnetotransport properties under pressure using diamond anvil cell (DAC) for $\text{Mo}_{0.50}\text{W}_{0.50}\text{Te}_2$ shows the relationship between superconductivity, MR, and Hall coefficient.

In the following, we shall provide an overview of the basic phenomena related to Weyl fermions in Chapter 2, cover the method for sample preparation and measurement techniques in Chapter 3, present our results and discussions in Chapter 4 and finally summarize our work with conclusions in Chapter 5.

Chapter 2

Background

2.1 Weyl Fermions

The Dirac equation for electron with mass m in covariant form is given by [34]:

$$(i\gamma^\mu \partial_\mu - m)\psi = 0, \quad (2.1)$$

where ψ is 4-component wave function for electron and γ^μ ($\mu = 0, 1, 2, 3$) are 4×4 matrices. In the equation, we have set the speed of light (c) and reduced Planck constant (\hbar) to unity. The gamma matrices in Weyl representation are [35]:

$$\gamma^0 = \begin{pmatrix} 0 & \mathbb{1} \\ \mathbb{1} & 0 \end{pmatrix} \text{ and } \gamma^i = \begin{pmatrix} 0 & \sigma^i \\ -\sigma^i & 0 \end{pmatrix} \text{ with } i = 1, 2, 3.$$

The σ^i are a set of three 2×2 Pauli matrices and are as follows:

$$\sigma^1 = \begin{pmatrix} 0 & 1 \\ 1 & 0 \end{pmatrix}, \sigma^2 = \begin{pmatrix} 0 & -i \\ i & 0 \end{pmatrix}, \text{ and } \sigma^3 = \begin{pmatrix} 1 & 0 \\ 0 & -1 \end{pmatrix}.$$

For massless particles like Weyl fermions, (2.1) becomes

$$(i\gamma^0 \frac{\partial}{\partial t} + i\gamma^1 \frac{\partial}{\partial x} + i\gamma^2 \frac{\partial}{\partial y} + i\gamma^3 \frac{\partial}{\partial z})\psi = 0. \quad (2.2)$$

Consider $\psi = \begin{pmatrix} \psi_L \\ \psi_R \end{pmatrix}$, where two components vectors ψ_L and ψ_R are called left-handed and right handed Weyl spinors. Using gamma matrices, (2.2) can be written as:

$$i \begin{pmatrix} 0 & \mathbb{1} \\ \mathbb{1} & 0 \end{pmatrix} \begin{pmatrix} \frac{\partial \psi_L}{\partial t} \\ \frac{\partial \psi_R}{\partial t} \end{pmatrix} + i \begin{pmatrix} 0 & \sigma^1 \\ -\sigma^1 & 0 \end{pmatrix} \begin{pmatrix} \frac{\partial \psi_L}{\partial x} \\ \frac{\partial \psi_R}{\partial x} \end{pmatrix} + i \begin{pmatrix} 0 & \sigma^2 \\ -\sigma^2 & 0 \end{pmatrix} \begin{pmatrix} \frac{\partial \psi_L}{\partial y} \\ \frac{\partial \psi_R}{\partial y} \end{pmatrix} + i \begin{pmatrix} 0 & \sigma^3 \\ -\sigma^3 & 0 \end{pmatrix} \begin{pmatrix} \frac{\partial \psi_L}{\partial z} \\ \frac{\partial \psi_R}{\partial z} \end{pmatrix} = 0. \quad (2.3)$$

Simplying,

$$\begin{pmatrix} i \frac{\partial \psi_R}{\partial t} + i\sigma^1 \frac{\partial \psi_R}{\partial x} + i\sigma^2 \frac{\partial \psi_R}{\partial y} + i\sigma^3 \frac{\partial \psi_R}{\partial z} \\ i \frac{\partial \psi_L}{\partial t} - i\sigma^1 \frac{\partial \psi_L}{\partial x} - i\sigma^2 \frac{\partial \psi_L}{\partial y} - i\sigma^3 \frac{\partial \psi_L}{\partial z} \end{pmatrix} = 0, \quad (2.4)$$

which gives

$$\begin{pmatrix} i\partial_t \psi_R + i\nabla \cdot \boldsymbol{\sigma} \psi_R \\ i\partial_t \psi_L - i\nabla \cdot \boldsymbol{\sigma} \psi_L \end{pmatrix} = 0. \quad (2.5)$$

With $\mathbf{p} = -i\nabla$, we have

$$\begin{pmatrix} i\partial_t \psi_R - \mathbf{p} \cdot \boldsymbol{\sigma} \psi_R \\ i\partial_t \psi_L + \mathbf{p} \cdot \boldsymbol{\sigma} \psi_L \end{pmatrix} = 0. \quad (2.6)$$

From which we obtain

$$\begin{aligned} i\partial_t\psi_R &= +\mathbf{p} \cdot \boldsymbol{\sigma}\psi_R; \\ i\partial_t\psi_L &= -\mathbf{p} \cdot \boldsymbol{\sigma}\psi_L. \end{aligned} \tag{2.7}$$

These are known as the Weyls equations for massless Weyl fermions [10].

2.2 Weyl Semimetal

Although the Weyl fermions have not been detected in high energy physics, Weyl fermions as quasiparticles have been experimentally observed in some semimetals.

Consider $H(\mathbf{k})$ is a Hamiltonian for noninteracting electron in a crystal momentum space \mathbf{k} . The eigenvalues equation for Bloch wave-functions $|u(\mathbf{k})\rangle$

$$H(\mathbf{k}) |u(\mathbf{k})\rangle = \epsilon(\mathbf{k}) |u(\mathbf{k})\rangle \tag{2.8}$$

defines the electronic structure [4]. The overlap between an eigenvector at point \mathbf{k} and nearby point $\mathbf{k}+\delta\mathbf{k}$ is

$$\langle u(\mathbf{k})|u(\mathbf{k} + \delta\mathbf{k})\rangle \approx 1 + \delta\mathbf{k} \cdot \langle u(\mathbf{k})| \nabla_{\mathbf{k}} |u(\mathbf{k})\rangle \approx e^{\delta\mathbf{k} \cdot \langle u(\mathbf{k})| \nabla_{\mathbf{k}} |u(\mathbf{k})\rangle}. \tag{2.9}$$

If we define Berry connection as:

$$\mathbf{A}(\mathbf{k}) = -i \langle u(\mathbf{k})| \nabla_{\mathbf{k}} |u(\mathbf{k})\rangle, \tag{2.10}$$

(2.9) becomes

$$\langle u(\mathbf{k})|u(\mathbf{k} + \delta\mathbf{k})\rangle \approx e^{i\mathbf{A}(\mathbf{k}) \cdot \delta\mathbf{k}}. \tag{2.11}$$

The curl of the Berry connection is called the Berry curvature:

$$\boldsymbol{\Omega}(\mathbf{k}) = \nabla_{\mathbf{k}} \times \mathbf{A}(\mathbf{k}). \quad (2.12)$$

The integral of the Berry curvature over the 2-D Fermi surface gives a Chern number χ . Mathematically,

$$\chi = \frac{1}{2\pi} \oint_{FS} \boldsymbol{\Omega}(\mathbf{k}) \cdot d\mathbf{S}(\mathbf{k}). \quad (2.13)$$

Consider a Fermi surface sheet and a nonzero flux of Berry curvature is passing through it. Then by Gauss's law, this Fermi surface must enclose a point source or sink of the Berry curvature. Around the point, the Berry curvature becomes

$$\boldsymbol{\Omega}(\mathbf{k}) = \pm \frac{\mathbf{k}}{2k^3}. \quad (2.14)$$

Using $\boldsymbol{\Omega}(\mathbf{k})$ in (2.13), we get

$$\chi = \pm 1. \quad (2.15)$$

In a crystal, a point source or sink of the Berry curvature corresponds to band touching point of valance and conduction bands in momentum space. When expanded around a pair of band touching points, the Weyl equation (2.7) for crystal momentum \mathbf{k} becomes

$$i\partial_t \psi_{R,L} = H(\mathbf{k}) \psi_{R,L} \quad (2.16)$$

with Hamiltonian

$$\begin{aligned} H(\mathbf{k}) &= \pm \hbar v_F \boldsymbol{\sigma} \cdot \mathbf{k} \\ &= \chi \hbar v_F \boldsymbol{\sigma} \cdot \mathbf{k}. \end{aligned} \quad (2.17)$$

Here, the crystal momentum \mathbf{k} is measured from the band touching point and we have used the relation $\mathbf{p} = \hbar\mathbf{k}$. We have use $\hbar = c = 1$ throughout the calculations, except in the final formula. The equations (2.7) and (2.16) are identical, except that the speed of light, c in (2.7) has been replaced by the velocity of the massless Dirac particles in condensed matter, v_F in (2.16). The chiral charge of the bands touching point in a crystal is identical to the chirality of Weyl fermions, chiral charge $\chi = +1$ corresponds to right-handed (R) and $\chi = -1$ to left-handed (L).

2.2.1 Weyl Node and Fermi Arc

A Weyl semimetal contains points in momentum space that are formed by the crossing of nondegenerate valance and conduction bands. The crossing point is called the Weyl node which is described by the Weyl equation (2.2) [36]. Weyl points in a host crystal are extremely robust and do not require symmetry protection because of the crystal's translational invariance to perturbations [1,37]. Berry curvature, which acts as a magnetic field in momentum space, characterizes the topological entanglement between valance and conduction bands [5]. The Berry curvature becomes singular at Weyl points. Similar to a magnetic monopole corresponds to source or sink of magnetic flux, a Weyl point acts as a monopole in momentum space corresponding to the source or sink of the Berry curvature. A Weyl point is associated with chiral fermion in real space and it behaves like a magnetic monopole in momentum space. In a Weyl semimetal, Weyl points always come in pairs with opposite chirality otherwise the Berry flux becomes divergent.

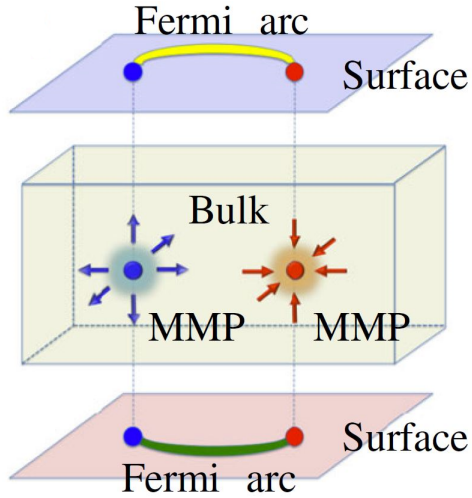


Figure 2.1: A Weyl semimetal with two Weyl nodes (blue and red points). A Weyl node can be considered as a magnetic monopole (MMP) in momentum space. The figure is adopted from the reference [1].

A semimetal with Weyl fermion as a quasiparticle demonstrates bulk-surface correspondence [38]. Due to that, a Weyl semimetal contains a Fermi arc that connects the projection of two bulk Weyl nodes with opposite chirality on a two-dimensional surface. Unlike $2d$ or $3d$ metals, which have usual closed Fermi surfaces, the surface states of a Weyl semimetal are unconventional due to open Fermi arcs [36, 39, 40]. If we consider two Weyl nodes with opposite chirality in a bulk Weyl semimetal in momentum space, one part of a Fermi surface is attached to the top and the other to the bottom and each surface has an open fermi arc [41].

Fermi arcs are strong evidence for identifying Weyl semimetal. Direct observation of the Fermi arc surface states are made by using Angle-Resolved Photoemission Spectroscopy (ARPES) [2, 13]. In the ARPES technique, light is shined on the material and energy, momentum, and spin of the emitted photoelectrons, both from

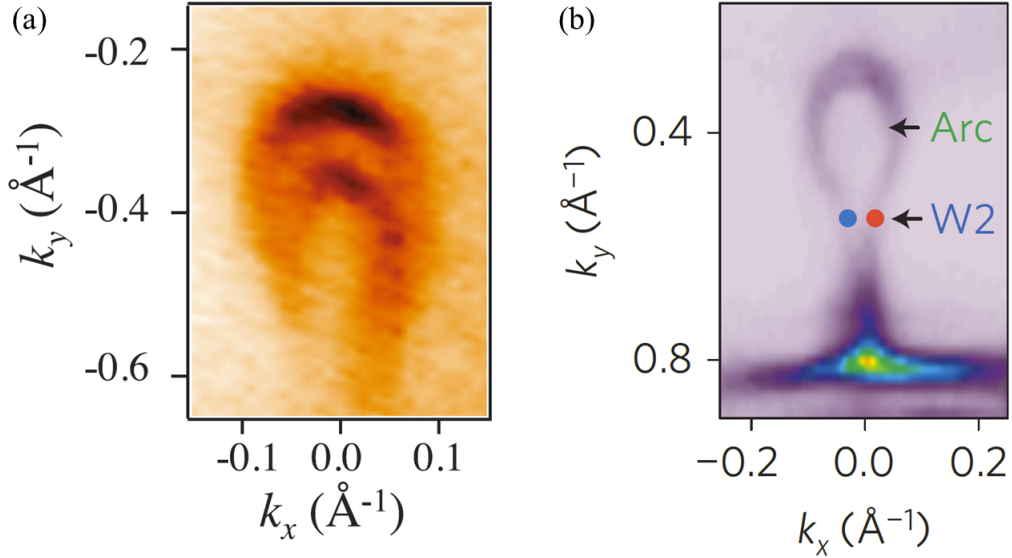


Figure 2.2: ARPES Fermi surface map of the Fermi arcs (a) TaAs [2] (b) NbAs [3].

the surface and the bulk, are measured [9]. Fermi arcs have a contribution to surface quasiparticle interference and hence they can also be observed by using scanning tunneling spectroscopy [42]. It has also been predicted that open Fermi arcs have a contribution to quantum oscillations in the density of states. The density of state oscillations could provide the observable signatures of the surface state in a bulk Weyl semimetal [43–45].

2.2.2 Chiral Anomaly

Let us introduce additional gamma matrix,

$$\gamma^5 = i\gamma^0\gamma^1\gamma^2\gamma^3, \quad (2.18)$$

where matrices γ^0 , γ^1 , γ^2 , and γ^3 are as defined in section (2.1). In block-diagonal form,

$$\gamma^5 = \begin{pmatrix} -\mathbb{1} & 0 \\ 0 & \mathbb{1} \end{pmatrix}. \quad (2.19)$$

γ^5 has following properties:

$$(\gamma^5)^\dagger = \gamma^5; \quad (2.20)$$

$$(\gamma^5)^2 = \mathbb{1}; \quad (2.21)$$

$$\{\gamma^5, \gamma^\mu\} = 0. \quad (2.22)$$

The significance of γ^5 is we can define projection operators

$$P_\pm = \frac{1}{2}(1 \pm \gamma^5), \quad (2.23)$$

which project onto the Weyl spinors, $\psi_{R,L}$. Hence:

$$\psi_{R,L} = P_\pm \psi. \quad (2.24)$$

In particular, we get from (2.24)

$$\psi_R = \begin{pmatrix} 0 \\ \psi_R \end{pmatrix} \text{ and } \psi_L = \begin{pmatrix} \psi_L \\ 0 \end{pmatrix}. \quad (2.25)$$

Solving eigenvalue equation for γ^5 , eigenvalue +1 corresponds to right-handed and -1 to left-handed Weyl fermion.

Let us define two currents out of Dirac field:

$$j^\mu = \psi^\dagger \gamma^\mu \psi \text{ and } j_5^\mu = \psi^\dagger \gamma^\mu \gamma^5 \psi. \quad (2.26)$$

Considering ψ satisfies the Dirac equation (2.1), divergences of j^μ :

$$\begin{aligned} \partial_\mu j^\mu &= (\partial_\mu \psi^\dagger) \gamma^\mu \psi + \psi^\dagger \gamma^\mu (\partial_\mu \psi) \\ &= (im\psi^\dagger) \psi + \psi^\dagger (-im\psi) \\ &= 0. \end{aligned} \quad (2.27)$$

If ψ satisfies the Dirac equation, j^μ is always conserved. When Dirac field couples with electromagnetic field, j^μ becomes electric current density. Now, computing the divergence j_5^μ and using relation (2.18):

$$\begin{aligned} \partial_\mu j_5^\mu &= (\partial_\mu \psi^\dagger) \gamma^\mu \gamma^5 \psi + \psi^\dagger \gamma^\mu \gamma^5 (\partial_\mu \psi) \\ &= (\partial_\mu \psi^\dagger) \gamma^\mu \gamma^5 \psi - \psi^\dagger \gamma^5 \gamma^\mu (\partial_\mu \psi) \\ &= (im\psi^\dagger) \gamma^5 \psi - \psi^\dagger \gamma^5 (-im\psi) \\ &= 2im\psi^\dagger \gamma^5 \psi \\ &= 0 \text{ if } m = 0. \end{aligned} \quad (2.28)$$

If $m = 0$, chiral current j_5^μ is also conserved. When electromagnetic field is applied, the divergence of chiral current is [4]:

$$\partial_\mu j_5^\mu = \frac{e^2}{16\pi^2} \epsilon^{\mu\nu\alpha\beta} F_{\mu\nu} F_{\alpha\beta}, \quad (2.29)$$

where $F_{\mu\nu} = \partial_\mu A_\nu - \partial_\nu A_\mu$ is electromagnetic field strength tensor and $\epsilon^{\mu\nu\alpha\beta}$ is antisymmetric fourth-rank tensor. Using dual electromagnetic field tensor $G^{\mu\nu} = \frac{1}{2}\epsilon^{\mu\nu\alpha\beta}F_{\alpha\beta}$ and for non-Abelian fields, (2.29) becomes:

$$\partial_\mu j_5^\mu = \frac{e^2}{8\pi^2} \text{tr} G^{\alpha\beta} F_{\alpha\beta}. \quad (2.30)$$

If A_μ corresponds to the electromagnetic four potential, we have:

$$G^{\alpha\beta} = \begin{pmatrix} 0 & -B_x & -B_y & -B_z \\ B_x & 0 & E_z & -E_y \\ B_y & -E_z & 0 & E_x \\ B_z & E_y & -E_x & 0 \end{pmatrix} \text{ and} \quad (2.31)$$

$$F_{\alpha\beta} = \begin{pmatrix} 0 & E_x & E_y & E_z \\ -E_x & 0 & -B_z & B_y \\ -E_y & B_z & 0 & -B_x \\ -E_z & -B_y & B_x & 0 \end{pmatrix}. \quad (2.32)$$

Using $G^{\alpha\beta}$ and $F_{\alpha\beta}$ in equation (2.30), we get:

$$\partial_\mu j_5^\mu = \frac{e^2}{2\pi^2} \mathbf{E} \cdot \mathbf{B}. \quad (2.33)$$

Consider a massless Dirac fermion is under a constant magnetic field \mathbf{B} say in z direction. The resulting Landau level for the two independent Weyl fermions due to this magnetic field is shown in upper panel of Figure 2.3. The Landau level spectrum

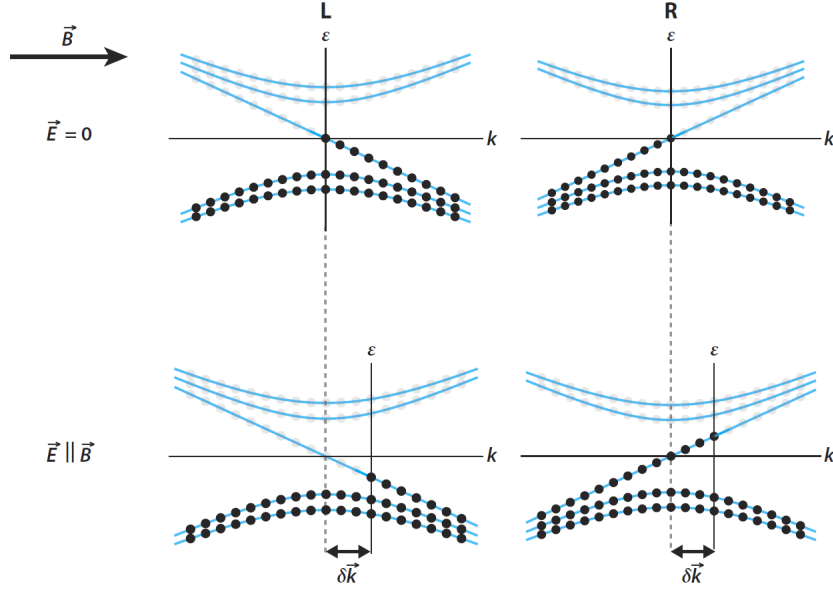


Figure 2.3: Illustration of the chiral anomaly of Weyl fermions based on a Landau level spectrum. (Top panel) Equilibrium energy spectrum of the left-handed (L) and right-handed (R) fermions under a magnetic field \mathbf{B} . Empty states with positive energy are shown by gray dots and filled states with negative energy are shown by black dots. (Bottom panel) Same spectrum in the presence of parallel magnetic field \mathbf{B} and electric field \mathbf{E} . The electrons are displaced from their equilibrium position by $\delta k \sim -\mathbf{E}$ resulting the production of left-handed antiparticles and right-handed particles [4].

also show the chirality of Weyl nodes. The dispersion relation for Landau level in each case is given by

$$\epsilon(k_z) = \pm k_z \quad (2.34)$$

where the ‘+’ sign in front corresponds to left-handed and ‘-’ sign to right-handed Weyl fermion. If we apply electric field \mathbf{E} in the same direction of magnetic field, the electrons will accelerate at a rate ‘ $-eE$ ’ in the z direction. The rates of the right-

and left-handed charge generation due to the presence of the chiral Landau levels is then given by:

$$\frac{\partial n_{R,L}}{\partial t} = \pm \frac{e^2}{4\pi^2} \mathbf{E} \cdot \mathbf{B}. \quad (2.35)$$

The factor of $e^2/4\pi^2$ in equation (2.35) arises from the density of states of the chiral Landau levels. If $n_R - n_L = n_5$, then from (2.35) we obtain

$$\frac{\partial(n_R - n_L)}{\partial t} = \frac{\partial n_5}{\partial t} = \frac{e^2}{2\pi^2} \mathbf{E} \cdot \mathbf{B}. \quad (2.36)$$

This Equation (2.36) and Equation (2.33) correspond to each other when $\mu = 0$ or $j_5^0 \equiv n_5$.

2.2.3 Positive Transverse Magnetoresistance

Magnetoresistance (MR) is the change in electrical resistance of a material due to an applied magnetic field. Mathematically:

$$\text{MR} = \frac{\Delta\rho(H)}{\rho(0)} = \frac{\rho(H) - \rho(0)}{\rho(0)}, \quad (2.37)$$

where $\rho(H)$ is the resistivity under an applied magnetic field H and $\rho(0)$ is the resistivity with no applied magnetic field. In general, MR is reported in percentage.

When magnetic field and electric current are applied perpendicular to each other, extremely large MR can be observed in semimetals [27, 46]. This property has generated a huge interest among researchers in recent years due to the possibility of

novel device applications [47]. Electrical transport in a semimetal generally consists of electrons and holes carriers. When a transverse magnetic field is applied in a semimetal having an equal number of electrons and holes carriers, large MR is observed [5]. In a Hall effect measurement, there is no net transverse current flow when electrons and holes are compensated with each other, but the transverse currents carried by a particular carrier may be non-zero. Due to the presence of a magnetic field, these nonzero transverse currents will experience a Lorentz force in the direction opposite to the applied electric field resulting in a backflow of carriers. Which will lead to a large positive MR in semimetals, stronger than that in normal metals and semiconductors. It should be noted that high-quality single crystals are required to realize electrons and holes compensation and hence to get the large positive magnetoresistance.

Large non saturating MR has been observed in TaAs class (TaAs, TaP, NbAs, NbP) of Weyl semimetal [46, 48–50]. For example, a non-saturating transverse MR of $8.1 \times 10^6\%$ has been observed in NbP under a field of 62 T at 1.5 K [46]. In addition to this, electron-hole compensation has also been observed in this compound explaining the large MR [51]. Large non-saturating MR also has been observed in Weyl semimetals WTe₂ [27] and MoTe₂ [26].

2.2.4 Symmetry Breaking in Weyl Semimetal

A Weyl semimetal has non-degenerate bands crossing in momentum space which requires a breaking of either time-reversal or inversion symmetry. If both time-reversal and inversion symmetries are present, Kramers theorem follows that all of

the bands are doubly degenerate in momentum space and correspond to a Dirac point [52].

In order to realize the minimum number of Weyl nodes, just two with opposite chirality, time-reversal symmetry must be broken. Alternately, if inversion symmetry is broken, there are minimum of four Weyl nodes [53]. Figure 2.4 shows that a Dirac-cone point will lead to two or four Weyl nodes depending on whether time-reversal or inversion symmetry breaks, respectively [1].

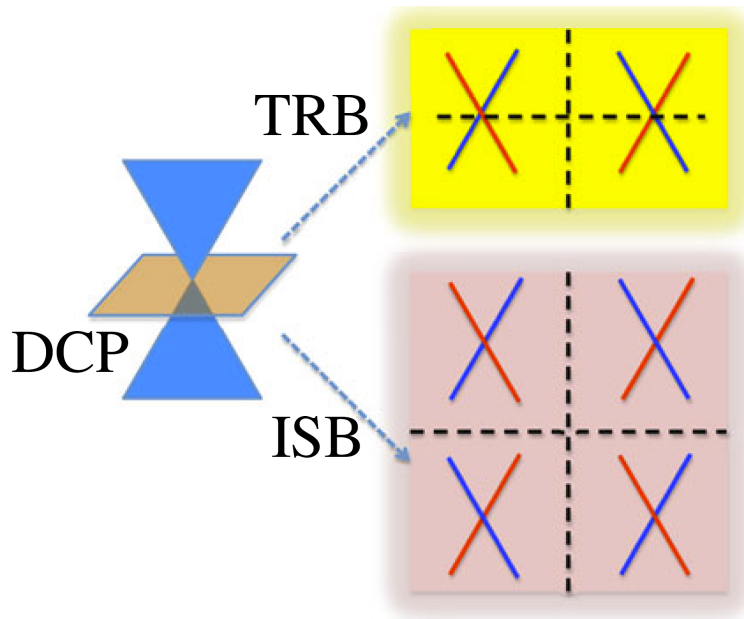


Figure 2.4: A 3D Dirac-cone point (DCP) can be driven into two Weyl nodes with opposite chirality by time-reversal symmetry breaking (TRB) or four Weyl nodes by inversion symmetry breaking (ISB) [1].

2.3 Types of Weyl Semimetal

Weyl semimetal can be classified into two types: type-I and type-II. In type-I Weyl semimetal, the Weyl point appears as a touching point between conduction and valance band forming a point like Fermi surface in momentum space. In type-II Weyl semimetal, Weyl cone is strongly tilted in momentum space so a Weyl point exists at a touching point between electron and hole pockets [12].

Both type-I and type-II Weyl semimetals exhibit chiral anomaly. The chiral anomaly in type-I appears regardless of the direction of the applied magnetic fields. In contrast, the chiral anomaly in type-II Weyl semimetals appears only when the magnetic field is applied along the tilt direction [12, 24, 54]. The Weyl nodes with opposite chirality can be merged and annihilate on both types of Weyl semimetals. There is also a possibility of type-I to type-II transitions in some materials either by doping or applying pressure [54].

Some examples of experimentally verified Weyl semimetals are TaAs, TaP, NbAs and NbP [1–3, 13, 16–21] which belongs to type-I and MoTe₂, WTe₂, Mo_{1-x}W_xTe₂ and TaIrTe₄ [22–25, 55] belongs to type-II.

2.4 Transition Metal Dichalcogenides: Mo_{1-x}W_xTe₂

Transition-metal dichalcogenides (TMDs) have wide-ranging electronic, optical, chemical, thermal, and mechanical properties. Because these properties have potential for device applications, TMDs have been generated great research interests [56–62]. TMDs can be represented by using a common formula MX₂, where M refers to a

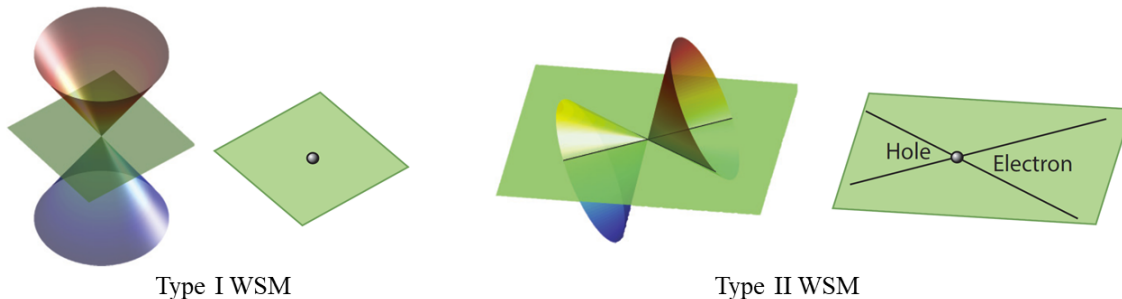


Figure 2.5: Two types of Weyl semimetals. In type-I Weyl semimetal, valence band and conduction band form a point like Fermi surface. In type-II WSM, due to the strong tilting of the Weyl cone, a Weyl point appears at the touching point between electron and hole pockets. The figure is adopted from the reference [5].

transition metal of group IVB (Ti, Zr, or Hf), VB (V, Nb, or Ta), or VIB (Cr, Mo, or W), and X is a chalcogen (S, Se, or Te) [63,64]. Most of the TMDs crystallize into a 2-D layered structure [65,66], in which each monolayer consists of transition-metal atoms between two planes of chalcogens (X-M-X). Atoms within a layer are bonded with a strong covalent bond, while interlayer bonding between the adjacent planes is by weak van der Waals-type forces. Due to this feature, the crystals can be cleaved easily and many of their physical properties are anisotropic [67]. TMDs can display semiconducting, semimetallic, or metallic behavior, which correlates well with the crystalline phase [68,69].

Both MoTe_2 and WTe_2 are type-II Weyl semimetals [22–25] with large non-saturating magnetoresistance (MR) and interesting physical properties [26,27]. The observed MR for MoTe_2 at 2 K and an applied field of 33 T is 61,700%, while that for WTe_2 is 13,000,000% at 0.53 K and an applied field of 60 T. When WTe_2 is

thinned to a single monolayer, it becomes a 2D topological insulator with a conducting edge, in which a superconducting transition can be driven by applying a gate voltage [70,71]. Additionally, a dome-shaped superconducting behavior has been observed in both MoTe₂ and WTe₂ under pressure, with a maximum superconducting transition temperatures (T_c 's) of 8.2 K at 11.7 GPa in MoTe₂ [31] and 7 K at 16.8 GPa in WTe₂ [72]. Also in Mo_{1-x}W_xTe₂ for $x = 0.75$, the type-II Weyl semimetal state has been experimentally observed and this compound has also been predicted to be a tunable Weyl semimetal with variation in x [28,69].

Mo_{1-x}W_xTe₂ can crystalize into one of three different phases: the hexagonal 2H phase (space group P6₃/mmc), the monoclinic 1T' phase (space group P2₁/m), or the orthorhombic T_d phase (space group Pmn2₁) and these phases depends on the synthesis conditions [65,73–76]. The 2H phase has semiconducting nature, whereas the 1T' and T_d phases have semimetallic behavior. For $x \leq 0.10$, the compound is semiconducting at ambient conditions, while it is semimetallic above 900 °C, which can be stabilized at room temperature by rapid cooling. Independent of synthesis conditions, the compound is semimetallic for $x > 0.10$. Rapid cooling of MoTe₂ results in the compound being in the 1T' phase at room temperature, whereas that of WTe₂ results in the T_d phase. Thus, depending on the doping level in Mo_{1-x}W_xTe₂, the semimetallic phase can exhibit either 1T' or T_d structure at room temperature [69,75].

The semimetallic 1T'-phase MoTe₂ undergoes a structural transition at ~ 250 K to the T_d phase at ambient conditions [29,30]. The structural transition temperature (T_s) in MoTe₂ is suppressed by application of external pressure, and when the T_s is

suppressed to lower temperatures, the superconducting transition temperature (T_c) can be increased. The MoTe_2 has T_c of 0.10 K at ambient pressure, which increased to 8.2 K under 11.7 GPa [31–33]. In WTe_2 , no structural transition at ambient pressure has been reported to date. When studied under pressure by conducting synchrotron X-ray diffraction (XRD) at room temperature, Kang *et al.* did not observe structural transition up to 20.1 GPa in WTe_2 [77]. While Zhuo *et al.* and Lu *et al.* both observed a structural transition in WTe_2 at room-temperature and starting under pressure of 6 GPa and 4 GPa, respectively, by conducting synchrotron XRD [69, 78, 79].

Chapter 3

Experimental Methods

3.1 Single Crystal Growth

We used flux method to grow single crystals of MoTe_2 and WTe_2 , and chemical vapor transport method to grow doped $\text{Mo}_{1-x}\text{W}_x\text{Te}_2$ single crystals.

3.1.1 Flux Method

In a flux method, the flux and raw materials for target compounds are put in a crucible and heated to a high temperature until the flux melts and dissolves the raw materials. Then, either by slow cooling or evaporating the flux, supersaturation occurs, and crystal growth takes place [80]. The flux method is also known as high-temperature solution growth since the flux melts at high temperature and acts as a solvent in solution growth. There are two types of flux methods. If the components of the flux are the elements in the products, then the method is called the self-flux method. The other is the use of flux which does not include the element in the

products. In general, the flux is the molten salt, oxide, or metal. We have employed the metallic flux to grow single crystals.

Single crystals from metallic fluxes can be grown by using several techniques. These techniques can be distinguished from one another either based on the operating temperature used or by method used to extract the crystals from the flux [81]. If the temperature below 1200 °C is used, it is good to seal the crucible in an evacuated quartz tube because it holds volatile components, provides a protective environment for the sample growth, and allows to remove the flux from the crystals using a centrifuge. For temperatures over 1200 °C, a protective atmosphere must have to be provided alternatively because of the melting point of the quartz tube, sealing the materials in it is no longer practical.

To grow the crystals, the starting materials are placed in a crucible with materials of lower melting point on the top. When the materials having a lower melting point melt, it flows over the materials at the bottom and starts to incorporate them. It should be noted that the crucible should be inert to the melts, otherwise the reaction between crucible and flux can destroy the crucible or modify the composition of the melts leading to failure of the growth. The crucible with starting materials is placed in a quartz tube slightly elevated from the bottom of the tube to avoid the cracking of the tube during the heating/cooling cycle due to the differential expansion between quartz and crucible. The elevation can be done by putting a small amount of quartz wool or shards of quartz in the bottom of the quartz tube before putting the crucible in the quartz tube. Some quartz wool is also placed on the top of the crucible before vacuum sealing the tube. The evacuated quartz tube is then vertically put in a

furnace and slowly heated to the final temperature. After putting the tube at the final temperature for 12 to 24 hours, it is slowly cooled (generally at the rate of 1 to 2 °C/hour) until the crystals are grown. Once the crystals are grown and the temperature is still above the melting point of flux, the quartz tube is removed from the furnace, inverted, and spun quickly. This leads to passing of the flux through the quartz wool and leaving the crystals in the crucible.

The other method to remove the flux is chemical etching, which involves the removal of solid flux away from the crystals by using an etching chemical. But, this process requires that the etchant must attack the flux much more quickly than it does the crystals. Crystals also can be extracted from the solid flux mechanically. But this is generally not preferred because it is time-consuming.

Single crystals of WTe_2 and $MoTe_2$ were grown by the self-flux method [82, 83]. Elemental molybdenum (99.95%) or tungsten (99.9%) and tellurium (99.999%) were mixed in the ratio of 1:25 and placed in an alumina ampule, and then sealed in a quartz tube under vacuum. For WTe_2 , the quartz tube was heated up to 1000 °C over 10 hours and maintained at this temperature for 24 hours. The quartz tube was slowly cooled down to 800 °C over 200 hours and subsequently cooled to 700 °C over an additional 20 hours. Once the quartz tube was cooled to 700 °C, the tellurium flux was spun off. For $MoTe_2$, on the other hand, the quartz tube was heated up to 1050 °C over 10.5 hours, maintained at this temperature for 24 hours, and then cooled down to 900 °C over 150 hours before it was spun in a centrifuge to remove the Te flux. To remove any residual tellurium flux, single crystals were then heated to 425 °C for 2 days in a sealed quartz tube [69].

3.1.2 Chemical Vapor Transport Method

In a chemical vapor transport (CVT), a condensed phase, typically a solid is volatilized in the presence of a gaseous reactant and deposited elsewhere in the form of crystals [84]. The gaseous reactant is called a transport agent and generally include halogens and halogen compounds. For the deposition to take place, it is essential to have different external conditions at the site of crystallization than at the site of volatilization. This is generally achieved by applying different temperatures in crystallization and volatilization sites.

A typical CVT reaction can be expressed as:



There can be more gaseous products in addition to $C(g)$. This equation represents that the source materials $A(s)$ which are in solid-phase react with the transport agent $B(g)$ at a certain temperature and convert to gaseous products. At other temperature, back reaction occurs resulting in deposition of solid thereby releasing the transport agent.

The parameters that need to be optimized for a successful CVT are transport agent, growth temperature, transport direction, rate of mass transport, and Gibbs energy of the reaction [85]. Based on whether the change of enthalpy is positive or negative in the transport reaction, temperature of source material (T_2) and temperature of crystal growth zone (T_1) must be altered. The exothermic transport reaction indicates the transport from cooler zone to hotter zone, so $T_1 > T_2$ and opposite for

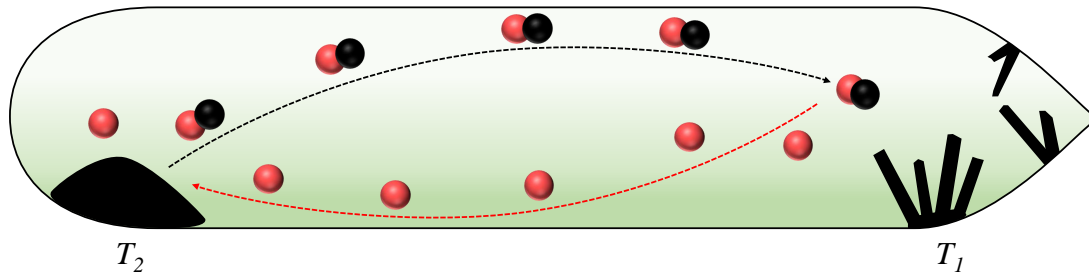


Figure 3.1: Schematic of Chemical Vapor Transport (CVT) method with source materials at temperature T_2 and crystal growth zone at T_1 .

endothermic reaction, that is $T_1 < T_2$.

If CVT is used for compound synthesis or purification, a high transport rate is chosen. A smaller transport rate is required to grow crystals to ensure good quality. Usually, two CVT methods are applied in the laboratory: transport in open or closed system [84]. In an open system, a tube made from glass or ceramic materials and open on both sides is used. The source material is kept inside the tube at a certain temperature and the flow of the transport agent is continuously passed over the source material leading to deposition of the material at another side at a different temperature under the release of the transport agent. The open system is generally used for substance separation and purification. A closed system contains a sealed tube and the transport agent remains in the systems, constantly re-entering the reaction. Hence the closed system requires much fewer transport agents than the open system.

In most cases, CVT reactions are executed in a closed system which can be made out of suitable glass. The selection of glass depends on the operating temperature. Borosilicate glass can be used up to 600 °C. For higher temperatures (up to 1200 °C),

quartz tubes are suitable. Typically, the closed tube has a diameter of 10 to 20 mm and a length of 100 to 200 mm [84]. It should be noted that the quartz tube contains water up to 50 ppm, which will be released during the heating. To avoid this, it is recommended to bake out the quartz tubes before using them in CVT method. If the materials that have to be transported are corrosive to quartz tube, ceramic materials containers or glassy carbon can be integrated into the quartz tubes [85].

Now, the general procedures for preparing the transport ampoules will be discussed. First, approximately 0.5 gram to 1 gram of the solid, that is to be transported, is put in the bottom of the prepared ampoule [84]. This can be done by using a funnel which is long enough such that the outlet is near the bottom of the ampoule. Transport agents can be added in a similar way. The amount of transport agent is chosen in such a way that the pressure in the closed ampule, calculated using the gas law, will be 1 bar at the experimental temperature. The transport ampule is generally connected to a vacuum line with a ground-glass joint. One can also use quick-fit joints. Once the transport ampule is vertically connected to the vacuum line, it is recommended to cool the contents of the ampule using liquid nitrogen before the evacuation. After approximately 3 minutes of cooling, the ampule is evacuated and sealed. Cooling of the ampule is necessary if there is a danger of vaporization or sublimation of any of the content at room temperature; as in the case of using iodine as a transport agent.

The temperature gradient required for CVT is obtained by using tube furnaces with two or three independent heating zones. In order to maintain the convection of the gas as low as possible, the transport furnace must be kept horizontally. However,

to prepare a large amount of substance in endothermic transport, the furnace can be tilted such that the sink side is at higher elevation than the source side. In this case, the transport takes place in a vertical direction due to a high convective contribution to the gas motion. The transport, however, takes place only up to 3 *cm*. In such experiments, an ampule having a large cross-section around 30 *cm*² is used. For exothermic transport reactions, the transport rate is determined only by diffusion since the convective part is neglected [84].

Doped single crystals of $\text{Mo}_{1-x}\text{W}_x\text{Te}_2$ for $x = 0.10, 0.30, 0.40, 0.50, 0.70, 0.75,$ and 0.90 were grown by the CVT method using iodine as the transport agent [75]. Stoichiometric ratios of molybdenum (99.95%), tungsten (99.9%) and tellurium (99.999%) were ground and sealed in evacuated quartz tubes before heating to 750 °C for 2 days. These polycrystalline samples were then vacuum sealed in quartz tubes with 5 mg cm^{-3} of iodine (99.8%). A temperature gradient of 100 °C was used with the crystal-growth-zone temperatures of 1000 °C for $x = 0.10$, 950 °C for $0.10 < x < 0.90$, and 900 °C for $x = 0.90$. Samples were finally quenched in ice-water for $x \leq 0.50$, while they were slowly cooled down to room temperature for $x > 0.50$ [69].

3.2 Elemental Composition Analysis

The elemental compositions of the samples were determined by using a scanning electron microscope (SEM) with energy-dispersive X-ray spectroscopy (EDS) capabilities (JEOL 8600 electron microprobe at the Texas Center for Superconductivity at the University of Houston). To prepare the samples for chemical analysis using

SEM/EDS, carbon tape was attached to the top of a graphite disk and the samples were placed on the tape.

3.3 X-ray Diffraction

The crystallographic orientations of single crystals were determined by X-ray diffraction (XRD) using a Rigaku X-ray diffractometer with a monochromatic Cu $K\alpha$ ($\lambda = 1.54178 \text{ \AA}$) radiation source at the Texas Center for Superconductivity at the University of Houston. Temperature-dependent synchrotron X-ray diffraction (SXRD) data were obtained at the 01C2 beamline (0.826569 \AA) of the National Synchrotron Radiation Research Center (NSRRC, Hsinchu, Taiwan).

3.4 Transport Measurements

3.4.1 Magneto-Transport Measurements

Quantum Design Physical Properties Measurement System (PPMS) was used for resistivity and magnetoresistance (MR) measurements. The resistivity was measured from 390 K down to 2 K by a standard four-point probe method using the PPMS AC transport option. The magnetoresistance was measured by applying magnetic fields from -7 T to 7 T.

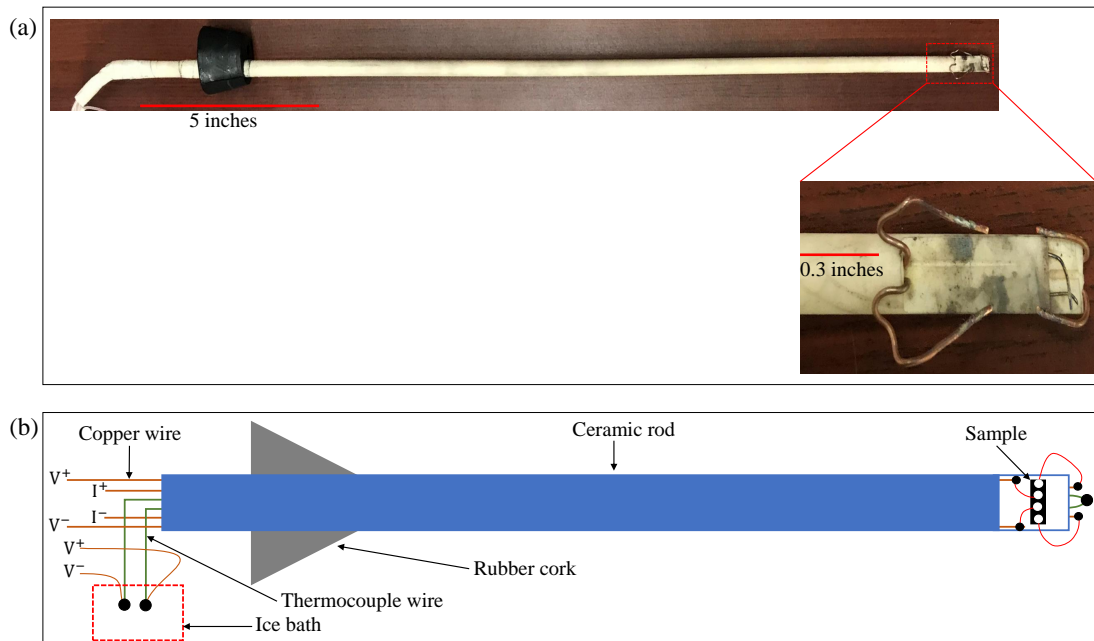


Figure 3.2: (a) A real picture and (b) schematic drawing of high temperature resistivity measurement probe.

3.4.2 High Temperature Resistivity Measurements

The resistivity measurement above room temperature was performed by four-point method using a homemade probe. A real picture and the schematic drawing of the probe are shown in Figure 3.2. It consists of a ceramic rod, which has eight through holes (channels). Four copper wires were passed through the four channels so that the wires are coming out from both ends of the rod. For a thermocouple, a pair of Alumel and Chromel wires were similarly inserted through the other two channels. One end of the thermocouple wires were connected to each other by spot welding whereas each of the other ends were connected to a copper wire. For the four-point resistivity measurements, four platinum wires having a diameter of $25\ \mu\text{m}$

were connected on a sample surface using Silver Conductive Epoxy (product number 16016) from Ted Pella. The epoxy consists of two components: Part A and Part B. Those two parts were mixed in the ratio of 1:1, applied to connect the wires, and dried at 120 °C for 15 minutes under a continuous flow of Argon gas. The sample was then placed at the end of the ceramic rod, near the thermocouple joint. The four platinum wires were connected to four copper wires using the same Silver Conductive Epoxy and dried similarly as mentioned above. The copper wires coming out from another end of the rod were connected to electronics. The ends of the thermocouple connected with copper wires were inserted in a stainless-steel tube. The ceramic rod was the inserted in a tube furnace and the furnace was ramped up at the rate of 1 °C/min. Argon gas was continuously supplied to protect the sample and copper wires from oxidation during the measurement. The thermocouple was calibrated with a reference temperature of 0 °C. To maintain the reference temperature, the stainless-steel tube was dipped in an ice bath during measurement. The copper wires from the ends of the thermocouple were connected to a voltmeter to measure the potential difference. Resistivity measurement was performed using Keithley 2400 SourceMeter and 2182 Nanovoltmeter in Delta mode configuration and data acquisition was done by using LabVIEW.

3.5 High-Pressure Study

3.5.1 Beryllium-Copper Clamp Cell

The beryllium-copper (BeCu) clamp cell which was prepared based on Dr. Paul C. W. Chu's design was used for high-pressure resistivity measurements up to 18 kbar. Advantages of BeCu clamp cell include a larger size sample (size up to 4 mm) and provision for application of hydrostatic pressure. As shown in Figure 3.3, the outer part consists of a locking screw (at the bottom) and the main body (above the locking screw) prepared from hardened BeCu. The different components of inner parts, which are inside the main body are shown in a schematic drawing (Figure 3.4). In the center, there is a Teflon cup. On the top of the Teflon cup, there is a Be-Cu cap. The Be-Cu cap has been machined such that the piston of the cap fits well with the Teflon cup and no leaking of the pressure medium occurs. There is a hole in the center of the Be-Cu cap. Twisted pairs of wires and a thermocouple goes through the hole, which was secured by using Stycast.

A sample was prepared for four-point resistivity measurement by connecting four platinum wires on the surface using Ted Pella Leitsilber 200 Silver paint. For the in situ pressure measurement, a manometer was prepared from a small piece of high purity lead (Pb 99.999%). Lead has a very sharp transition (0.02 K transition width) and pressure dependence of the T_C has been well-studied. In the lead piece, the secondary (inner) coil was prepared by winding 2 - 4 layers of copper wire (46 gauge). By using another copper wire (44 gauge), two additional layers had been wound as the primary (outer) coil.

The sample and the lead manometer were connected to four pairs of twisted wires coming out from the Be-Cu cap. The Teflon cup was filled with pressure medium (Fluorinert FC-77) before putting the Be-Cu cap with a sample and lead manometer on the top. Then the cup was inserted into a hardened BeCu cylinder with a through-hole having the diameter the same as the Teflon container. Small BeCu rings were put on both sides of the Teflon container before bringing pistons (made from tungsten carbide) from above (top piston) and below (back piston). On the top of the “top piston”, a hardened BeCu plate (top plate) was placed. There is a through-hole on the top piston, top plate, and top of the main body, which allow the electrical connections to pass through to the measurement electronics. Before hand tightening the locking screw on the main body, another hardened BeCu plate (back plate) was put on the bottom of the back piston. The pressure cell was then attached to the probe and inserted into a double jacket glass Dewar filled with liquid nitrogen (LN2) in the outer space and liquid He⁴ in the inner space. The temperature was controlled by moving the pressure cell up-down with respect to the cryostat. For the temperature measurement above 50 K, the thermocouple that was inserted near the sample in the Teflon container was used. The temperatures below 50 K were measured by a germanium resistor embedded in the wall of the BeCu clamp cell. To apply pressure, a force from a hydraulic press was applied. When the force is applied, the piston moves by squeezing the Teflon container and increasing the pressure. The locking screw is tightened before releasing the force, which keeps the Teflon container from expanding and locks in the pressure. All of the BeCu caps, Teflon cups, and BeCu rings were machined for each pressure run using a lathe.

During the pressure measurement, the primary coil of the lead manometer was driven (applied a small current) and the mutual inductance of the secondary coil was measured using LR400 AC RESISTANCE BRIDGE. A sharp drop in inductance was observed when the lead enters into the superconducting state due to the diamagnetic property of the superconductor. The T_c of the lead was defined at the mid-point of the sharp drop. Reference T_c was determined by doing measurement without applying pressure in the cell. The T_c of the lead decreases with pressure. By calculating the difference in T_c , the pressure of the sample environment was determined using the table given in Appendix A, which is based on Equation 3.2 [86].

$$\Delta T_c = -3.689 \times 10^{-2}P + 1.026 \times 10^{-4}P^2 \quad (3.2)$$

For the resistivity measurement, Keithley 2400 SourceMeter, and 2182 Nanovoltmeter in Delta mode configuration were used. Data acquisition was done by using LabVIEW.

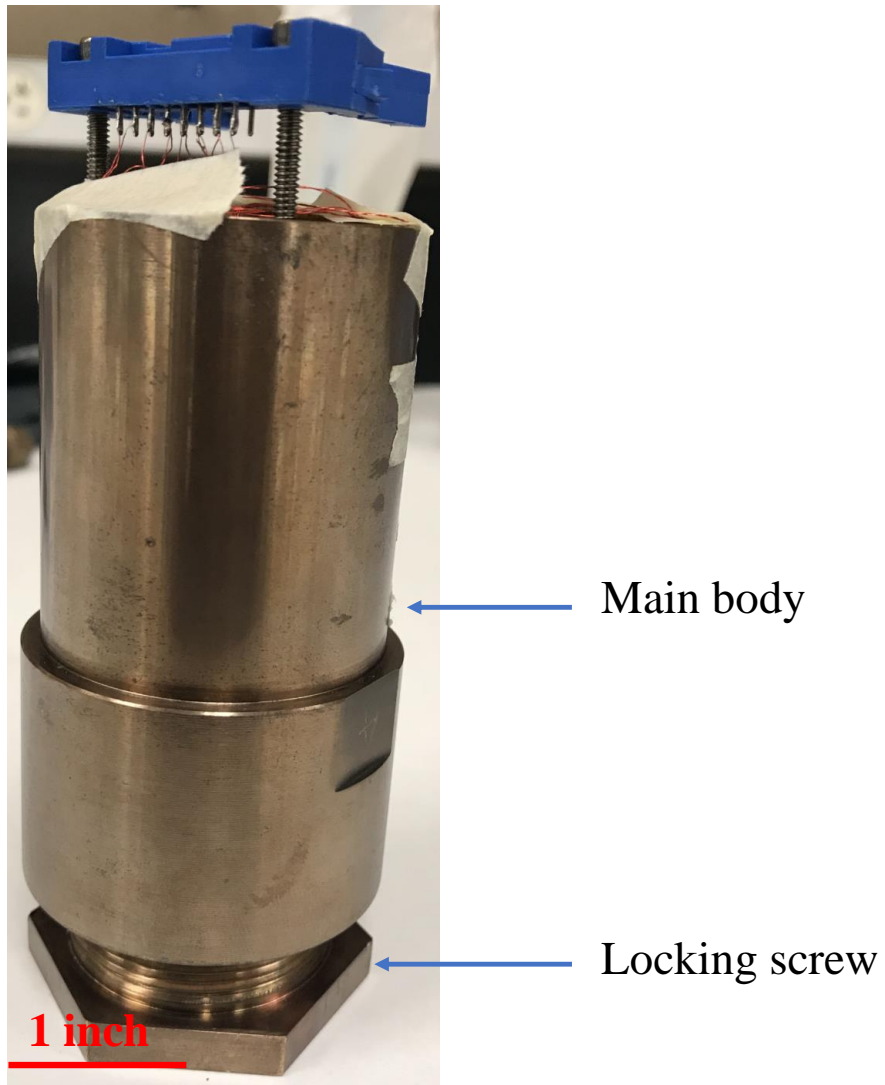


Figure 3.3: A photograph of the high-pressure beryllium-copper clamp cell.

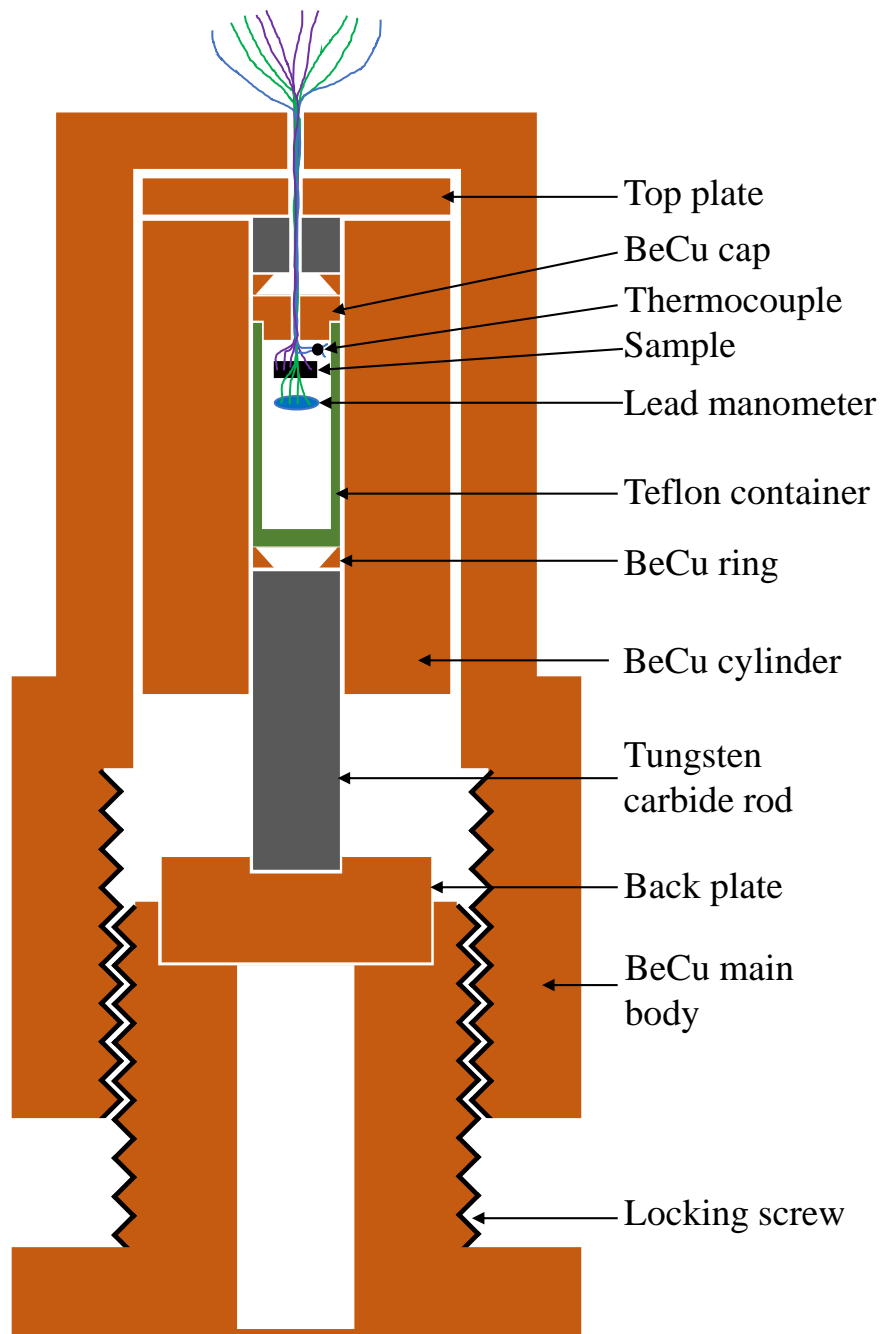


Figure 3.4: Schematic drawing of the high-pressure beryllium-copper (BeCu) clamp cell.

3.5.2 Diamond Anvil Cell

High-pressure resistivity measurements up to 43 GPa was done by using a diamond anvil cell (DAC). A picture and schematic diagram of DAC used in this study are shown in Figure 3.5. There are two parts in the cell: upper and lower, made from hardened BeCu. Each part of the cell consists of a diamond anvil with culet diameter of $\sim 400 \mu\text{m}$ attached to a tungsten-carbide (WC) piece using Stycast. The WC piece is called a diamond seat or backing piece. There is a conical hole in each of the seats aligned with the hole from the cell allowing optical access to the sample. The conical shape helps to collect more light, thus enhancing the imaging. Four screws were used for holding the WC seat in each part of the cell. Horizontal alignment of the culet of the diamond can be obtained by adjusting these screws.

A gasket with a central hole was sandwiched between the two diamond culets and contains a sample, pressure medium, and a ruby piece. The gasket can be made from various materials depending on the requirement for the experiment. The basic requirement for the material is that it must be hard and ductile. If one wants to use it for susceptibility measurements, the materials also must be non-magnetic and non-superconducting. We used a square-shaped stainless steel gasket with a thickness of $\sim 250 \mu\text{m}$ for the resistivity measurements. The gasket was pre-indented by applying pressure of $\sim 1/3$ of target pressure (with target pressure ~ 42 GPa, we applied ~ 14 GPa and the thickness of the pre-indented area was $\sim 43 \mu\text{m}$). Then, a hole with a diameter equal to culet size was drilled in the pre-indented area. To insulate the gasket for the resistivity measurements, the pre-indented area was filled with cubic boron nitride (c-BN) and pressed to ~ 15 GPa (little higher than pre-indentation of

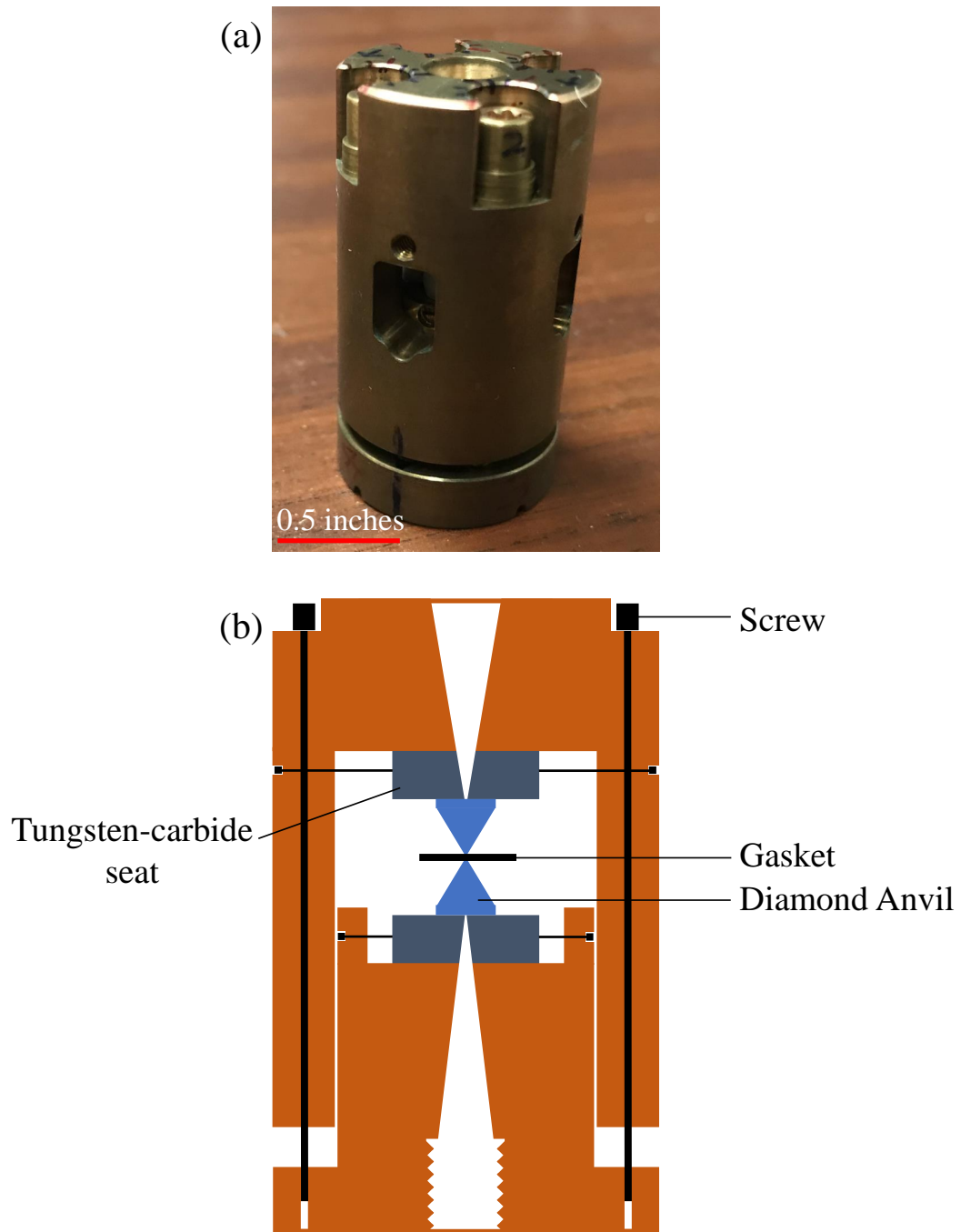


Figure 3.5: (a) A real picture and (b) schematic drawing of diamond anvil cell (DAC).

the gasket). After that, a hole of diameter $\sim 130 \mu\text{m}$ ($\sim 1/3$ of the culet size) was made at the center of the pre-indented area. The $\sim 130 \mu\text{m}$ hole was then filled with c-BN, which acts as a pressure medium for the sample.

Resistivity and Hall measurements under pressure were done using the van der Pauw method. A sample with a dimension around $90 \times 90 \times 15 \mu\text{m}^3$ was prepared from a single crystal and placed on the top of the pressure medium. Four electrodes with sharp tips ($\sim 10 \mu\text{m}$) were cut using a razor from a $\sim 10 \mu\text{m}$ thick platinum foil.

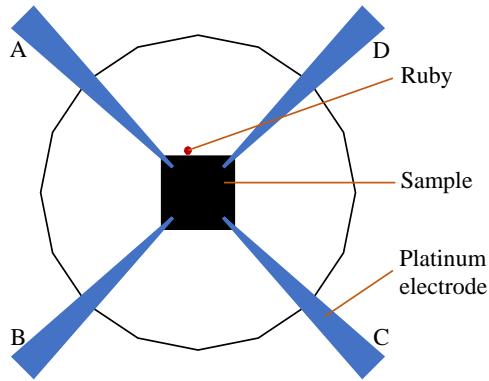


Figure 3.6: Schematic drawing of preindented gasket area with a sample, four platinum electrodes, and a Ruby piece. The electrodes are used for resistivity and Hall measurements by the van der Pauw method.

The electrodes were then adjusted such that they rest on four corners of the sample as shown in Figure 3.6. A small ruby piece with diameter of $\sim 10 \mu\text{m}$ was placed near the sample for pressure measurement. There are four screws, two right and two left-handed, that connect the two parts of the cell. These screws were slowly tightened to increase the pressure. The pressure of the cell at room temperature was measured using a ruby fluorescence manometer. The pressure cell was then connected to a

puck that is designed to fit in the PPMS from Quantum Design. ACT option from the PPMS was used to perform the van der Pauw resistivity and Hall measurements. During resistivity measurements, the platinum electrodes A, B, C, and D from Figure 3.6 were connected to I^+ , I^- , V^- , and V^+ respectively in Chanel 1 of the puck, which gave resistance $R_{AB,CD} = \frac{V_{CD}}{I_{AB}}$. Similarly $R_{BC,DA} = \frac{V_{DA}}{I_{BC}}$ was measured in Chanel 2. The sheet resistance (R_s) can be calculated using van der Pauw formula [87]

$$e^{-\pi R_{AB,CD}/R_s} + e^{-\pi R_{BC,DA}/R_s} = 1. \quad (3.3)$$

By knowing thickness (t) of the sample, resistivity can be obtained using $\rho = R_s t$.

For Hall measurement, in Chanel 1, current was supplied through A(I^+) and C(I^-) and potential difference between D(V^-) and B(V^+) was measured under positive and negative magnetic fields. This gave $V_{DB,P}$ and $V_{DB,N}$, where P and N corresponds to *positive* and *negative* magnetic fields. Similarly, Channel 2 has connections B(I^+), D(I^-), A(V^-), and C(V^+) giving $V_{AC,P}$ and $V_{AC,N}$ under positive and negative magnetic field, respectively. Then, Hall voltage was calculated using

$$V_H = \frac{V_{DB,P} - V_{DB,N} + V_{AC,P} - V_{AC,N}}{4}. \quad (3.4)$$

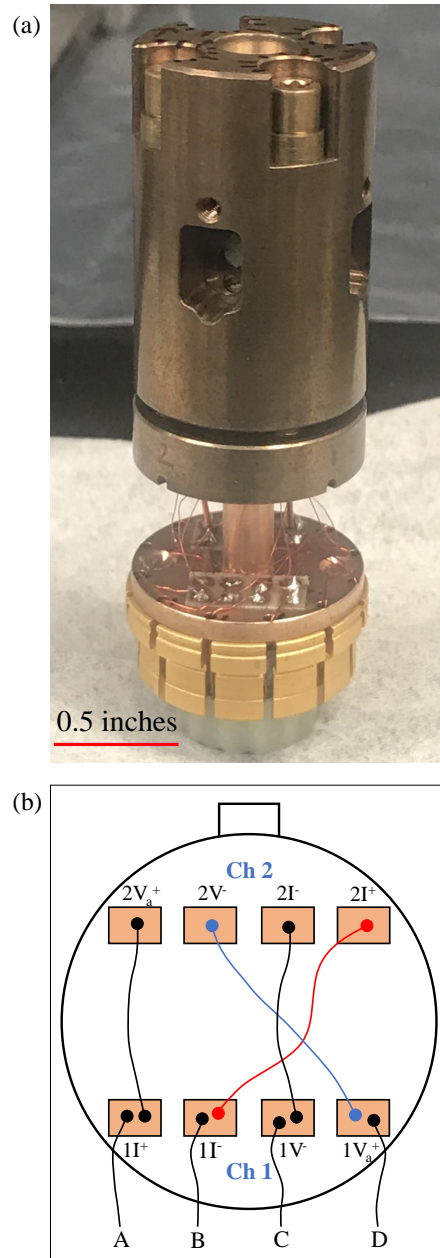


Figure 3.7: (a) A picture of DAC after connecting with a puck and (b) schematic drawing of the puck connections for van der Pauw resistivity measurement using ACT option from the PPMS. The wires A, B, C, and D are connected to the corresponding platinum electrodes in Figure 3.6.

Chapter 4

Results

We have carried out doping and pressure dependence studies on single crystalline $\text{Mo}_{1-x}\text{W}_x\text{Te}_2$ with various tungsten compositions. To determine the relation between the structural transition temperature (T_s) and the tungsten composition, doping dependence study were conducted on $\text{Mo}_{1-x}\text{W}_x\text{Te}_2$ for $x = 0, 0.10, 0.30, 0.50, 0.70, 0.90,$ and 1. High pressure studies up to 17 kbar were carried out on $\text{Mo}_{1-x}\text{W}_x\text{Te}_2$ for $x = 0.10, 0.40,$ and 0.75 using a BeCu clamp pressure cell and pressure-dependent structural transition and superconductivity phase diagrams have been constructed. Pressure effects on superconductivity, magnetoresistance, and the Hall effect have been studied in $\text{Mo}_{0.50}\text{W}_{0.50}\text{Te}_2$ by applying pressure up to 43 GPa using a diamond anvil cell (DAC).

In this chapter, I will first discuss the composition determined by energy dispersive X-ray spectroscopy (EDS), the X-ray diffraction patterns, and the magneto-transport properties of single-crystal $\text{Mo}_{1-x}\text{W}_x\text{Te}_2$ for $x = 0, 0.10, 0.30, 0.40, 0.50, 0.60, 0.70, 0.75, 0.90,$ and 1. Results from the doping-dependent structural transition

and high-pressure studies will then be presented.

4.1 Elemental Analysis using Energy-Dispersive X-ray Spectroscopy

Table 4.1 shows the nominal compositions and those determined by energy-dispersive X-ray spectroscopy (EDS) of single-crystalline $\text{Mo}_{1-x}\text{W}_x\text{Te}_2$ for $x = 0, 0.10, 0.30, 0.40, 0.50, 0.70, 0.75, 0.90,$ and 1. EDS measurements show excess tellurium, which may be due to the presence of unreacted tellurium in the single crystals. In most of the $\text{Mo}_{1-x}\text{W}_x\text{Te}_2$ single crystals compositions, x from EDS measurement is close to nominal x , except for $\text{Mo}_{0.60}\text{W}_{0.40}\text{Te}_2$ and $\text{Mo}_{0.25}\text{W}_{0.75}\text{Te}_2$ (Figure 4.1), which could be due to the following reason. During the growth of doped single crystals using the chemical vapor transport (CVT) method, the finely ground starting materials were pelletized to make polycrystalline precursors for all cases except for the 40 % ($x = 0.40$) and 75 % ($x = 0.75$) tungsten doped compounds. Due to the smaller atomic radius of Mo than that of W, hybridization between the Te p_z orbitals increases in $\text{Mo}_{1-x}\text{W}_x\text{Te}_2$ with increasing Mo content [88]. This suggests that higher Mo concentration is favorable in the compound if there is no constraint (pelletization is constraint here). Thus, making polycrystalline precursors without pelletization resulted in higher Mo content in the final measured compositions. This observation suggests that pelletization of the finely ground starting materials is one of the necessary steps to grow doped single crystals of $\text{Mo}_{1-x}\text{W}_x\text{Te}_2$ with the desired compositions.

Table 4.1: Nominal compositions and compositions determined by energy-dispersive X-ray spectroscopy (EDS) for $\text{Mo}_{1-x}\text{W}_x\text{Te}_2$ ($x = 0, 0.10, 0.30, 0.40, 0.50, 0.70, 0.75, 0.90,$ and 1).

Nominal composition	EDS measurement results
MoTe_2	$\text{MoTe}_{2.30}$
$\text{Mo}_{0.90}\text{W}_{0.10}\text{Te}_2$	$\text{Mo}_{0.90}\text{W}_{0.10}\text{Te}_{2.26}$
$\text{Mo}_{0.70}\text{W}_{0.30}\text{Te}_2$	$\text{Mo}_{0.74}\text{W}_{0.26}\text{Te}_{2.40}$
$\text{Mo}_{0.60}\text{W}_{0.40}\text{Te}_2$	$\text{Mo}_{0.81}\text{W}_{0.19}\text{Te}_{2.37}$
$\text{Mo}_{0.50}\text{W}_{0.50}\text{Te}_2$	$\text{Mo}_{0.56}\text{W}_{0.44}\text{Te}_{2.49}$
$\text{Mo}_{0.30}\text{W}_{0.70}\text{Te}_2$	$\text{Mo}_{0.27}\text{W}_{0.73}\text{Te}_{2.41}$
$\text{Mo}_{0.25}\text{W}_{0.75}\text{Te}_2$	$\text{Mo}_{0.46}\text{W}_{0.54}\text{Te}_{2.70}$
$\text{Mo}_{0.10}\text{W}_{0.90}\text{Te}_2$	$\text{Mo}_{0.12}\text{W}_{0.88}\text{Te}_{1.77}$
WTe_2	$\text{WTe}_{2.26}$

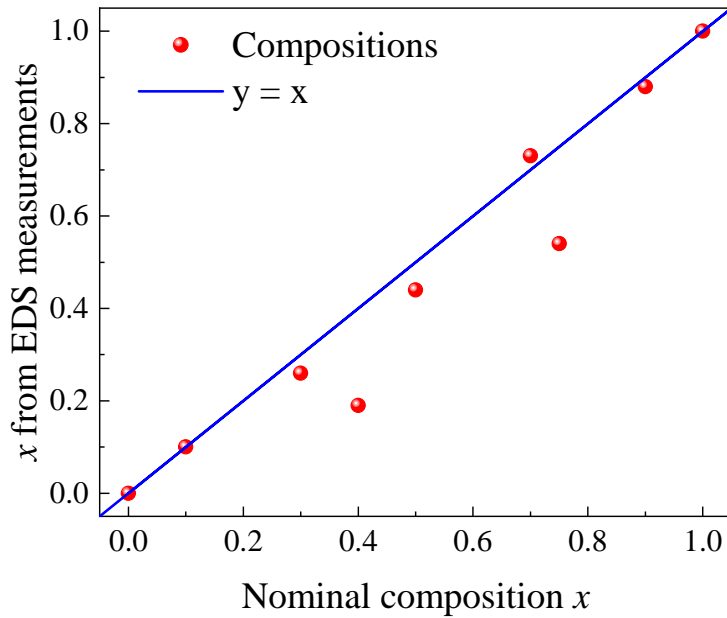


Figure 4.1: Plot of nominal composition x vs composition x from EDS measurements for $\text{Mo}_{1-x}\text{W}_x\text{Te}_2$ single crystals. $y = x$ is the reference line passing through the origin. Except for $\text{Mo}_{0.60}\text{W}_{0.40}\text{Te}_2$ and $\text{Mo}_{0.25}\text{W}_{0.75}\text{Te}_2$, the composition from EDS measurement is close to the nominal composition.

4.2 X-ray Diffraction Patterns

The X-ray diffraction (XRD) patterns of the single crystals $\text{Mo}_{1-x}\text{W}_x\text{Te}_2$ for $x = 0, 0.10, 0.30, 0.40, 0.50, 0.70, 0.75, 0.90,$ and 1 are shown in Figure 4.2(a). All of the observed peaks were indexed as $(0\ 0\ 2k)$ reflections, indicating that the exposed surfaces of the crystals are along the c -plane. Magnified XRD patterns showing the (002) peaks are presented in Figure 4.2(b) for all of the $\text{Mo}_{1-x}\text{W}_x\text{Te}_2$ single crystals. With increasing W concentration, the 2θ angle for the (002) peak either decreases or remains constant except for $\text{Mo}_{0.60}\text{W}_{0.40}\text{Te}_2$. With increasing tungsten composition $x = 0.30$ to $x = 0.40$, the 2θ angle for the (002) peak increases. Values for the calculated lattice parameter c by considering the monoclinic $1T'$ phase with a monoclinic angle $\beta = 93^\circ 55'$ for MoTe_2 and $\text{Mo}_{0.90}\text{W}_{0.10}\text{Te}_2$ and the orthorhombic T_d phase for all of the other single crystals are shown in Figure 4.2(c). The obtained c for MoTe_2 is $13.85 \pm 0.04 \text{ \AA}$ and that for WTe_2 is $14.04 \pm 0.04 \text{ \AA}$, and both are close to the previously reported values of $c = 13.86 \text{ \AA}$ for MoTe_2 and $c = 14.07 \text{ \AA}$ for WTe_2 [74]. The values of the calculated lattice parameter c for the doped compounds lie between those for the parent compounds. In general, the lattice parameter c increases with increasing W composition, which is due to the larger ionic radius of W^{4+} (0.66 \AA) compared to that of Mo^{4+} ions (0.65 \AA) [89, 90].

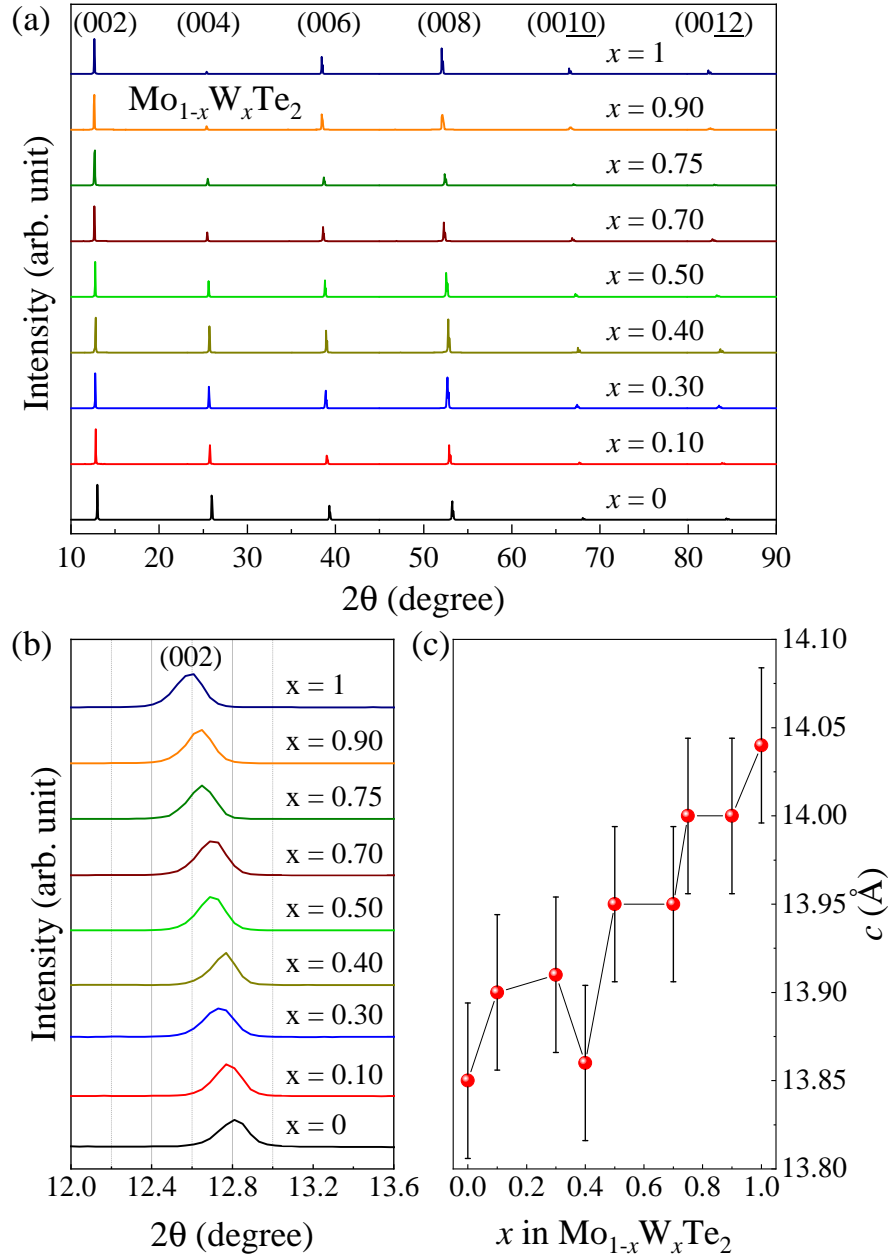


Figure 4.2: (a) X-ray diffraction (XRD) patterns from 10 to 90 degrees, (b) magnified view of the (002) XRD peaks, and (c) lattice parameter (c) vs composition (x) for $\text{Mo}_{1-x}\text{W}_x\text{Te}_2$ single crystals ($x = 0, 0.10, 0.30, 0.40, 0.50, 0.60, 0.70, 0.75, 0.90,$ and 1).

4.3 Magnetotransport Properties

Temperature dependence of the electrical resistivity of $\text{Mo}_{1-x}\text{W}_x\text{Te}_2$ single crystals as a function of W doping is shown in Figure 4.3(a). During these measurements, the four-point probe method was used with four contacts on the ab -plane and current along the a -axis. All of the single crystals show metallic behavior. Residual resistivity ratio (RRR) *vs* x is plotted in Figure 4.3(b). Here the RRR is defined as $RRR = \rho(300 \text{ K})/\rho(2 \text{ K})$. For the parent compounds, the RRR is large with values around 151 for MoTe_2 and 228 for WTe_2 . The large RRR values indicate the high quality of the single crystals. In comparison with the parent compounds, the RRR of the doped single crystals is drastically lower, with values from ~ 6 to ~ 13 . The significant decrease in the RRR value may be due to the presence of defects scattering [90,91].

Under a magnetic field, the resistivity of WTe_2 follows the zero-field curve until it is cooled to the so-called “turn on” temperature T^* [27], below which the resistivity starts to increase as shown in Figure 4.4(a). The obtained T^* , defined as the point where the resistivity is minimum, is around 64 K for WTe_2 under 7 T when the current (I) is along a and the magnetic field (H) is along the c axis. Figure 4.4(b) shows the magnetic field dependence of the magnetoresistance (MR) at 2 K for WTe_2 with $I \parallel a$ and $H \parallel c$. We observed maximum MR around 74 000% at 2 K and under a magnetic field of 7 T, which is comparable to the value reported by Ali *et al.* (MR ~ 105 000% at 2 K and under 7 T) [27]. A Shubnikov–de Haas quantum oscillation is also observed at 2 K [inset in Figure 4.4(b)] following extraction of the oscillations after subtracting a smooth quadratic background above 4 T.

The corresponding MR behavior of MoTe_2 under magnetic field with $I \parallel a$ and H

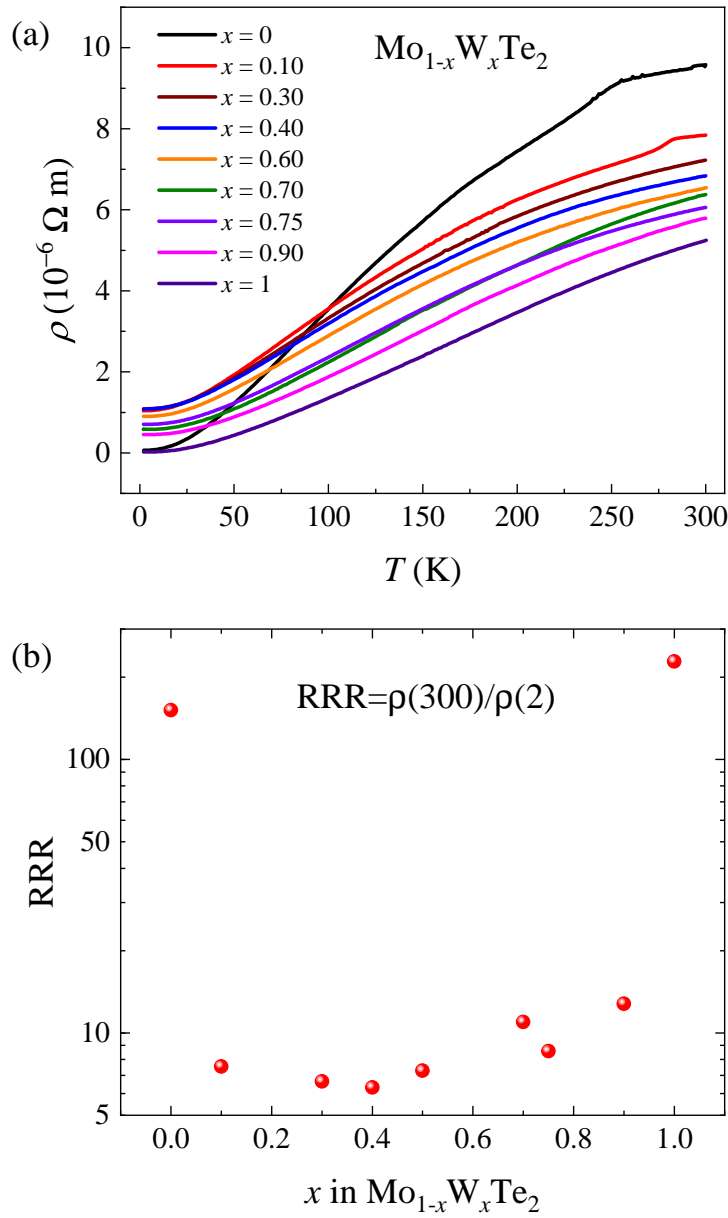


Figure 4.3: (a) Temperature-dependent resistivity from 300 K down to 2 K and (b) composition-dependent residual resistivity ratio (RRR) ($RRR = \rho(300 \text{ K})/\rho(2 \text{ K})$) of $\text{Mo}_{1-x}\text{W}_x\text{Te}_2$ for $x = 0, 0.10, 0.30, 0.40, 0.50, 0.60, 0.70, 0.75, 0.90$, and 1. The anomaly in the resistivity curve for each of $x = 0$ and 0.10 in (a) corresponds to a structural transition.

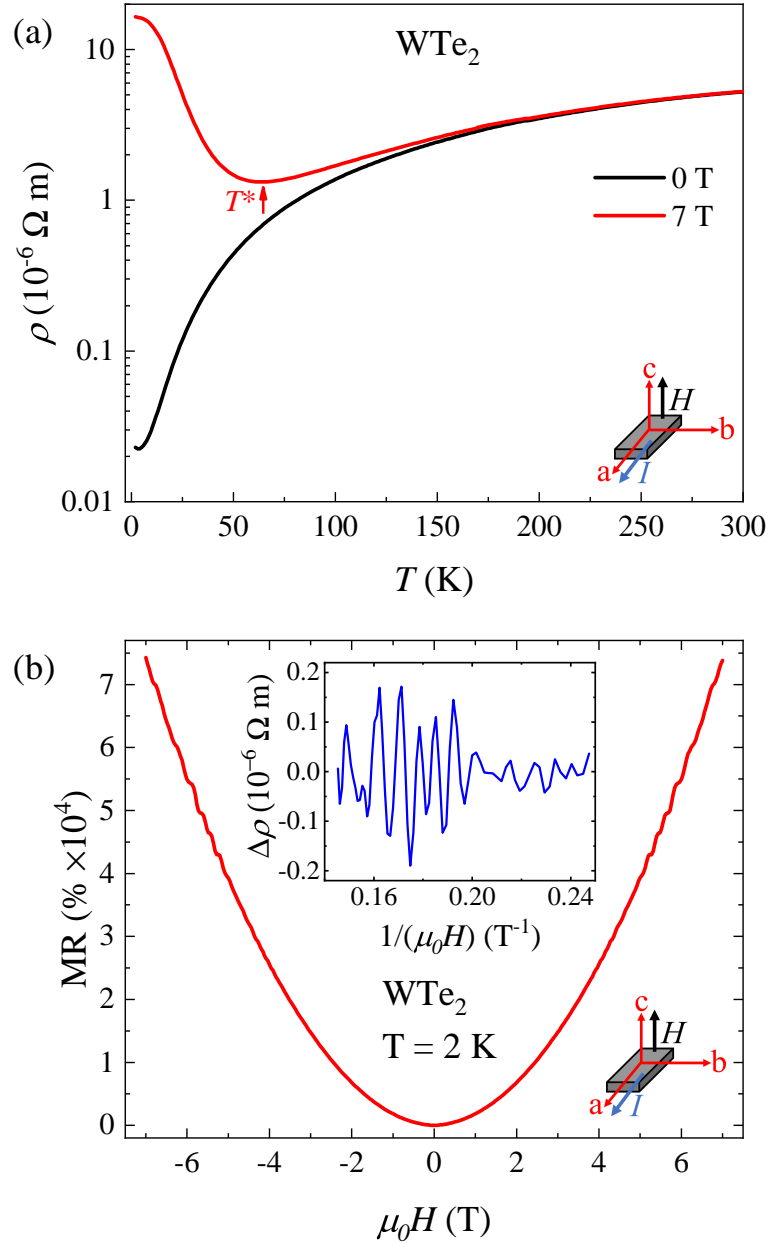


Figure 4.4: Magnetic field effects on WTe₂ with current along the a axis and magnetic field parallel to the c axis. (a) Temperature-dependent resistivity without and with magnetic field of 7 T. (b) Field-dependent MR at 2 K. Inset: quantum oscillations demonstrate the high quality of the crystal.

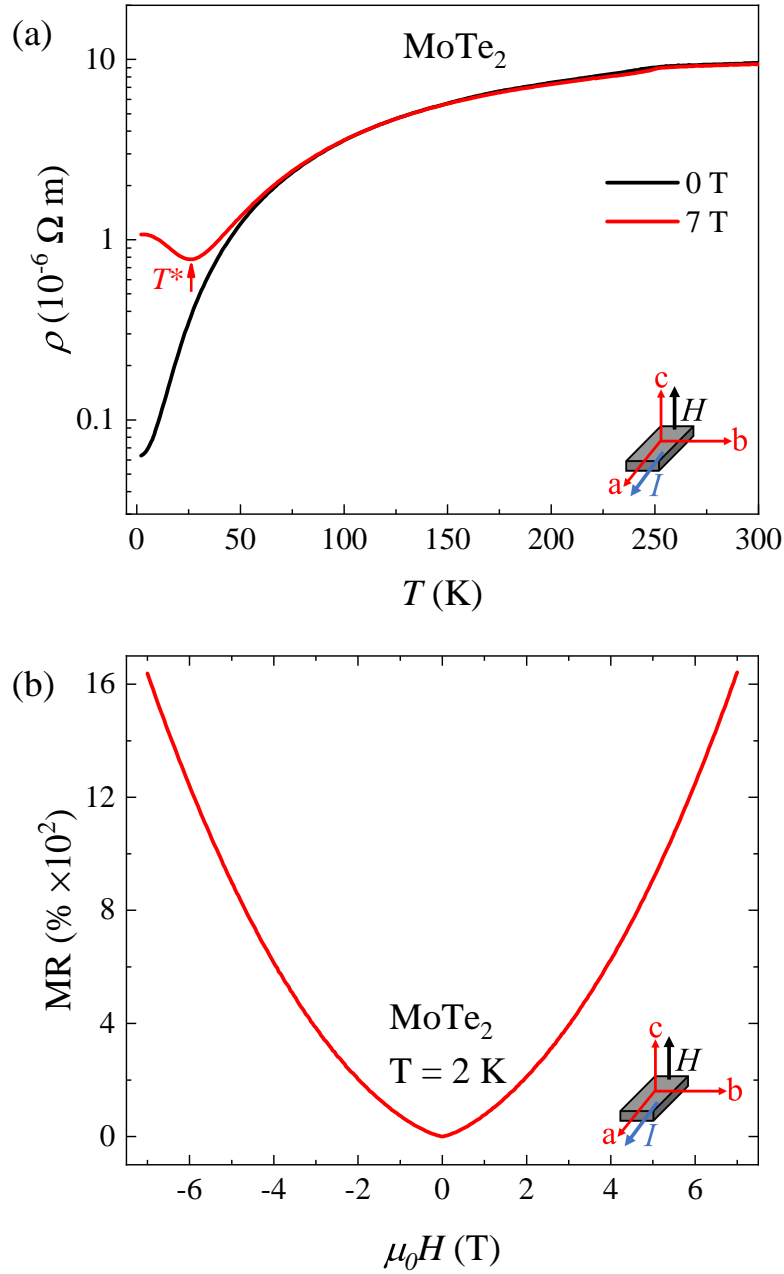


Figure 4.5: (a) Temperature-dependent resistivity without and with magnetic field of 7 T and (b) field dependence of MR up to 7 T at 2 K for MoTe₂ with current parallel to a axis and magnetic field perpendicular to ab plane.

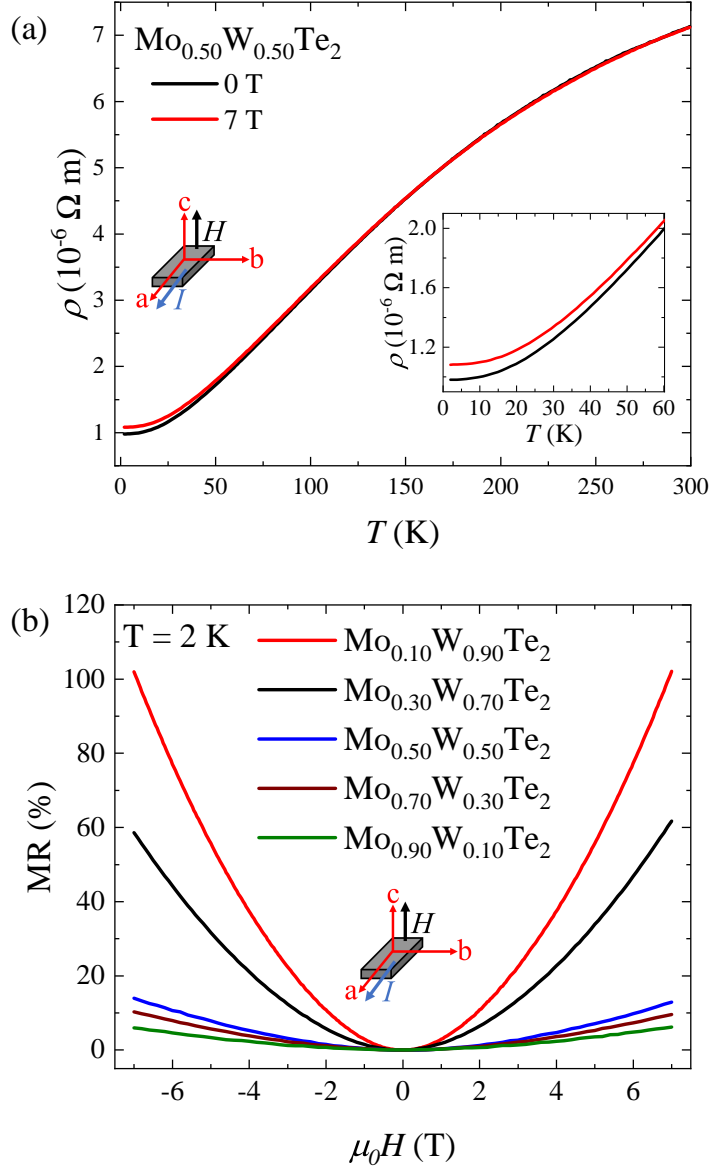


Figure 4.6: Magnetic field effects in single-crystalline $\text{Mo}_{1-x}\text{W}_x\text{Te}_2$. The electric current is applied parallel to the a axis and the magnetic field is along the c axis. (a) Temperature-dependent resistivity without and with magnetic field of 7 T in $\text{Mo}_{0.50}\text{W}_{0.50}\text{Te}_2$. Inset: low-temperature data show that the resistivity increases under field. (b) Field dependence of MR up to 7 T and at 2 K in $\text{Mo}_{1-x}\text{W}_x\text{Te}_2$ for $x = 0.10, 0.30, 0.50, 0.70,$ and 0.90 .

$\parallel c$ is shown in Figure 4.5. It also shows “turn on” behavior with $T^* \sim 26$ K under 7 T. The MR of MoTe_2 reaches $\sim 1650\%$ under 7 T at 2 K. The “turn on” and large MR behavior in MoTe_2 and WTe_2 is may be due to the electron-hole compensation caused by an electronic structure change [92].

The temperature-dependent resistivity behavior of $\text{Mo}_{0.50}\text{W}_{0.50}\text{Te}_2$ without and with magnetic field of 7 T is shown in Figure 4.6(a). Although the resistivity of $\text{Mo}_{0.50}\text{W}_{0.50}\text{Te}_2$ increases under the magnetic field, it does not exhibit the “turn on” behavior. Similar kinds of temperature-dependent resistivity behavior have been observed for all other doped $\text{Mo}_{1-x}\text{W}_x\text{Te}_2$ single crystals that we have measured. Figure 4.6(b) shows the MR of $\text{Mo}_{1-x}\text{W}_x\text{Te}_2$ for $x = 0.10, 0.30, 0.50, 0.70,$ and 0.90 . The MR increases with increasing W composition in the doped single crystals. In comparison with the parent compounds, the MR values are lower in the doped single crystals, which may be due to the electron-hole concentration asymmetry induced by doping.

4.4 Structural Transition at Ambient Pressure

When resistivity was measured from 2 K to 300 K for MoTe_2 , a clear hysteresis was observed in the cooling and warming data as shown in Figure 4.7(a). The hysteresis is associated with the first-order structural transition from the monoclinic $1T'$ phase to the orthorhombic T_d phase. The observed structural transition temperature (T_s) for MoTe_2 , which is defined as the maxima of $d\rho/dT$ during the cooling cycle, is 249 K, consistent with previous reports [29, 31, 66]. The anomaly with hysteresis was also observed during resistivity measurement of $\text{Mo}_{1-x}\text{W}_x\text{Te}_2$ for $x = 0.10, 0.30, 0.50,$

Table 4.2: Compositions and corresponding structural transition temperature (T_s) values determined by resistivity measurements.

Composition	T_s (K)
MoTe ₂	249
Mo _{0.90} W _{0.10} Te ₂	279
Mo _{0.70} W _{0.30} Te ₂	341
Mo _{0.50} W _{0.50} Te ₂	424
Mo _{0.30} W _{0.70} Te ₂	506
Mo _{0.10} W _{0.90} Te ₂	562
WTe ₂	613

0.70, 0.90, and 1 in different temperature ranges from 2 K to 650 K and the results are shown in Figures 4.7(b), 4.8(a), 4.8(b), 4.9(a), 4.9(b), and 4.10(a), respectively. The T_s values obtained from the resistivity measurements of the samples are listed in Table 4.2. With increasing tungsten composition x in Mo_{1-x}W_xTe₂, T_s linearly increases as shown in Figure 4.10(b). The observed increase in T_s with increasing W concentration across the phase diagram could be due to the following reason. It has been reported from density-functional theory (DFT) calculations that the equilibrium volume of the 1T' phase is slightly smaller than that of the T_d phase in MoTe₂ [31]. Since the atomic radius of W is slightly larger than that of Mo, the equilibrium volume of the T_d phase becomes larger with increasing W composition. When T_d phase has a larger equilibrium volume, it becomes energetically more favorable, and more active energy is required to convert the T_d phase into the 1T' phase as described in Ref. [76]. The requirement of more energy thus leads to a higher T_s with increasing W composition [69].

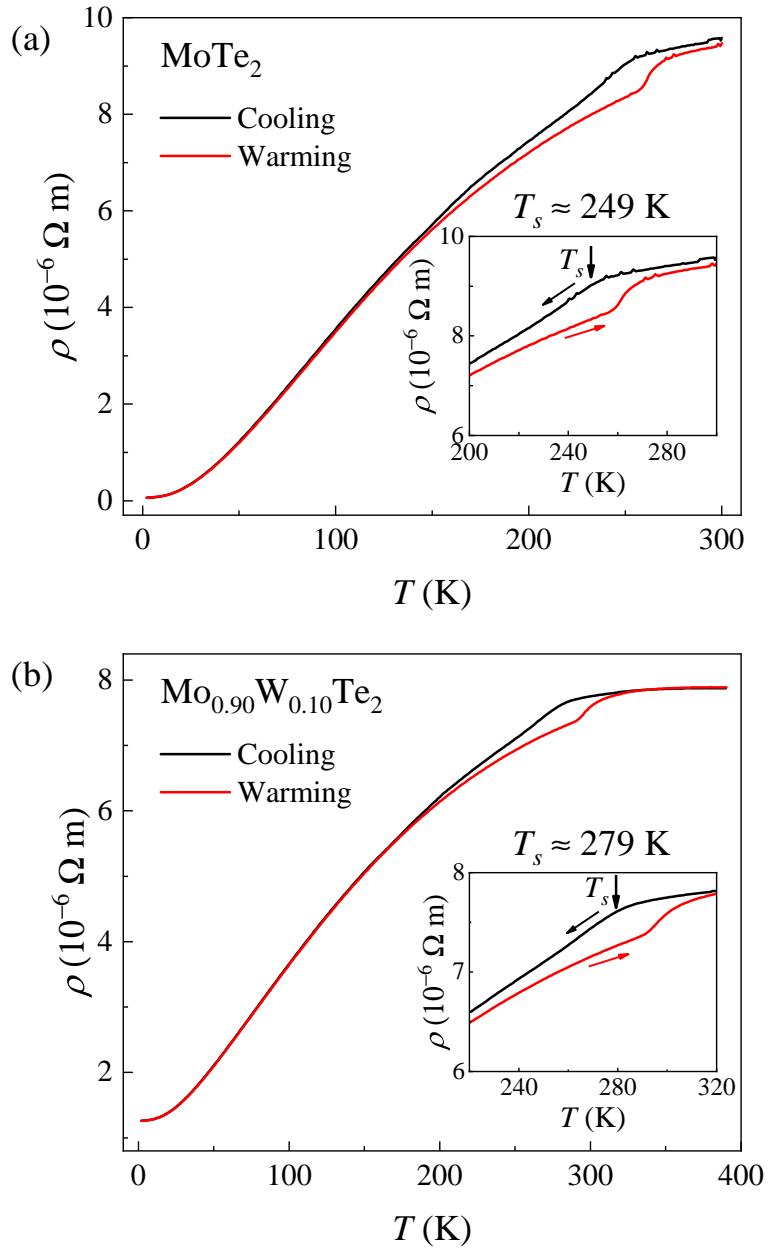


Figure 4.7: Temperature-dependent electrical resistivity during cooling and warming cycles for (a) MoTe₂ from 2 K to 300 K and (b) Mo_{0.90}W_{0.10}Te₂ from 2 K to 390 K. Insets: anomaly with thermal hysteresis associated with the structural transition from the monoclinic 1T' phase to the orthorhombic T_d phase.

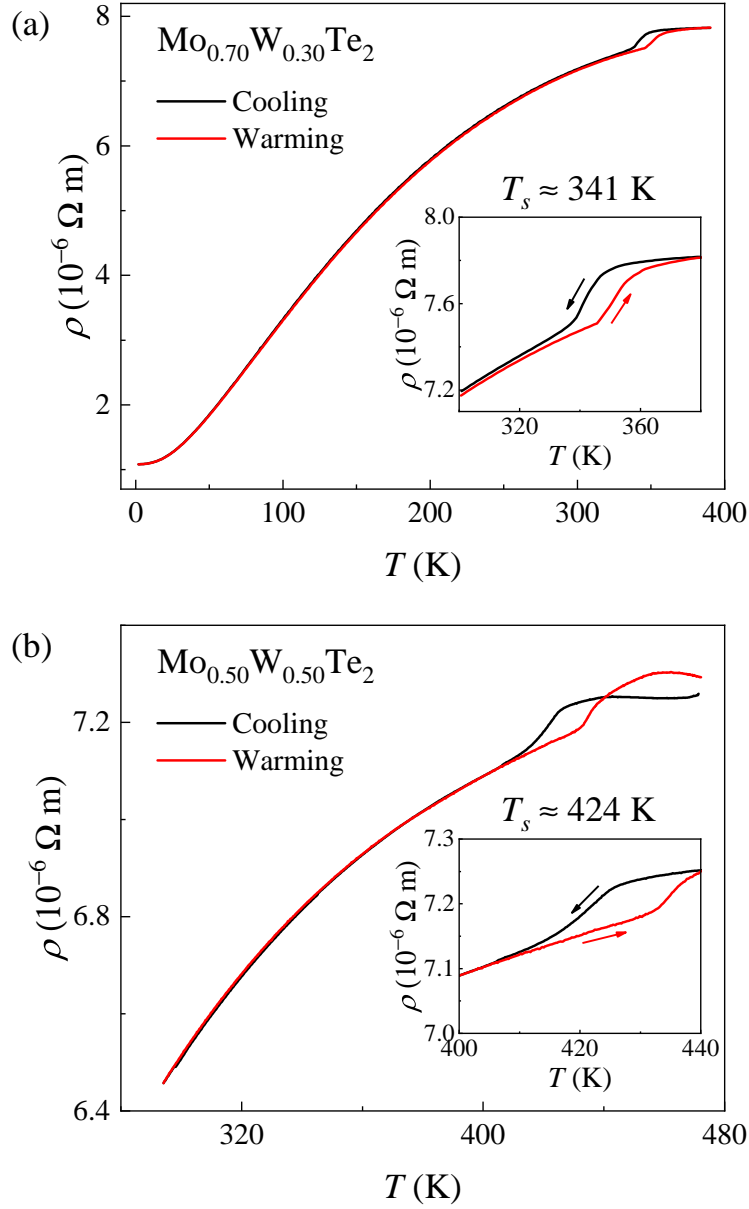


Figure 4.8: Electrical resistivity as a function of temperature during cooling and warming cycles for (a) $\text{Mo}_{0.70}\text{W}_{0.30}\text{Te}_2$ from 2 K to 390 K and (b) $\text{Mo}_{0.50}\text{W}_{0.50}\text{Te}_2$ from room temperature to 470 K. Insets: anomaly with thermal hysteresis associated with the structural transition from the monoclinic $1T'$ phase to the orthorhombic T_d phase.

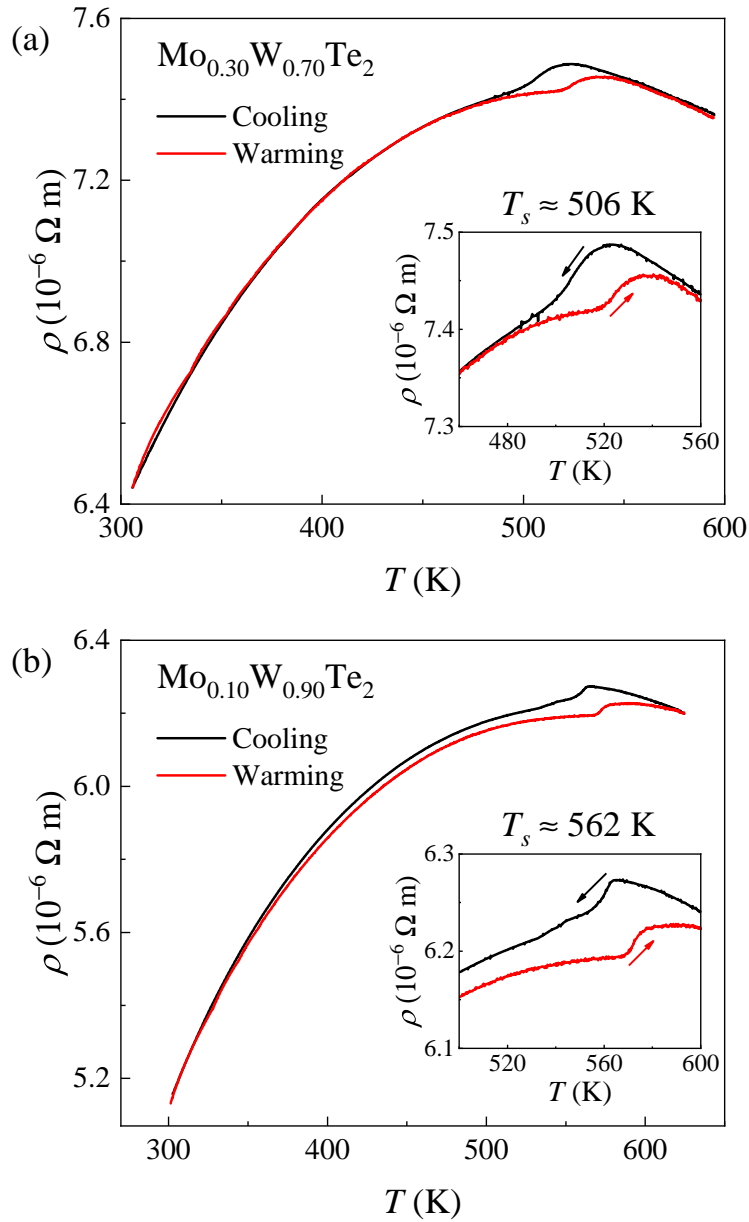


Figure 4.9: The plot of electrical resistivity as a function of temperature during cooling and warming cycles for (a) $\text{Mo}_{0.30}\text{W}_{0.70}\text{Te}_2$ from room temperature to 590 K and (b) $\text{Mo}_{0.10}\text{W}_{0.90}\text{Te}_2$ from room temperature to 620 K. Insets: anomaly with thermal hysteresis associated with the structural transition from the monoclinic $1T'$ phase to the orthorhombic T_d phase.

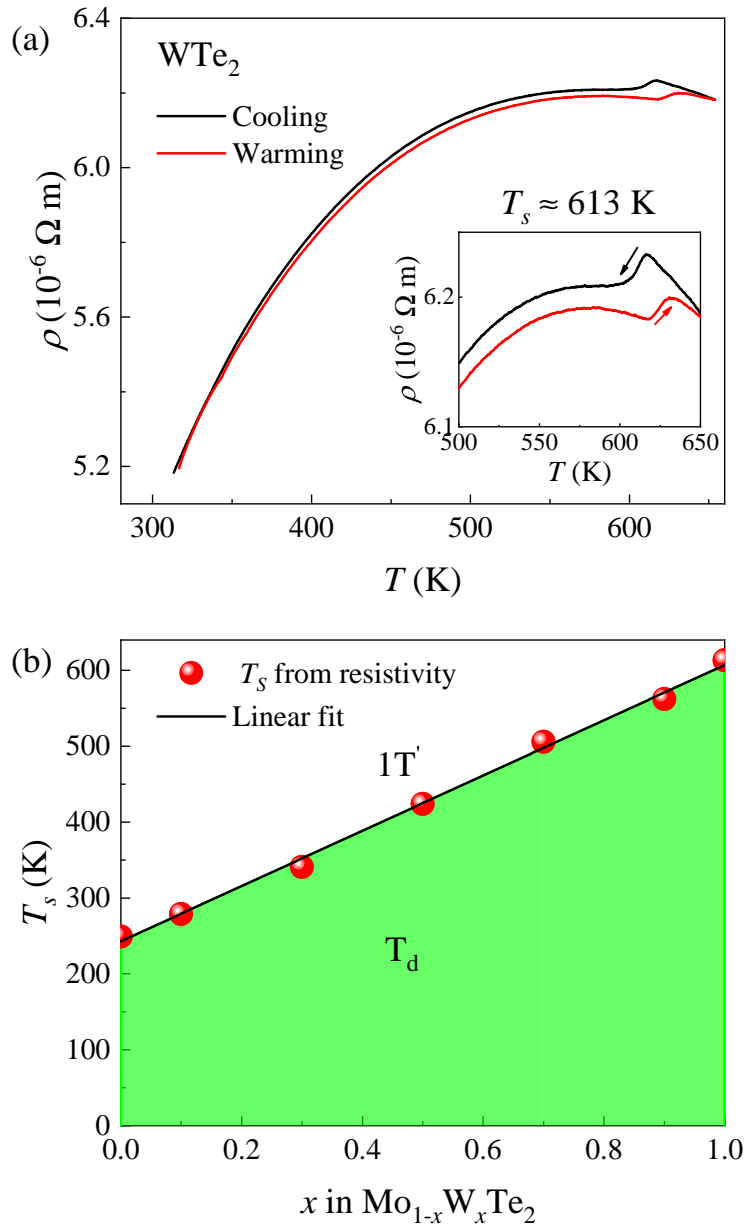


Figure 4.10: (a) Electrical resistivity as a function of temperature during cooling and warming cycles for WTe_2 from room temperature to 650 K. Insets: anomaly with thermal hysteresis associated with the structural transition from the monoclinic $1T'$ phase to the orthorhombic T_d phase. (b) Variation of structural transition temperature T_s with doping from resistivity measurements of $\text{Mo}_{1-x}\text{W}_x\text{Te}_2$. T_s is defined as the maxima of $d\rho/dT$ during the cooling cycles.

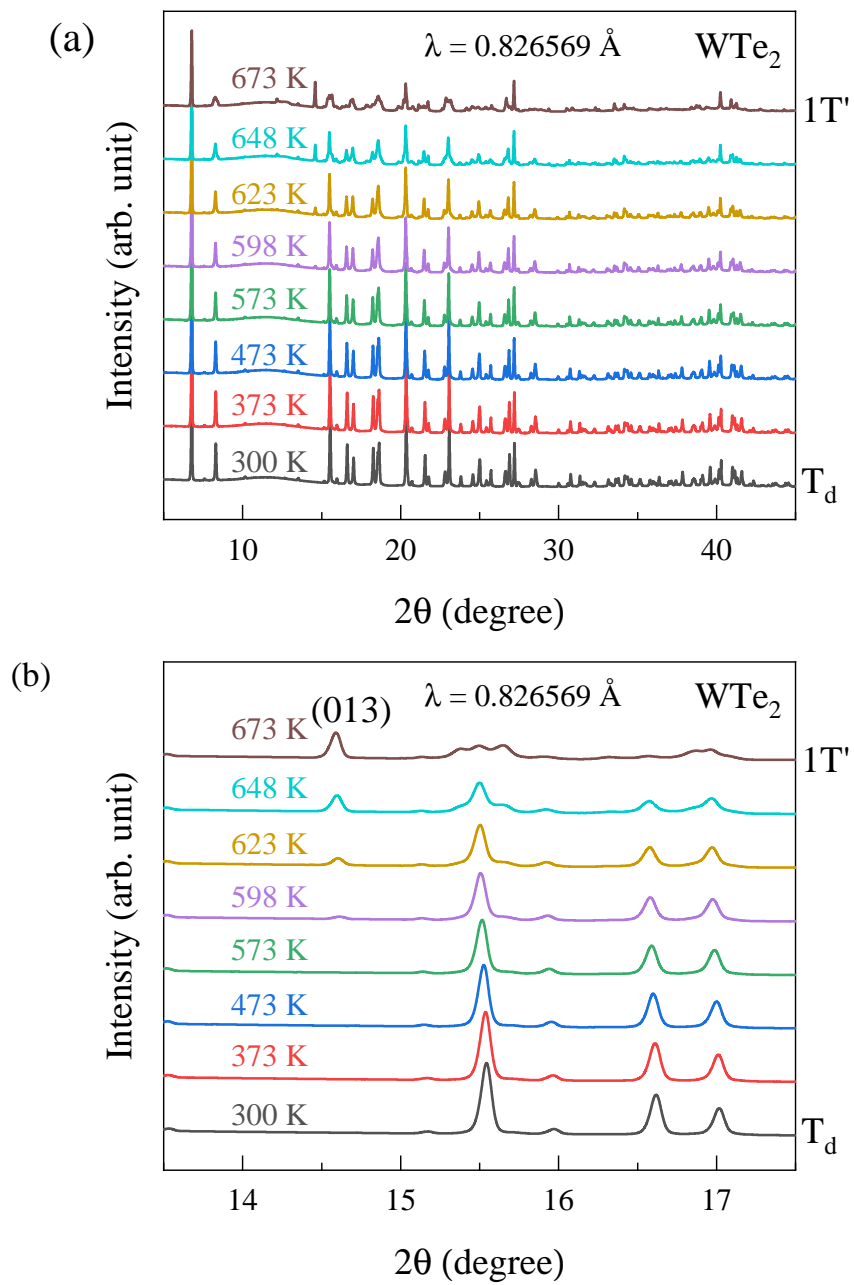


Figure 4.11: Synchrotron XRD patterns for WTe_2 for 2θ (a) from 5 to 45 degrees and (b) from 13.5 to 17.5 degrees at different temperatures.

In order to verify the structural transition obtained from the resistivity measurements and to obtain further structural information above T_s , temperature-dependent synchrotron XRD measurements in the temperature range from 300 K to 673 K were conducted on WTe_2 . Here we have selected WTe_2 since it has the highest T_s and because the structural transition in MoTe_2 has already been verified. The orthorhombic T_d phase with the non-centrosymmetric space group $\text{Pmn}2_1$ is detected at room temperature in WTe_2 , as shown in Figure 4.11(a). This result is consistent with a previous report [74]. The T_d phase persists with increasing temperature up to 573 K. When the temperature is increased to 598 K, a new Bragg reflection peak emerges, which suggests the breaking of the crystal symmetry. The observed new Bragg reflection peak was indexed as a 013 peak with the monoclinic centrosymmetric $1T'$ phase ($\text{P}2_1/\text{m}$) and is shown in Figure 4.11(b). With increasing temperature, the intensity of the 013 peak also increases, indicating the development of the $1T'$ phase. The structure is completely transformed to the $1T'$ phase when the temperature reaches to 673 K. Thus, the temperature-dependent synchrotron XRD results for WTe_2 support our resistivity measurement data [69].

4.5 High-Pressure Study using Beryllium-Copper Clamp Cell

At ambient pressure, $\text{Mo}_{0.90}\text{W}_{0.10}\text{Te}_2$ exhibits a resistivity (ρ) anomaly at T_s associated with the structural transition, as shown in Figure 4.12(a). The ρ anomaly at T_s is characteristic of the structural $1T'$ -to- T_d phase transition. With increasing

pressure up to 13.52 kbar, the T_s is increasingly suppressed. At 17.71 kbar, the T_s is no longer observable. The evolution of the structural transition with pressure can be clearly seen in the hysteresis effects as presented in Figure 4.13. As shown in the inset to Figure 4.12(a), a slight drop in ρ is observed at 3.89 kbar at 1.26 K. With increasing pressure, this ρ drop becomes more pronounced and reaches zero at 13.52 kbar, indicating the emergence of superconductivity at a transition temperature $T_c \sim 2.7$ K. The T_c continues to increase with further increasing pressure, and a T_c of 3.6 K is reached at 17.71 kbar [69].

Figure 4.14(a) shows the temperature-dependent resistivity from room temperature down to 1.25 K for $\text{Mo}_{0.60}\text{W}_{0.40}\text{Te}_2$ under different pressures. Initially, no structural transition was detected in this compound at ambient pressure. However, a structural transition was observed with T_s around 244 K under 3.28 kbar. The T_s continuously decreases with further increasing pressure and reaches to ~ 65 K at 16.66 kbar. Both warming and cooling cycles under different pressures are plotted in Figure 4.15, which clearly shows the evolution of the structural transition under pressure. As shown in the inset to Figure 4.14(a), superconductivity was observed at 1.59 K around 8.35 kbar and T_c continuously increases to 2.6 K with further increasing pressure [69].

No structural transition was detected for $\text{Mo}_{0.25}\text{W}_{0.75}\text{Te}_2$ at ambient pressure from room temperature down to 1.25 K, as shown in Figure 4.16(a). With increasing pressure, the overall resistivity decreases. When pressure of ~ 12.32 kbar was applied, a ρ anomaly appeared at around 245 K. This anomaly is associated with a first-order structural transition [29]. Figure 4.17 clearly shows the hysteresis effects, supporting

the structural transition. With further increasing pressure, the T_s is suppressed to around 180 K at 17.05 kbar, but superconductivity was not observed down to 1.25 K [69].

Figures 4.12(b), 4.14(b), and 4.16(b) show the temperature - pressure ($T - P$) phase diagrams of $\text{Mo}_{1-x}\text{W}_x\text{Te}_2$ for $x = 0.10$, $x = 0.40$, and $x = 0.75$, respectively. Increasing pressure continuously suppresses the T_s in all three compounds we have studied. Our observation also shows that to suppress the T_s to below room temperature for $x \geq 0.40$, pressures higher than 3.28 kbar are required. As previously reported, a structural transition in WTe_2 has been observed at room temperature under pressures of 4 to 6 GPa [78, 79]. In addition, it has also been found that the T_s of MoTe_2 is suppressed to lower temperature under pressure [32, 33]. These observations support the existence of a structural transition in $\text{Mo}_{1-x}\text{W}_x\text{Te}_2$ at ambient pressure for all x , with higher T_s at higher W concentration. Among these three compounds, superconductivity was observed for $x = 0.10$ and $x = 0.40$. The T_c increases with increasing pressure and the dT_c/dP is 0.17 K/kbar for $x = 0.10$ and 0.11 K/kbar for $x = 0.40$ [69].

The following observations support the competition between the structural transition and superconductivity in $\text{Mo}_{1-x}\text{W}_x\text{Te}_2$. T_s continuously decreases with increasing pressure in all three compounds we have studied, as shown in Figures 4.12(b), 4.14(b), and 4.16(b). Superconductivity emerges once the T_s is suppressed to < 175 K (e.g. for $x = 0.10$ with a $T_c = 1.26$ K under 3.89 kbar and for $x = 0.40$ with a $T_c = 1.59$ K under 8.35 kbar). An increase in the T_c is coupled with the decrease of the T_s .

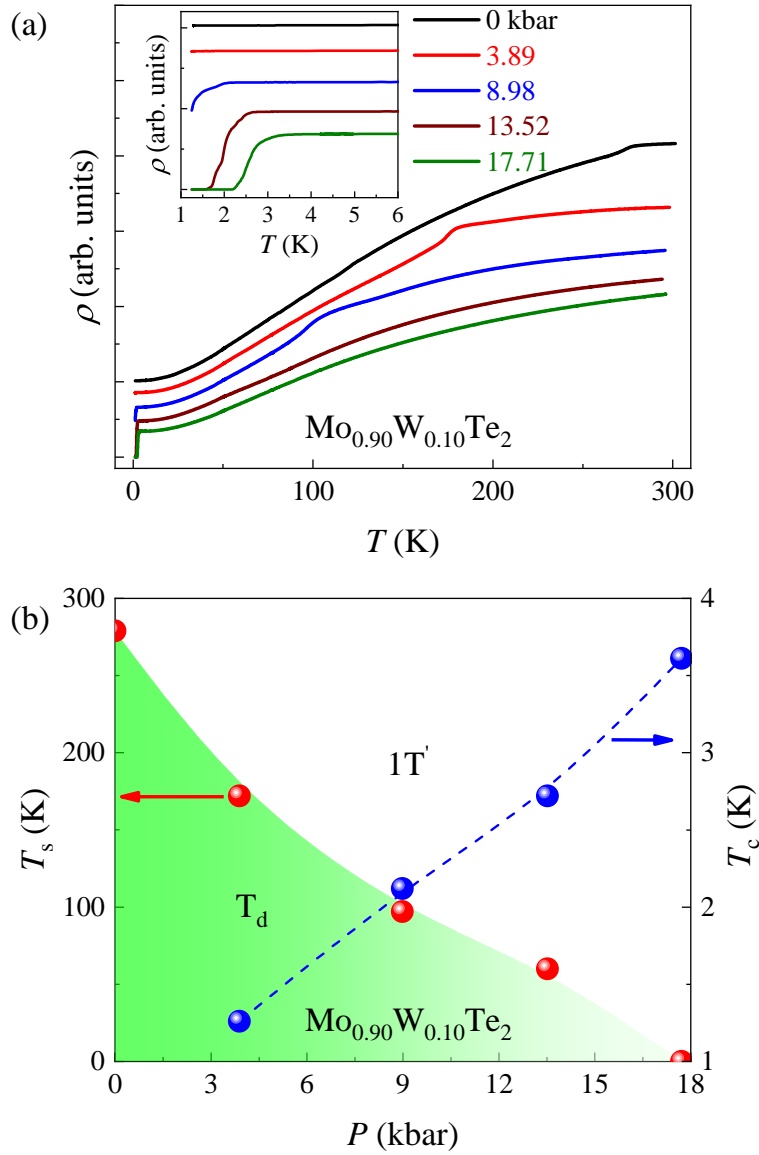


Figure 4.12: High-pressure effects on $\text{Mo}_{0.90}\text{W}_{0.10}\text{Te}_2$. (a) Electrical resistivity as a function of temperature for different pressures in the range of 0–17.71 kbar. Resistivity curves are shifted vertically for clarity. The anomaly in the resistivity corresponds to the structural transition from the monoclinic $1T'$ phase to the orthorhombic T_d phase. Inset: low-temperature data. (b) Pressure-dependent structural and superconducting transition temperatures (red and blue spheres, respectively).

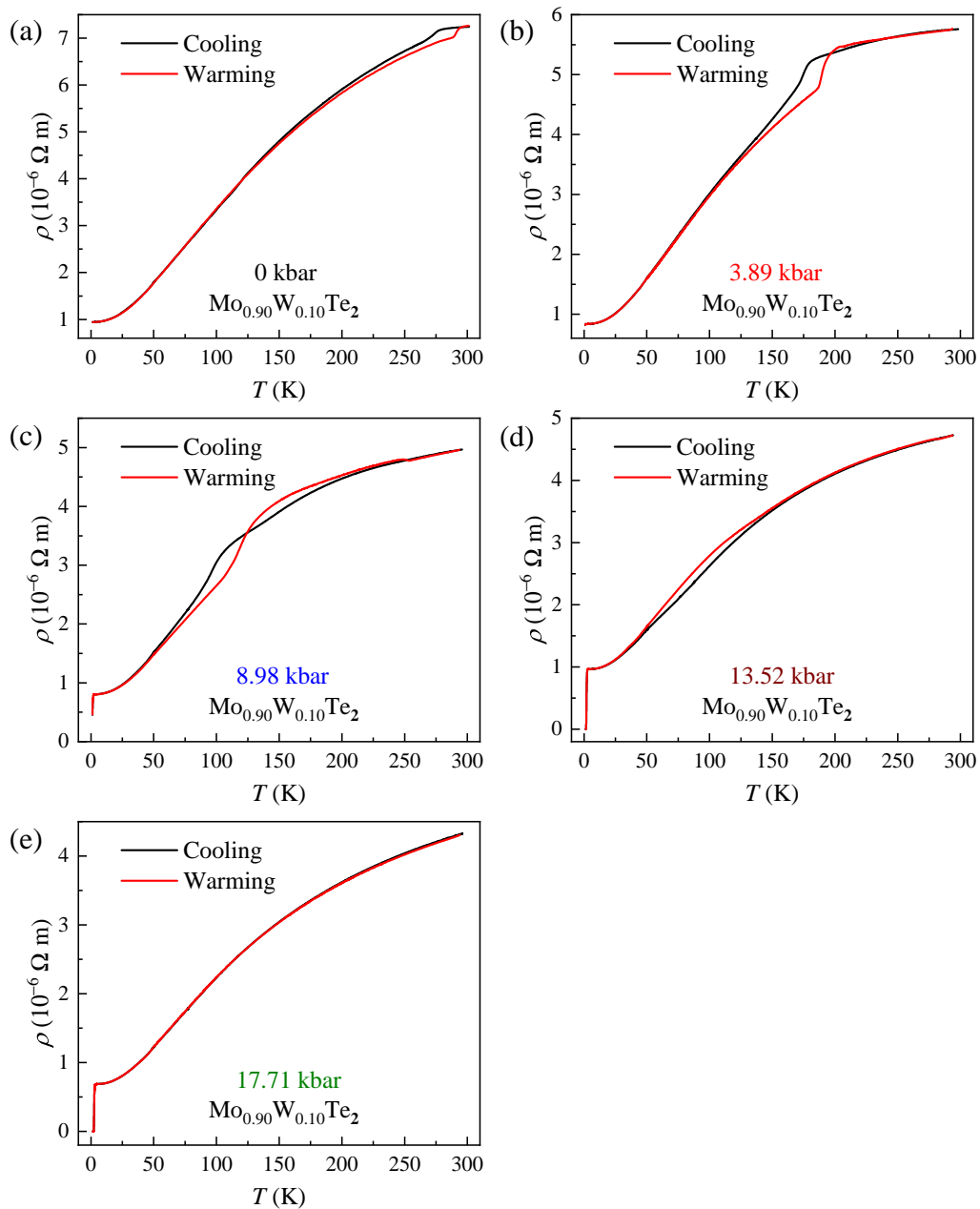


Figure 4.13: Temperature-dependent resistivity of $\text{Mo}_{0.90}\text{W}_{0.10}\text{Te}_2$ under (a) 0 kbar, (b) 3.89 kbar, (c) 8.98 kbar, (d) 13.52 kbar, and (e) 17.71 kbar. Anomalies with thermal hysteresis under 0 kbar, 3.89 kbar, 8.98 kbar, and 13.52 kbar are associated with structural transitions.

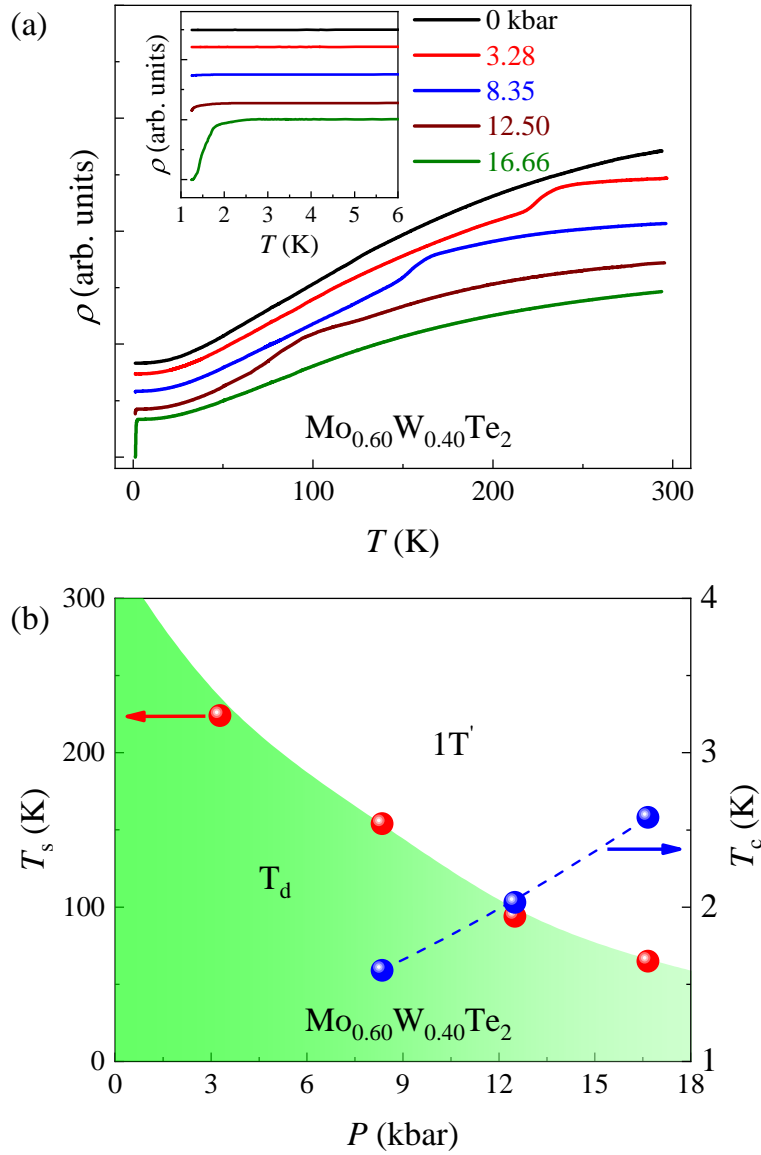


Figure 4.14: High-pressure effects on $\text{Mo}_{0.60}\text{W}_{0.40}\text{Te}_2$. (a) Electrical resistivity as a function of temperature for different pressures in the range of 0–16.66 kbar. Resistivity curves are shifted vertically for clarity. The anomaly in the resistivity corresponds to the structural transition from the monoclinic $1T'$ phase to the orthorhombic T_d phase. Inset: low-temperature data. (b) Pressure-dependent structural and superconducting transition temperatures (red and blue spheres, respectively).

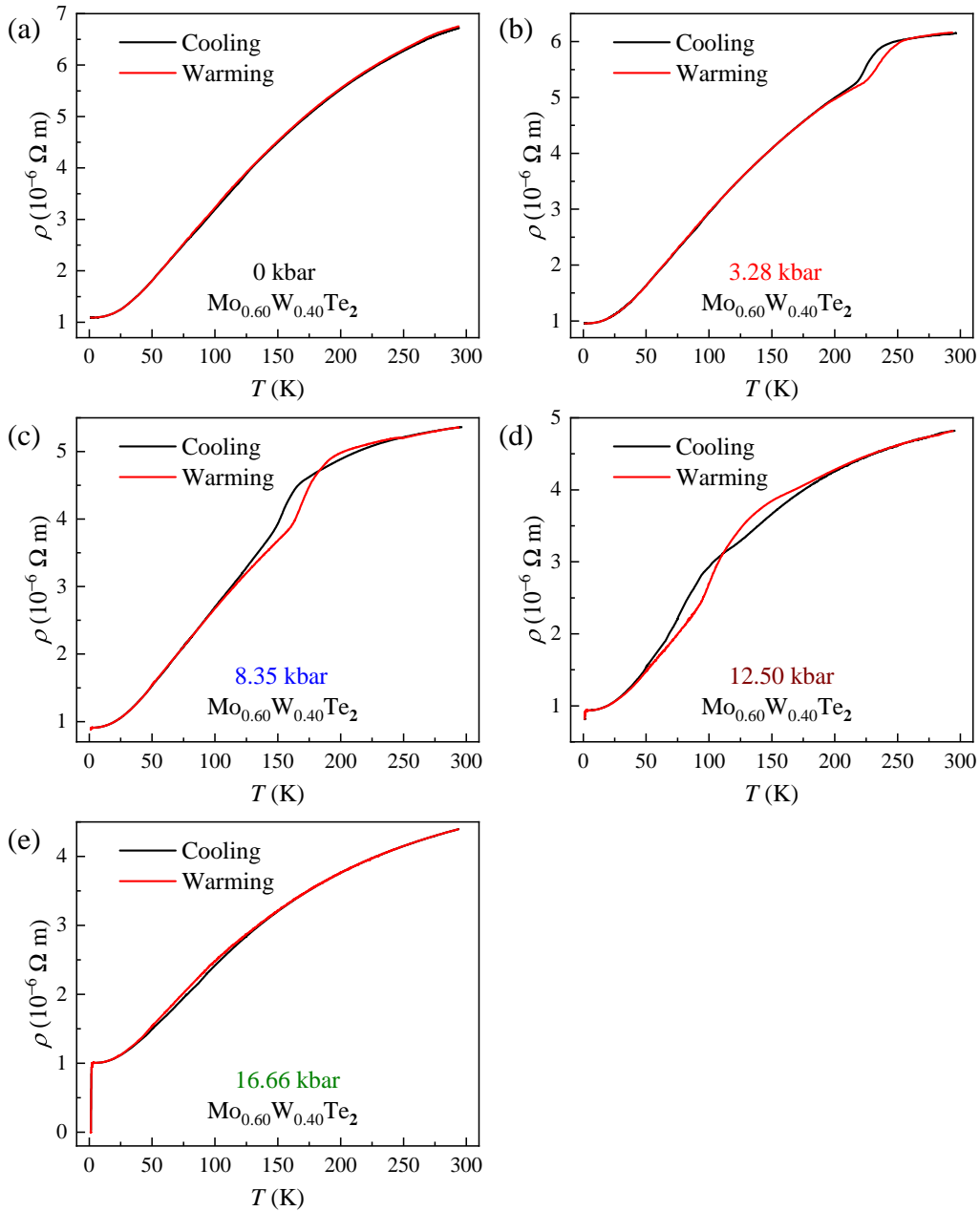


Figure 4.15: Evolution of structural transition under pressure on $\text{Mo}_{0.60}\text{W}_{0.40}\text{Te}_2$. Temperature-dependent resistivity under (a) 0 kbar, (b) 3.28 kbar, (c) 8.35 kbar, (d) 12.50 kbar, and (e) 16.66 kbar. Anomalies with thermal hysteresis under 3.28 kbar, 8.35 kbar, 12.50 kbar, and 16.66 kbar are associated with structural transitions.

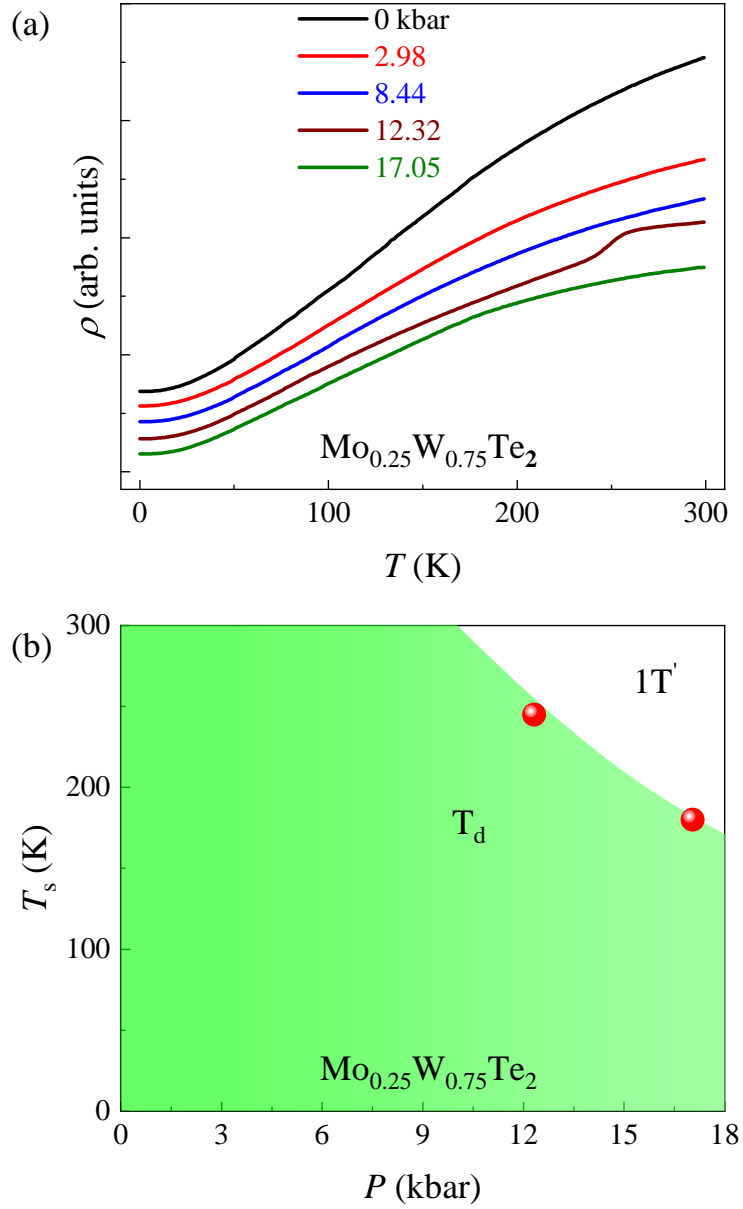


Figure 4.16: (a) Electrical resistivity of single-crystalline $\text{Mo}_{0.25}\text{W}_{0.75}\text{Te}_2$ as a function of temperature for different pressures in the range of 0–17.05 kbar. Resistivity curves are shifted vertically for clarity. (b) Pressure-dependent structural transition temperatures of $\text{Mo}_{0.25}\text{W}_{0.75}\text{Te}_2$.

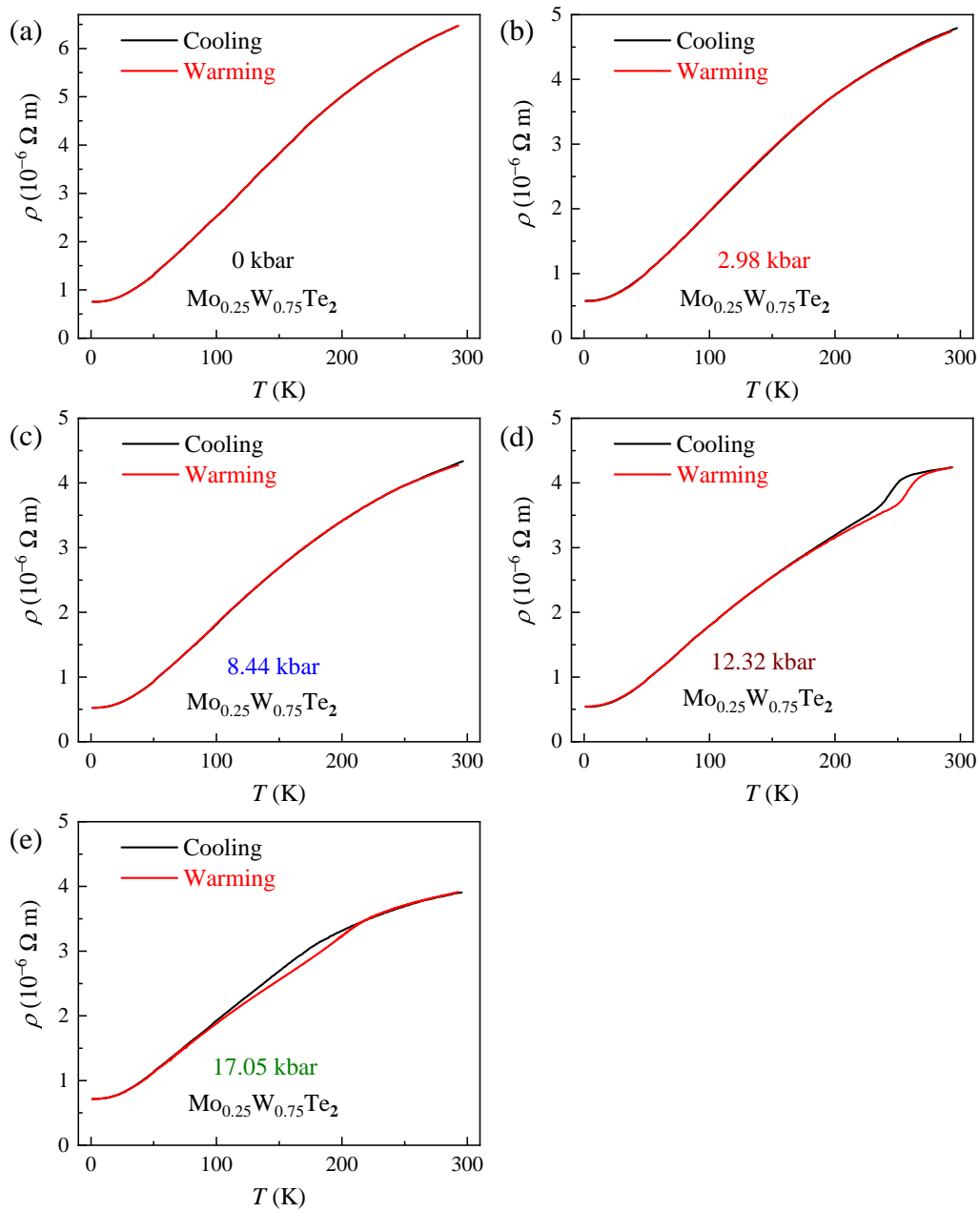


Figure 4.17: Temperature-dependent resistivity of $\text{Mo}_{0.25}\text{W}_{0.75}\text{Te}_2$ under (a) 0 kbar, (b) 2.98 kbar, (c) 8.44 kbar, (d) 12.32 kbar, and (e) 17.05 kbar. Anomalies with thermal hysteresis under 12.32 kbar and 17.05 kbar are associated with structural transitions.

For $x = 0.75$, superconductivity was not observed down to 1.25 K and applying pressures up to 17 kbar with the suppression of the T_s down to ~ 180 K. Previous studies of MoTe_2 have shown that pressure continuously suppresses T_s [31, 33, 93] and that in the pressure range from 2.7 to 7.5 kbar, a sharp increase in T_c is observed [32]. A pressure induced structural transition in WTe_2 at room temperature was previously reported [78, 79]. However, our observation shows a structural transition at ambient pressure in WTe_2 with $T_s = 613$ K; therefore, the previously reported structural transition at room temperature in WTe_2 under pressure is more likely related to suppression of the structural transition from higher temperature with increasing pressure rather than being induced by pressure. By conducting temperature-dependent X-ray measurements, Clarke *et al.* reported that although the structural transition in MoTe_2 at ambient pressure occurs around 250 K, two phases coexist in an extended temperature range from 233 K to 290 K [30]. Heikes *et al.* have also shown that the $1T'$ and T_d phases co-exist in MoTe_2 at 1.5 K and under hydrostatic pressure of 1 GPa [33]. From the observations discussed above, it can be concluded that, once the T_s in $\text{Mo}_{1-x}\text{W}_x\text{Te}_2$ is suppressed by pressure to below the critical temperature, completion of the structural transition occurs at very low temperature, after which the T_c sharply increases with further increasing pressure. These observations shed light on the possible origin(s) for the superconductivity in the $\text{Mo}_{1-x}\text{W}_x\text{Te}_2$ system, such as the competition between the superconductivity and the structural transition, and/or the co-existence of different phases [69].

It has been shown from total energy calculations, including the van der Waals interaction, that the T_d phase is energetically more stable than the $1T'$ phase [94].

The energy differences between the T_d and $1T'$ phases in MoTe_2 and WTe_2 are 0.40 and 0.46 meV per unit cell, respectively. This suggests that WTe_2 requires higher energy than MoTe_2 for the transition from the T_d phase to the $1T'$ phase. It has been reported that the interlayer contraction increases the hybridization between the Te p_z orbitals, which leads to the enhancement of the three-dimensionality of the band character [88]. Since the atomic radius of W is larger than that of Mo, an increase in W content expands the interlayer distance in $\text{Mo}_{1-x}\text{W}_x\text{Te}_2$ and reduces interlayer hybridization. The total kinetic energy of the electron increases as interlayer hybridization decreases [32]. The increase in kinetic energy leads to an increase in the total energy, assuming that the rest changes negligibly. Thus, the energy difference between the T_d phase and the $1T'$ phase increases with increasing W composition. When the energy difference is larger, higher energy (and hence higher temperature) is required for the transition from the T_d phase to the $1T'$ phase, which explains the increasing T_s with increasing W content as shown in Figure 4.10 (b). On the other hand, the application of external pressure reduces the interlayer distance and enhances the interlayer hybridization, which leads to a lower T_s and favors superconductivity [69].

When pressure is applied to $\text{MoTe}_2/\text{WTe}_2$, the interlayer Te-Te distance is suppressed while, due to the anisotropy of the van der Waals structure, the intralayer Mo-Te/W-Te [31,79] bond length remains almost unchanged. P. Lu *et al.* [79] pointed out that one transverse acoustic vibrational mode, mainly from Te-Te interlayer vibrations, contributes significantly to the electron-phonon coupling. It is thus natural to suggest that the pressure effect on $\text{Mo}_{1-x}\text{W}_x\text{Te}_2$ also leads to the softening of the

interlayer Te-Te vibration modes. Using a modified McMillan formula, the superconducting transition temperature T_c can be estimated as [95]:

$$T_c = \frac{\langle\omega\rangle}{1.20} \exp\left(-\frac{1.04(1+\lambda)}{\lambda - \mu^*(1+0.62\lambda)}\right), \quad (4.1)$$

where the parameter $\langle\omega\rangle$ is the average of phonon energy defined as $\langle\omega\rangle = \frac{2}{\lambda} \int_0^\infty d\omega \alpha^2 F(\omega)$, μ^* is the Coulomb pseudopotential, and λ is the dimensionless electron-phonon coupling strength. λ in terms of the Eliashberg electron-phonon spectral function $\alpha^2 F(\omega)$ is expressed as $\lambda = 2 \int_0^\infty d\omega \alpha^2 F(\omega)/\omega$, where α^2 is an average of the electron-phonon interaction, $F(\omega)$ is the phonon density of states, and ω is the phonon frequency. The phonon softening can result in an increase in the superconducting transition temperature, which could possibly be the origin of the emergence of superconductivity in $\text{Mo}_{1-x}\text{W}_x\text{Te}_2$ under high pressure [69].

4.6 High-Pressure Study using Diamond Anvil Cell

Magnetotransport properties of $\text{Mo}_{0.50}\text{W}_{0.50}\text{Te}_2$ under pressure have been investigated using a diamond anvil cell (DAC). Figure 4.18(a) shows the temperature-dependent resistance under different pressures. With increasing pressure, the electrical resistance is suppressed over the entire temperature range. The low-temperature data for different pressures are shown in Figures 4.18(b) and 4.18(c). During loading, superconductivity appears under 1.1 GPa with a superconducting transition temperature (T_c) of 2.6 K. The T_c continuously increases with increasing pressure and reaches a maximum value of 5.8 K under 14.3 GPa. With the further application

Table 4.3: The upper critical field determined by using Werthamer-Helfand-Hohenberg (WHH) approximation at different pressures.

P (GPa)	$H_{c2}(0)^{WHH}$ (T)
1.1	1.14
5.9	1.60
14.3	2.18
23.5	1.71
35.8	1.07

of pressure, the T_c remains constant and starts to decrease at 17.5 GPa. The rate of change in T_c is 0.24 K/GPa in the pressure range of 1.1 to 14.3 GPa and -0.14 K/GPa from 15.7 GPa to 42.3 GPa.

To determine the value of the upper critical field (H_{c2}), we carried out resistance measurements around T_c for various magnetic fields. As shown in Figure 4.19 (a), the T_c gradually decreases with increasing magnetic field and disappears at 2 T when measured under 5.9 GPa. Similar kinds of behavior are observed when measured under other pressures, for example 14.3 GPa as shown in Figure 4.19(b). Figure 4.19(c) shows the plot of H_{c2} vs T_c under various pressures. The data points show the linear dependence of T_c with H_{c2} and the solid curves are linear fits of the data. From the linear extrapolation of each curve, the upper critical field $H_{c2}(0)^{linear}$ can be obtained. By using the Werthamer-Helfand-Hohenberg (WHH) approximation:

$$H_{c2}(0)^{WHH} = 0.691 \times H_{c2}(0)^{linear}, \quad (4.2)$$

the upper critical field at each pressure was then determined. The obtained $H_{c2}(0)^{WHH}$ values at various pressures are listed in Table 4.3.

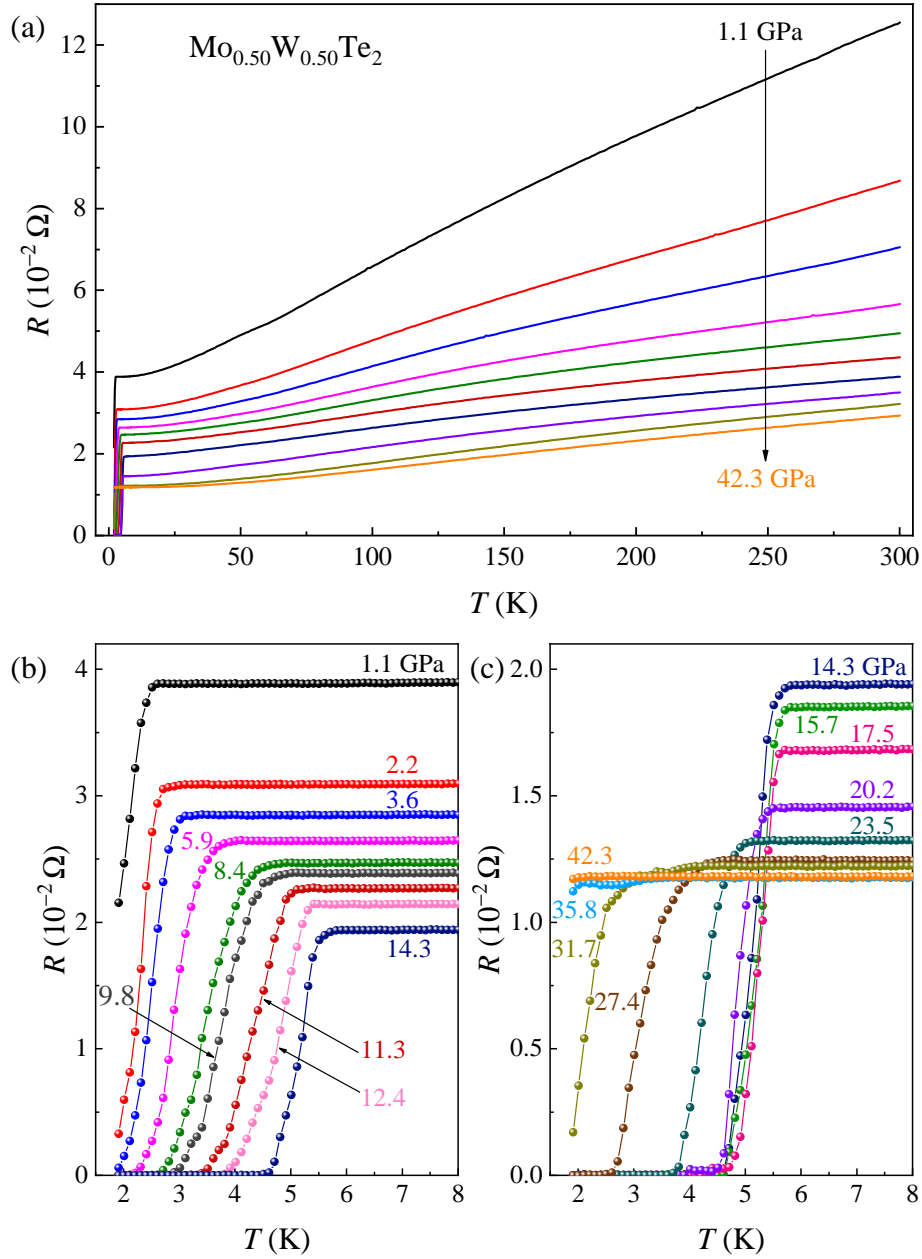


Figure 4.18: (a) Electrical resistance as a function of temperature for $\text{Mo}_{0.50}\text{W}_{0.50}\text{Te}_2$ under pressures ranging from 1.1 to 42.3 GPa. Electrical resistance below 8 K under pressures of (b) 1.1 – 14.3 and (c) 14.3 – 42.3 GPa. Drops in the electrical resistance and zero-resistance behavior are both clearly observed.

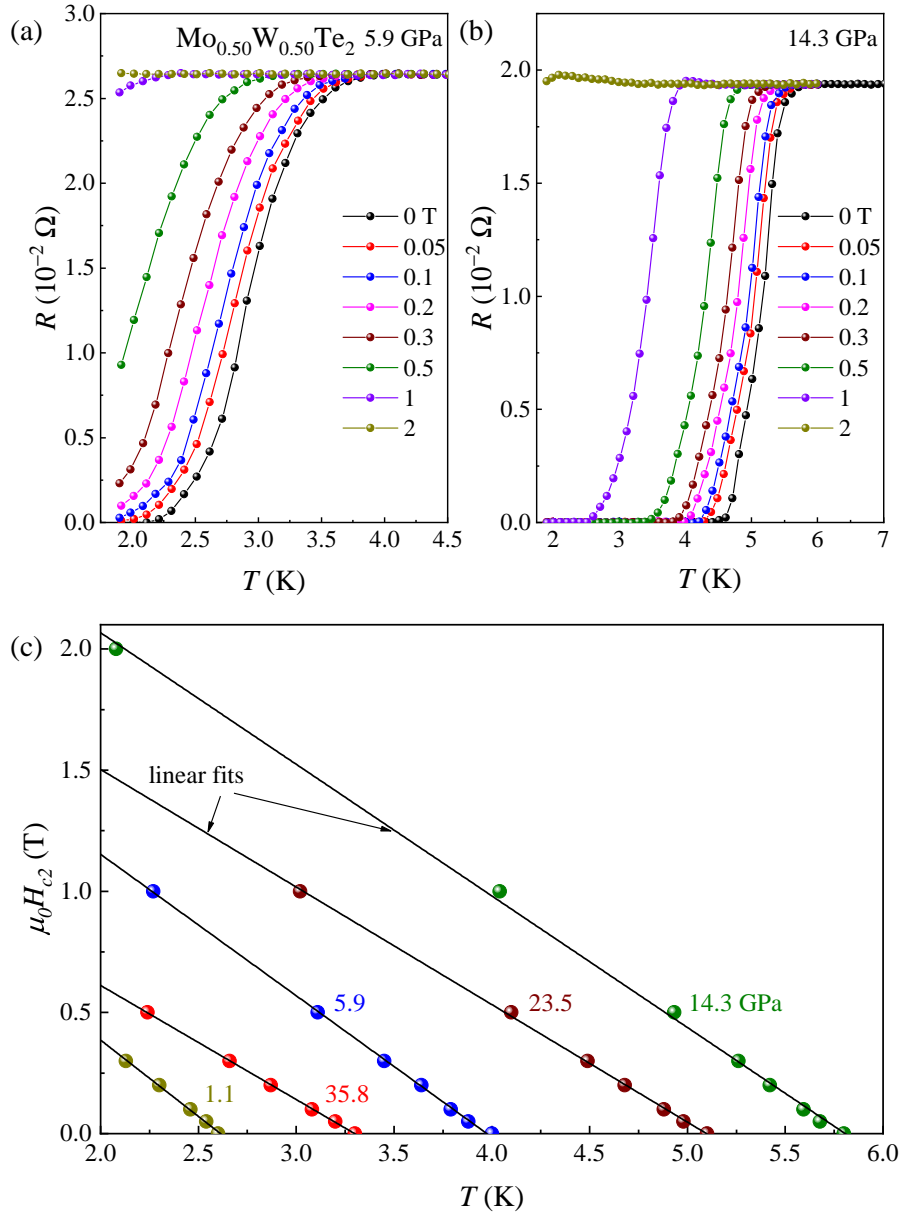


Figure 4.19: Upper critical field (H_{c2}) analysis of the superconducting $\text{Mo}_{0.50}\text{W}_{0.50}\text{Te}_2$. Temperature dependence of electrical resistance under different magnetic fields up to 2 T under (a) 5.9 GPa and (b) 14.3 GPa. (c) H_{c2} as a function of temperature under different pressures. Solid lines are the linear fits of the experimental data.

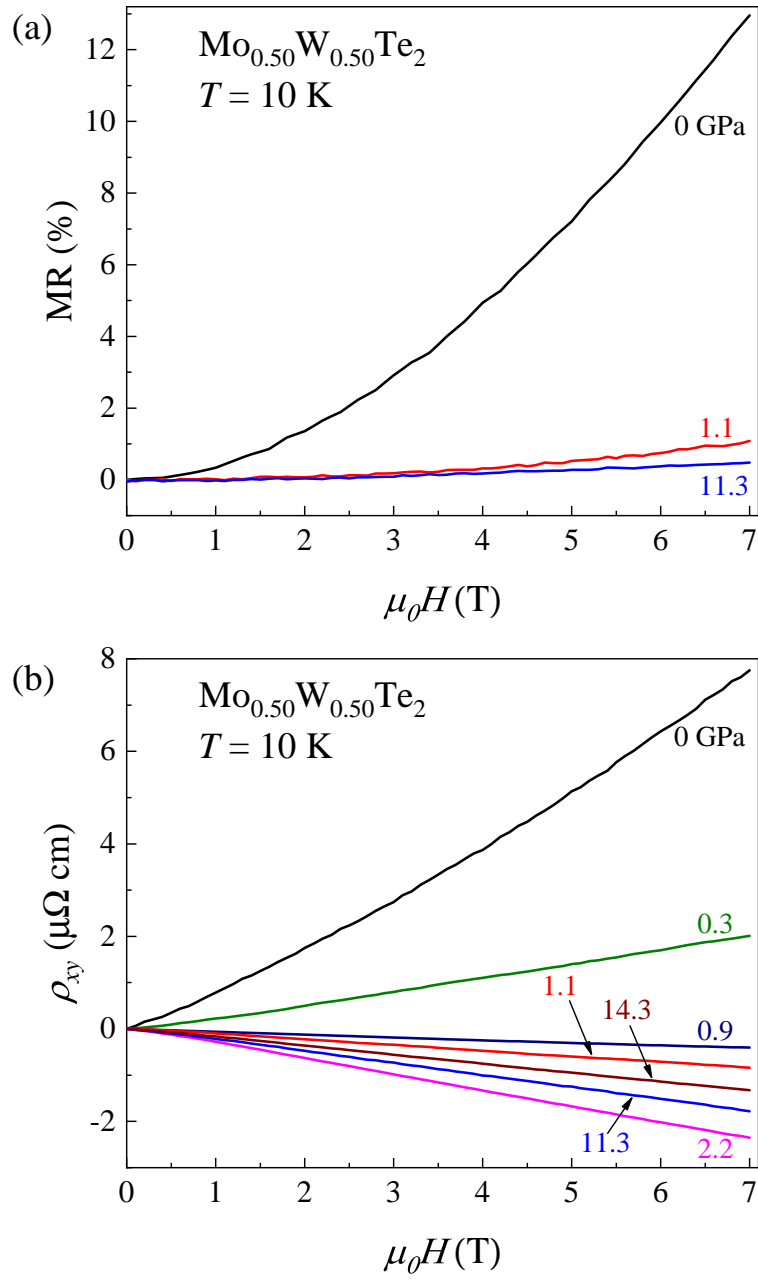


Figure 4.20: Magnetic-field-dependent (a) MR and (b) Hall resistivity of $\text{Mo}_{0.50}\text{W}_{0.50}\text{Te}_2$ under different pressures at 10 K.

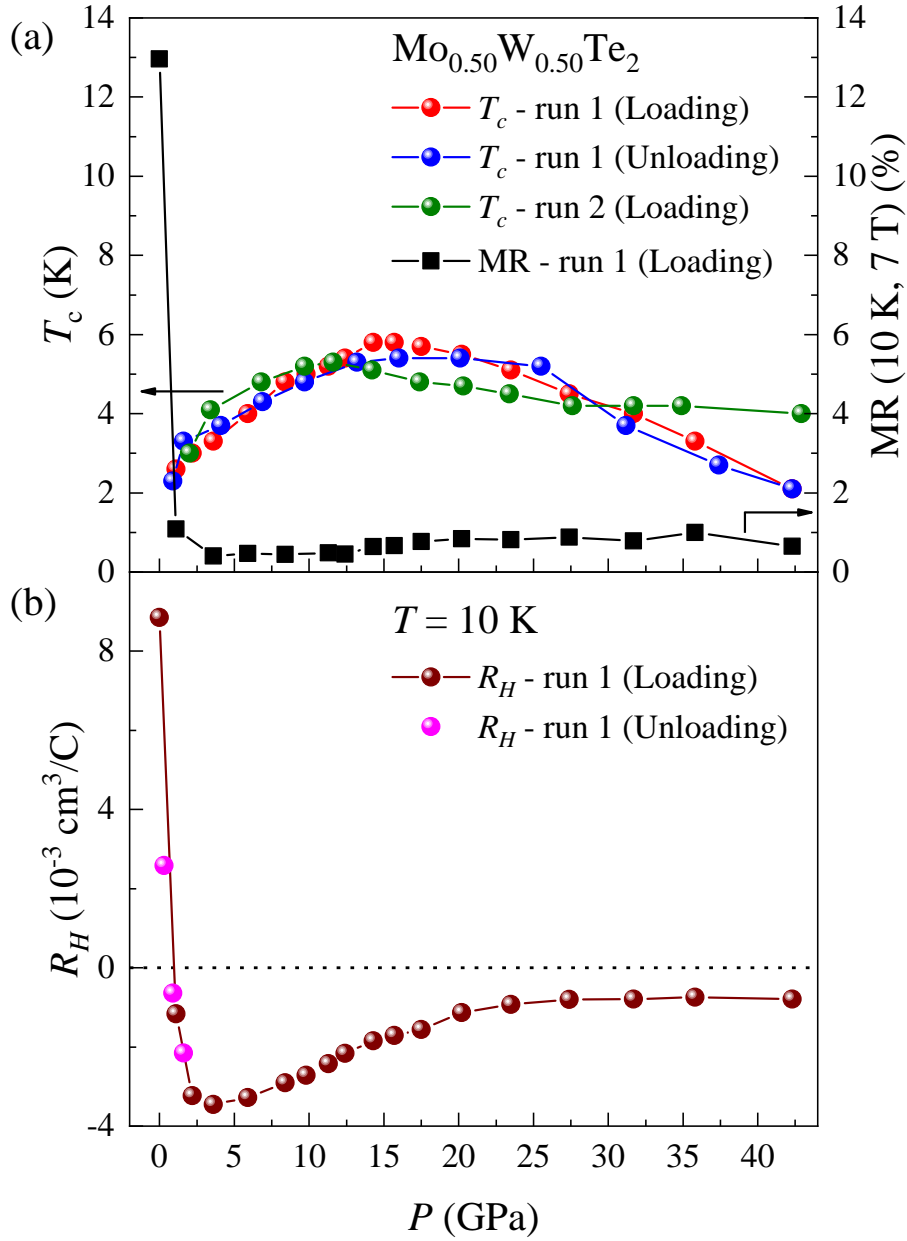


Figure 4.21: Phase diagram of $\text{Mo}_{0.50}\text{W}_{0.50}\text{Te}_2$ under pressure. (a) T_c (left axis) and MR at 10 K under magnetic field of 7 T (right axis) plotted against pressure for different runs of pressure loading and unloading. (b) Pressure loading and unloading for pressure-dependent Hall coefficient (R_H) at 10 K.

Magnetoresistance (MR) and Hall effect measurements of $\text{Mo}_{0.50}\text{W}_{0.50}\text{Te}_2$ were performed under different pressures by applying magnetic fields up to 7 T at 10 K. Magnetic-field-dependent MR under different pressures is shown in Figure 4.20(a). Suppression of the MR in $\text{Mo}_{0.50}\text{W}_{0.50}\text{Te}_2$ is observed under pressure. Figure 4.20(b) shows the plot of Hall resistivity (ρ_{xy}) vs magnetic field under different pressures. With increasing pressure, the Hall resistivity decreases and first becomes negative under 0.9 GPa.

As shown in Figure 4.21(a) (left axis), dome-shaped superconducting behavior is observed under pressure for $\text{Mo}_{0.50}\text{W}_{0.50}\text{Te}_2$. There is a discrepancy in the T_c between run-1 and run-2, which might be due to different reasons. The pressure medium used was quasi-hydrostatic, so it may vary from one experiment to another and lead to the discrepancy in the T_c . The difference in the sample thickness between different runs could also cause the T_c variation. Sample dimensions were $90 \times 90 \times 22 \mu\text{m}^3$ in run 1 and $90 \times 90 \times 14 \mu\text{m}^3$ in run 2.

Pressure-dependent MR at 10 K and under magnetic field of 7 T is shown in Figure 4.21(a) (right axis). At ambient pressure, the MR (10 K, 7 T) is $\sim 13\%$, while under 1.1 GPa, it is suppressed to $\sim 1\%$ and superconductivity appears. The MR (10 K, 7 T) remains almost constant with further increasing pressure. In the parent compounds, MoTe_2 and WTe_2 , similar kinds of dome-shaped superconducting behavior and MR suppression under pressure have been reported [31, 72, 77, 93].

Figure 4.21(b) shows the pressure dependence of the Hall coefficient (R_H). Here, the R_H s are extracted by fitting the ρ_{xy} data [some of the representative ρ_{xy} values are shown in Figure 4.20(b)] using the equation $\rho_{xy} = R_H \times (\mu_0 H) + \beta \times (\mu_0 H)^3$,

where β provides the nonlinearity in the ρ_{xy} values. R_H has a positive value at ambient pressure. When pressure of 1.1 GPa is applied during loading, the R_H becomes negative and superconductivity appears. R_H remains negative with further increasing pressure over the entire pressure range. During unloading, the R_H remains negative down to the pressure of 0.9 GPa and the superconductivity remains with $T_c \sim 2.3$ K. When pressure is released to 0.3 GPa, the R_H becomes positive and superconductivity is not observed in temperature measurements down to 1.9 K. By applying pressure at a particular value, the critical pressure, R_H changes sign and superconductivity appears. This observation indicates that there is a significant reconstruction of the Fermi surface, which may be associated with anisotropic reductions of the lattice parameter under pressure as reported in Ref. [77].

Chapter 5

Conclusion

In this work, we have grown single crystals of the Weyl semimetal $\text{Mo}_{1-x}\text{W}_x\text{Te}_2$ for $x = 0, 0.10, 0.30, 0.40, 0.50, 0.70, 0.75, 0.90,$ and 1 and have characterized them using energy dispersive X-ray spectroscopy (EDS) and X-ray diffraction (XRD). Their composition-dependent magnetotransport properties and structural transitions have been investigated, along with high-pressure effects on the single crystals.

Single crystals of the parent compounds MoTe_2 and WTe_2 were grown by the self-flux method, whereas the doped single crystals were grown using the chemical vapor transport (CVT) method. Based on the EDS analysis of the single crystals, it was concluded that, using the CVT method, pelletization of the finely ground starting materials is one of the necessary steps to obtain doped single crystals of $\text{Mo}_{1-x}\text{W}_x\text{Te}_2$ with the desired composition. XRD analysis of each sample suggested their single-crystalline nature with the exposed surface on the ab plane. The lattice parameter c calculated using XRD increases with increasing W content.

All of the single crystals showed metallic behavior in temperature-dependent resistivity measurements at ambient pressure. The RRR values of the doped single crystals were found to be low in comparison to the parent compounds, indicating that doping may cause impurities/defects in the crystals. Temperature-dependent resistivity measurements under magnetic fields showed large nonsaturating magnetoresistance (MR) behavior in the parent compounds, MoTe_2 and WTe_2 , when the magnetic and electric fields are perpendicular to each other. The observed maximum MR (2 K, 7 T) is $\sim 1650\%$ for MoTe_2 and $\sim 74000\%$ for WTe_2 . The large transverse MR behavior has been attributed to the electron-hole resonance. Although resistance slightly increases under magnetic field with $H \perp I$ in the doped compounds, the large nonsaturating MR behavior is absent. The MR (2 K, 7 T) increases with increasing W composition value from $\sim 6\%$ for $\text{Mo}_{0.90}\text{W}_{0.10}\text{Te}_2$ to $\sim 101\%$ for $\text{Mo}_{0.10}\text{W}_{0.90}\text{Te}_2$. Lower values of MR in the doped single crystals could be due to the electron-hole concentration asymmetry induced by doping.

Resistivity measurements of $\text{Mo}_{1-x}\text{W}_x\text{Te}_2$ for $x = 0, 0.10, 0.30, 0.50, 0.70, 0.90$, and 1 were conducted at ambient pressure and at temperatures up to 650 K. Based on the hysteresis observed in the resistivity data during the cooling and warming cycles, the structural phase diagram of $\text{Mo}_{1-x}\text{W}_x\text{Te}_2$ at ambient pressure has been constructed. The phase diagram shows that the structural transition temperature (T_s) increases linearly with increasing W content, which is due to enhancement in the kinetic energy of the system with W doping. By conducting temperature-dependent synchrotron XRD for WTe_2 , the structural transition was confirmed to be from the high-temperature monoclinic $1T'$ phase to the low-temperature orthorhombic T_d

phase.

High-pressure resistivity measurements of $\text{Mo}_{1-x}\text{W}_x\text{Te}_2$ for $x = 0.10, 0.40,$ and 0.75 up to 17 kbar were conducted using a BeCu clamp cell and the $T - P$ phase diagrams have been constructed. The study showed that with increasing pressure, the T_s decreases. When T_s is suppressed to < 175 K, superconductivity emerges, and as T_s is further suppressed, T_c sharply increases. Based on these results, we conclude that there is a competition between the structural transition and superconductivity. When pressure is applied, softening of the phonons occurs due the suppression of the Te-Te distances, which leads to the superconductivity in $\text{Mo}_{1-x}\text{W}_x\text{Te}_2$.

A diamond anvil cell (DAC) was used to study the magnetotransport properties of $\text{Mo}_{0.50}\text{W}_{0.50}\text{Te}_2$ under pressure and the phase diagram has been established. With increasing pressure, the transverse MR (10 K, 7 T) of $\text{Mo}_{0.50}\text{W}_{0.50}\text{Te}_2$ is suppressed, the Hall coefficient changes sign, and superconductivity emerges, suggesting a significant reconstruction of the Fermi surface.

There are numerous possibilities for future work studies of this family of compounds. For example, the structural behavior of $\text{Mo}_{1-x}\text{W}_x\text{Te}_2$ under pressure could be investigated. In order to understand the competition between the structural transition and superconductivity, theoretical study is required. Likewise, the Fermi surface reconstruction could be understood by performing theoretical calculations. Additionally, intercalating $\text{Mo}_{1-x}\text{W}_x\text{Te}_2$ with alkali metals like lithium (Li), sodium (Na), and potassium (K) could lead to new properties in these materials.

Appendix A

Superconductivity of Lead Under Pressure

The change in superconducting transition temperature (T_c) under pressure with respect to ambient pressure is given by [86]

$$\Delta T_c = T_c(0) - T_c(P), \quad (\text{A.1})$$

where $T_c(0)$ is T_c at ambient pressure and $T_c(P)$ is T_c under an unknown pressure. By knowing $T_c(0)$ and $T_c(P)$ of lead, ΔT_c can be calculated from which unknown pressure of the lead was determined using the Table A.1 or A.2.

Table A.1: Table showing change in superconducting transition temperature of lead under pressure.

T_c(K) of lead under pressure(kbar)

$$\Delta T_c = -3.689 \times 10^{-2} P + 1.026 \times 10^{-4} P^2$$

-ΔT _c	.000	.001	.002	.003	.004	.005	.006	.007	.008	.009
0.000	0.00	0.03	0.05	0.08	0.11	0.14	0.16	0.19	0.22	0.24
0.010	0.27	0.30	0.33	0.35	0.38	0.41	0.43	0.46	0.49	0.52
0.020	0.54	0.57	0.60	0.62	0.65	0.68	0.71	0.73	0.76	0.79
0.030	0.82	0.84	0.87	0.90	0.92	0.95	0.98	1.01	1.03	1.06
0.040	1.09	1.11	1.14	1.17	1.20	1.22	1.25	1.28	1.31	1.33
0.050	1.36	1.39	1.42	1.44	1.47	1.50	1.52	1.55	1.58	1.61
0.060	1.63	1.66	1.69	1.72	1.74	1.77	1.80	1.83	1.85	1.88
0.070	1.91	1.94	1.96	1.99	2.02	2.04	2.07	2.10	2.13	2.15
0.080	2.18	2.21	2.24	2.26	2.29	2.32	2.35	2.37	2.40	2.43
0.090	2.46	2.48	2.51	2.54	2.57	2.59	2.62	2.65	2.68	2.70
0.100	2.73	2.76	2.79	2.81	2.84	2.87	2.90	2.92	2.95	2.98
0.110	3.01	3.03	3.06	3.09	3.12	3.14	3.17	3.20	3.23	3.26
0.120	3.28	3.31	3.34	3.37	3.39	3.42	3.45	3.48	3.50	3.53
0.130	3.56	3.59	3.61	3.64	3.67	3.70	3.73	3.75	3.78	3.81
0.140	3.84	3.86	3.89	3.92	3.95	3.97	4.00	4.03	4.06	4.09
0.150	4.11	4.14	4.17	4.20	4.22	4.25	4.28	4.31	4.34	4.36
0.160	4.39	4.42	4.45	4.47	4.50	4.53	4.56	4.59	4.61	4.64
0.170	4.67	4.70	4.72	4.75	4.78	4.81	4.84	4.86	4.89	4.92
0.180	4.95	4.98	5.00	5.03	5.06	5.09	5.11	5.14	5.17	5.20
0.190	5.23	5.25	5.28	5.31	5.34	5.37	5.39	5.42	5.45	5.48
0.200	5.51	5.53	5.56	5.59	5.62	5.65	5.67	5.70	5.73	5.76
0.210	5.79	5.81	5.84	5.87	5.90	5.93	5.95	5.98	6.01	6.04
0.220	6.07	6.09	6.12	6.15	6.18	6.21	6.23	6.26	6.29	6.32
0.230	6.35	6.37	6.40	6.43	6.46	6.49	6.52	6.54	6.57	6.60
0.240	6.63	6.66	6.68	6.71	6.74	6.77	6.80	6.83	6.85	6.88
0.250	6.91	6.94	6.97	6.99	7.02	7.05	7.08	7.11	7.14	7.16
0.260	7.19	7.22	7.25	7.28	7.30	7.33	7.36	7.39	7.42	7.45
0.270	7.47	7.50	7.53	7.56	7.59	7.62	7.64	7.67	7.70	7.73
0.280	7.76	7.79	7.81	7.84	7.87	7.90	7.93	7.96	7.98	8.01
0.290	8.04	8.07	8.10	8.13	8.15	8.18	8.21	8.24	8.27	8.30
0.300	8.33	8.35	8.38	8.41	8.44	8.47	8.50	8.52	8.55	8.58
0.310	8.61	8.64	8.67	8.69	8.72	8.75	8.78	8.81	8.84	8.87
0.320	8.89	8.92	8.95	8.98	9.01	9.04	9.07	9.09	9.12	9.15
0.330	9.18	9.21	9.24	9.27	9.29	9.32	9.35	9.38	9.41	9.44
0.340	9.47	9.49	9.52	9.55	9.58	9.61	9.64	9.67	9.69	9.72
0.350	9.75	9.78	9.81	9.84	9.87	9.90	9.92	9.95	9.98	10.01
0.360	10.04	10.07	10.10	10.13	10.15	10.18	10.21	10.24	10.27	10.30
0.370	10.33	10.36	10.38	10.41	10.44	10.47	10.50	10.53	10.56	10.59
0.380	10.61	10.64	10.67	10.70	10.73	10.76	10.79	10.82	10.84	10.87
0.390	10.90	10.93	10.96	10.99	11.02	11.05	11.08	11.10	11.13	11.16
0.400	11.19	11.22	11.25	11.28	11.31	11.34	11.36	11.39	11.42	11.45
0.410	11.48	11.51	11.54	11.57	11.60	11.63	11.65	11.68	11.71	11.74
0.420	11.77	11.80	11.83	11.86	11.89	11.92	11.94	11.97	12.00	12.03
0.430	12.06	12.09	12.12	12.15	12.18	12.21	12.24	12.26	12.29	12.32
0.440	12.35	12.38	12.41	12.44	12.47	12.50	12.53	12.56	12.58	12.61
0.450	12.64	12.67	12.70	12.73	12.76	12.79	12.82	12.85	12.88	12.91
0.460	12.93	12.96	12.99	13.02	13.05	13.08	13.11	13.14	13.17	13.20
0.470	13.23	13.26	13.29	13.31	13.34	13.37	13.40	13.43	13.46	13.49
0.480	13.52	13.55	13.58	13.61	13.64	13.67	13.70	13.73	13.75	13.78
0.490	13.81	13.84	13.87	13.90	13.93	13.96	13.99	14.02	14.05	14.08
0.500	14.11	14.14	14.17	14.20	14.22	14.25	14.28	14.31	14.34	14.37
0.510	14.40	14.43	14.46	14.49	14.52	14.55	14.58	14.61	14.64	14.67
0.520	14.70	14.73	14.76	14.78	14.81	14.84	14.87	14.90	14.93	14.96
0.530	14.99	15.02	15.05	15.08	15.11	15.14	15.17	15.20	15.23	15.26
0.540	15.29	15.32	15.35	15.38	15.41	15.44	15.47	15.50	15.53	15.55
0.550	15.58	15.61	15.64	15.67	15.70	15.73	15.76	15.79	15.82	15.85

Table A.2: Table A.1 continued.

Tc(K) of lead under pressure(kbar)

$$\Delta T_c = -3.689 \times 10^{-2} P + 1.026 \times 10^{-4} P^2$$

$-\Delta T_c$.000	.001	.002	.003	.004	.005	.006	.007	.008	.009
0.560	15.88	15.91	15.94	15.97	16.00	16.03	16.06	16.09	16.12	16.15
0.570	16.18	16.21	16.24	16.27	16.30	16.33	16.36	16.39	16.42	16.45
0.580	16.48	16.51	16.54	16.57	16.60	16.63	16.66	16.69	16.72	16.75
0.590	16.78	16.81	16.84	16.87	16.90	16.93	16.96	16.99	17.02	17.05
0.600	17.08	17.11	17.14	17.17	17.20	17.23	17.26	17.29	17.32	17.35
0.610	17.38	17.41	17.44	17.47	17.50	17.53	17.56	17.59	17.62	17.65
0.620	17.68	17.71	17.74	17.77	17.80	17.83	17.86	17.89	17.92	17.95
0.630	17.98	18.01	18.04	18.07	18.10	18.13	18.16	18.19	18.22	18.25
0.640	18.28	18.31	18.34	18.37	18.40	18.43	18.46	18.49	18.52	18.55
0.650	18.58	18.61	18.64	18.67	18.70	18.73	18.76	18.79	18.82	18.85
0.660	18.88	18.91	18.94	18.97	19.00	19.03	19.06	19.09	19.13	19.16
0.670	19.19	19.22	19.25	19.28	19.31	19.34	19.37	19.40	19.43	19.46
0.680	19.49	19.52	19.55	19.58	19.61	19.64	19.67	19.70	19.73	19.76
0.690	19.79	19.82	19.85	19.89	19.92	19.95	19.98	20.01	20.04	20.07
0.700	20.10	20.13	20.16	20.19	20.22	20.25	20.28	20.31	20.34	20.37
0.710	20.40	20.43	20.47	20.50	20.53	20.56	20.59	20.62	20.65	20.68
0.720	20.71	20.74	20.77	20.80	20.83	20.86	20.89	20.92	20.96	20.99
0.730	21.02	21.05	21.08	21.11	21.14	21.17	21.20	21.23	21.26	21.29
0.740	21.32	21.35	21.39	21.42	21.45	21.48	21.51	21.54	21.57	21.60
0.750	21.63	21.66	21.69	21.72	21.76	21.79	21.82	21.85	21.88	21.91
0.760	21.94	21.97	22.00	22.03	22.06	22.09	22.13	22.16	22.19	22.22
0.770	22.25	22.28	22.31	22.34	22.37	22.40	22.44	22.47	22.50	22.53
0.780	22.56	22.59	22.62	22.65	22.68	22.71	22.75	22.78	22.81	22.84
0.790	22.87	22.90	22.93	22.96	22.99	23.02	23.06	23.09	23.12	23.15
0.800	23.18	23.21	23.24	23.27	23.30	23.34	23.37	23.40	23.43	23.46
0.810	23.49	23.52	23.55	23.59	23.62	23.65	23.68	23.71	23.74	23.77
0.820	23.80	23.83	23.87	23.90	23.93	23.96	23.99	24.02	24.05	24.09
0.830	24.12	24.15	24.18	24.21	24.24	24.27	24.30	24.34	24.37	24.40
0.840	24.43	24.46	24.49	24.52	24.56	24.59	24.62	24.65	24.68	24.71
0.850	24.74	24.78	24.81	24.84	24.87	24.90	24.93	24.96	25.00	25.03
0.860	25.06	25.09	25.12	25.15	25.19	25.22	25.25	25.28	25.31	25.34
0.870	25.37	25.41	25.44	25.47	25.50	25.53	25.56	25.60	25.63	25.66
0.880	25.69	25.72	25.75	25.79	25.82	25.85	25.88	25.91	25.94	25.98
0.890	26.01	26.04	26.07	26.10	26.13	26.17	26.20	26.23	26.26	26.29
0.900	26.32	26.36	26.39	26.42	26.45	26.48	26.51	26.55	26.58	26.61
0.910	26.64	26.67	26.71	26.74	26.77	26.80	26.83	26.86	26.90	26.93
0.920	26.96	26.99	27.02	27.06	27.09	27.12	27.15	27.18	27.22	27.25
0.930	27.28	27.31	27.34	27.38	27.41	27.44	27.47	27.50	27.54	27.57
0.940	27.60	27.63	27.66	27.70	27.73	27.76	27.79	27.82	27.86	27.89
0.950	27.92	27.95	27.98	28.02	28.05	28.08	28.11	28.14	28.18	28.21
0.960	28.24	28.27	28.31	28.34	28.37	28.40	28.43	28.47	28.50	28.53
0.970	28.56	28.60	28.63	28.66	28.69	28.72	28.76	28.79	28.82	28.85
0.980	28.89	28.92	28.95	28.98	29.02	29.05	29.08	29.11	29.14	29.18
0.990	29.21	29.24	29.27	29.31	29.34	29.37	29.40	29.44	29.47	29.50
1.000	29.53	29.57	29.60	29.63	29.66	29.70	29.73	29.76	29.79	29.83
1.010	29.86	29.89	29.92	29.96	29.99	30.02	30.05	30.09	30.12	30.15
1.020	30.18	30.22	30.25	30.28	30.31	30.35	30.38	30.41	30.44	30.48
1.030	30.51	30.54	30.57	30.61	30.64	30.67	30.71	30.74	30.77	30.80
1.040	30.84	30.87	30.90	30.93	30.97	31.00	31.03	31.07	31.10	31.13
1.050	31.16	31.20	31.23	31.26	31.29	31.33	31.36	31.39	31.43	31.46
1.060	31.49	31.52	31.56	31.59	31.62	31.66	31.69	31.72	31.76	31.79
1.070	31.82	31.85	31.89	31.92	31.95	31.99	32.02	32.05	32.08	32.12
1.080	32.15	32.18	32.22	32.25	32.28	32.32	32.35	32.38	32.41	32.45
1.090	32.48	32.51	32.55	32.58	32.61	32.65	32.68	32.71	32.75	32.78
1.100	32.81	32.85	32.88	32.91	32.95	32.98	33.01	33.04	33.08	33.11

Bibliography

- [1] B. Q. Lv, H. M. Weng, B. B. Fu, X. P. Wang, H. Miao, J. Ma, P. Richard, X. C. Huang, L. X. Zhao, G. F. Chen, Z. Fang, X. Dai, T. Qian, and H. Ding. Experimental discovery of Weyl semimetal TaAs. *Phys. Rev. X*, 5:031013, 2015.
- [2] S.-Y. Xu, I. Belopolski, N. Alidoust, M. Neupane, G. Bian, C. Zhang, R. Sankar, G. Chang, Z. Yuan, C.-C. Lee, S.-M. Huang, H. Zheng, J. Ma, D. S. Sanchez, B. Wang, A. Bansil, F. Chou, P. P. Shibayev, H. Lin, S. Jia, and M. Z. Hasan. Discovery of a Weyl fermion semimetal and topological Fermi arcs. *Science*, 349:613, 2015.
- [3] S.-Y. Xu, N. Alidoust, I. Belopolski, Z. Yuan, G. Bian, T.-R. Chang, H. Zheng, V. N. Strocov, D. S. Sanchez, G. Chang, C. Zhang, D. Mou, Y. Wu, L. Huang, C.-C. Lee, S.-M. Huang, B. Wang, A. Bansil, H.-T. Jeng, T. Neupert, A. Kaminski, H. Lin, S. Jia, and M. Z. Hasan. Discovery of a Weyl fermion state with Fermi arcs in niobium arsenide. *Nat. Phys.*, 11:748, 2015.
- [4] A. A. Burkov. Weyl metals. *Annu. Rev. Condens. Matter Phys.*, 9:359, 2018.
- [5] B. Yan and C. Felser. Topological materials: Weyl semimetals. *Annu. Rev. Condens. Matter Phys.*, 8:337, 2017.
- [6] M. Z. Hasan and C. L. Kane. Topological insulators. *Rev. Mod. Phys.*, 82:3045, 2010.
- [7] Z. K. Liu, B. Zhou, Y. Zhang, Z. J. Wang, H. M. Weng, D. Prabhakaran, S.-K. Mo, Z. X. Shen, Z. Fang, X. Dai, Z. Hussain, and Y. L. Chen. Discovery of a three-dimensional topological Dirac semimetal, Na₃Bi. *Science*, 343:864, 2014.
- [8] Q. Li, D. E. Kharzeev, C. Zhang, Y. Huang, I. Pletikosić, A. V. Fedorov, R. D. Zhong, J. A. Schneeloch, G. D. Gu, and T. Valla. Chiral magnetic effect in ZrTe₅. *Nat. Phys.*, 12:550, 2016.

- [9] M. Z. Hasan, S.-Y. Xu, I. Belopolski, and S.-M. Huang. Discovery of Weyl fermion semimetals and topological Fermi arc states. *Annu. Rev. Condens. Matter Phys.*, 8:289, 2017.
- [10] H. Weyl. Elektron und Gravitation. *I. Z. Phys.*, 56:330, 1929.
- [11] Y. Fukuda, T. Hayakawa, E. Ichihara, K. Inoue, K. Ishihara, H. Ishino, Y. Itow, T. Kajita, J. Kameda, S. Kasuga, K. Kobayashi, Y. Kobayashi, Y. Koshio, M. Miura, M. Nakahata, S. Nakayama, A. Okada, K. Okumura, N. Sakurai, M. Shiozawa, Y. Suzuki, Y. Takeuchi, Y. Totsuka, S. Yamada, M. Earl, A. Habig, E. Kearns, M. D. Messier, K. Scholberg, J. L. Stone, L. R. Sulak, C. W. Walter, M. Goldhaber, T. Barszczak, D. Casper, W. Gajewski, P. G. Halverson, J. Hsu, W. R. Kropp, L. R. Price, F. Reines, M. Smy, H. W. Sobel, M. R. Vagins, K. S. Ganezer, W. E. Keig, R. W. Ellsworth, S. Tasaka, J. W. Flanagan, A. Kibayashi, J. G. Learned, S. Matsuno, V. J. Stenger, D. Takekoshi, T. Ishii, J. Kanzaki, T. Kobayashi, S. Mine, K. Nakamura, K. Nishikawa, Y. Oyama, A. Sakai, M. Sakuda, O. Sasaki, S. Echigo, M. Kohama, A. T. Suzuki, T. J. Haines, E. Blaufuss, B. K. Kim, R. Sanford, R. Svoboda, M. L. Chen, Z. Conner, J. A. Goodman, G. W. Sullivan, J. Hill, C. K. Jung, K. Martens, C. Mauger, C. McGrew, E. Sharkey, B. Viren, C. Yanagisawa, W. Doki, K. Miyano, H. Okazawa, C. Saji, M. Takahata, Y. Nagashima, M. Takita, T. Yamaguchi, M. Yoshida, S. B. Kim, M. Etoh, K. Fujita, A. Hasegawa, T. Hasegawa, S. Hatakeyama, T. Iwamoto, M. Koga, T. Maruyama, H. Ogawa, J. Shirai, A. Suzuki, F. Tsushima, M. Koshihara, M. Nemoto, K. Nishijima, T. Futagami, Y. Hayato, Y. Kanaya, K. Kaneyuki, Y. Watanabe, D. Kielczewska, R. A. Doyle, J. S. George, A. L. Stachyra, L. L. Wai, R. J. Wilkes, and K. K. Young. Evidence for oscillation of atmospheric neutrinos. *Phys. Rev. Lett.*, 81:1562, 1998.
- [12] A. A. Soluyanov, D. Gresch, Z. Wang, Q. Wu, M. Troyer, X. Dai, and B. A. Bernevig. Type-II Weyl semimetals. *Nature (London)*, 527:495, 2015.
- [13] S.-Y. Xu, I. Belopolski, D. S. Sanchez, C. Zhang, G. Chang, C. Guo, G. Bian, Z. Yuan, H. Lu, T.-R. Chang, P. P. Shibayev, M. L. Prokopovych, N. Alidoust, H. Zheng, C.-C. Lee, S.-M. Huang, R. Sankar, F. Chou, C.-H. Hsu, H.-T. Jeng, A. Bansil, T. Neupert, V. N. Strocov, H. Lin, S. Jia, and M. Z. Hasan. Experimental discovery of a topological Weyl semimetal state in TaP. *Sci. Adv.*, 1:e1501092, 2015.
- [14] H. Weng, C. Fang, Z. Fang, B. A. Bernevig, and X. Dai. Weyl semimetal phase in noncentrosymmetric transition-metal monophosphides. *Phys. Rev. X*, 5:011029, 2015.

- [15] S.-M. Huang, S.-Y. Xu, I. Belopolski, C.-C. Lee, G. Chang, B. Wang, N. Alidoust, G. Bian, M. Neupane, C. Zhang, S. Jia, A. Bansil, H. Lin, and M. Z. Hasan. A Weyl Fermion semimetal with surface Fermi arcs in the transition metal monopnictide TaAs class. *Nat. Commun.*, 6:7373, 2015.
- [16] L. X. Yang, Z. K. Liu, Y. Sun, H. Peng, H. F. Yang, T. Zhang, B. Zhou, Y. Zhang, Y. F. Guo, M. Rahn, D. Prabhakaran, Z. Hussain, S.-K. Mo, C. Felser, B. Yan, and Y. L. Chen. Weyl semimetal phase in the non-centrosymmetric compound TaAs. *Nat. Phys.*, 11:728, 2015.
- [17] N. Xu, H. M. Weng, B. Q. Lv, C. E. Matt, J. Park, F. Bisti, V. N. Strocov, D. Gawryluk, E. Pomjakushina, K. Conder, N. C. Plumb, M. Radovic, G. Autès, O. V. Yazyev, Z. Fang, X. Dai, T. Qian, J. Mesot, H. Ding, and M. Shi. Observation of Weyl nodes and Fermi arcs in tantalum phosphide. *Nat. Commun.*, 7:11006, 2016.
- [18] D.-F. Xu, Y.-P. Du, Z. Wang, Y.-P. Li, X.-H. Niu, Q. Yao, D. Pavel, Z.-A. Xu, X.-G. Wan, and D.-L. Feng. Observation of Fermi arcs in non-centrosymmetric Weyl semi-metal candidate NbP. *Chin. Phys. Lett.*, 32:107101, 2015.
- [19] S. Souma, Z. Wang, H. Kotaka, T. Sato, K. Nakayama, Y. Tanaka, H. Kimizuka, T. Takahashi, K. Yamauchi, T. Oguchi, K. Segawa, and Y. Ando. Direct observation of nonequivalent Fermi-arc states of opposite surfaces in the noncentrosymmetric Weyl semimetal NbP. *Phys. Rev. B*, 93:161112(R), 2016.
- [20] Z. K. Liu, L. X. Yang, Y. Sun, T. Zhang, H. Peng, H. F. Yang, C. Chen, Y. Zhang, Y. F. Guo, D. Prabhakaran, M. Schmidt, Z. Hussain, S.-K. Mo, C. Felser, B. Yan, and Y. L. Chen. Evolution of the Fermi surface of Weyl semimetals in the transition metal pnictide family. *Nat. Mater.*, 15:27, 2016.
- [21] I. Belopolski, S.-Y. Xu, D. S. Sanchez, G. Chang, C. Guo, M. Neupane, H. Zheng, C.-C. Lee, S.-M. Huang, G. Bian, N. Alidoust, T.-R. Chang, B. Wang, X. Zhang, A. Bansil, H.-T. Jeng, H. Lin, S. Jia, and M. Z. Hasan. Criteria for directly detecting topological Fermi arcs in Weyl semimetals. *Phys. Rev. Lett.*, 116:066802, 2016.
- [22] M. Sakano, M. S. Bahramy, H. Tsuji, I. Araya, K. Ikeura, H. Sakai, S. Ishiwata, K. Yaji, K. Kuroda, A. Harasawa, S. Shin, and K. Ishizaka. Observation of spin-polarized bands and domain-dependent Fermi arcs in polar Weyl semimetal MoTe₂. *Phys. Rev. B*, 95:121101(R), 2017.
- [23] J. Jiang, Z. K. Liu, Y. Sun, H. F. Yang, C. R. Rajamathi, Y. P. Qi, L. X. Yang, C. Chen, H. Peng, C.-C. Hwang, S. Z. Sun, S.-K. Mo, I. Vobornik, J. Fujii,

- S. S. P. Parkin, C. Felser, B. H. Yan, and Y. L. Chen. Signature of type-II Weyl semimetal phase in MoTe₂. *Nat. Commun.*, 8:13973, 2017.
- [24] P. Li, Y. Wen, X. He, Q. Zhang, C. Xia, Z.-M. Yu, S. A. Yang, Z. Zhu, H. N. Alshareef, and X.-X. Zhang. Evidence for topological type-II Weyl semimetal WTe₂. *Nat. Commun.*, 8:2150, 2017.
- [25] Y.-Y. Lv, X. Li, B.-B. Zhang, W. Y. Deng, S.-H. Yao, Y. B. Chen, J. Zhou, S.-T. Zhang, M.-H. Lu, L. Zhang, M. Tian, L. Sheng, and Y.-F. Chen. Experimental observation of anisotropic Adler-Bell-Jackiw anomaly in type-II Weyl semimetal WTe_{1.98} crystals at the quasiclassical regime. *Phys. Rev. Lett.*, 118:096603, 2017.
- [26] X. Luo, F. C. Chen, J. L. Zhang, Q. L. Pei, G. T. Lin, W. J. Lu, Y. Y. Han, C. Y. Xi, W. H. Song, and Y. P. Sun. T_d-MoTe₂: A possible topological superconductor. *Appl. Phys. Lett.*, 109:102601, 2016.
- [27] M. N. Ali, J. Xiong, S. Flynn, J. Tao, Q. D. Gibson, L. M. Schoop, T. Liang, N. Haldolaarachchige, M. Hirschberger, N. P. Ong, and R. J. Cava. Large, non-saturating magnetoresistance in WTe₂. *Nature (London)*, 514:205, 2014.
- [28] I. Belopolski, D. S. Sanchez, Y. Ishida, X. Pan, P. Yu, S.-Y. Xu, G. Chang, T.-R. Chang, H. Zheng, N. Alidoust, G. Bian, M. Neupane, S.-M. Huang, C.-C. Lee, Y. Song, H. Bu, G. Wang, S. Li, G. Eda, H.-T. Jeng, T. Kondo, H. Lin, Z. Liu, F. Song, S. Shin, and M. Z. Hasan. Discovery of a new type of topological Weyl fermion semimetal state in Mo_xW_{1-x}Te₂. *Nat. Commun.*, 7:13643, 2016.
- [29] H. P. Hughes and R. H. Friend. Electrical resistivity anomaly in β -MoTe₂ (metallic behaviour). *J. Phys. C: Solid State Phys.*, 11:L103, 1978.
- [30] R. Clarke, E. Marseglia, and H. P. Hughes. A low-temperature structural phase transition in β -MoTe₂. *Philos. Mag. B*, 38:121, 1978.
- [31] Y. Qi, P. G. Naumov, M. N. Ali, C. R. Rajamathi, W. Schnelle, O. Barkalov, M. Hanfland, S.-C. Wu, C. Shekhar, Y. Sun, V. Süß, M. Schmidt, U. Schwarz, E. Pippel, P. Werner, R. Hillebrand, T. Förster, E. Kampert, S. Parkin, R. J. Cava, C. Felser, B. Yan, and S. A. Medvedev. Superconductivity in Weyl semimetal candidate MoTe₂. *Nat. Commun.*, 7:11038, 2016.
- [32] H. Takahashi, T. Akiba, K. Imura, T. Shiino, K. Deguchi, N. K. Sato, H. Sakai, M. S. Bahramy, and S. Ishiwata. Anticorrelation between polar lattice instability and superconductivity in the Weyl semimetal candidate MoTe₂. *Phys. Rev. B*, 95:100501(R), 2017.

- [33] C. Heikes, I.-L. Liu, T. Metz, C. Eckberg, P. Neves, Y. Wu, L. Hung, P. Piccoli, H. Cao, J. Leao, J. Paglione, T. Yildirim, N. P. Butch, and W. Ratcliff II. Mechanical control of crystal symmetry and superconductivity in Weyl semimetal MoTe₂. *Phys. Rev. Mater.*, 2:074202, 2018.
- [34] P. A. M. Dirac. The quantum theory of the electron. *Proc. R. Soc. Lond. A*, 117:610, 1928.
- [35] M. E. Peskin and D. V. Schroeder. *An introduction to quantum field theory*. Addison-Wesley Publishing Company, 1995.
- [36] X. Wan, A. M. Turner, A. Vishwanath, and S. Y. Savrasov. Topological semimetal and Fermi-arc surface states in the electronic structure of pyrochlore iridates. *Phys. Rev. B*, 83:205101, 2011.
- [37] A. A. Burkov and L. Balents. Weyl semimetal in a topological insulator multilayer. *Phys. Rev. Lett.*, 107:127205, 2011.
- [38] M. A. Silaev and G. E. Volovik. Topological Fermi arcs in superfluid ³He. *Phys. Rev. B*, 86:214511, 2012.
- [39] L. Balents. Weyl electrons kiss. *Physics*, 4:36, 2011.
- [40] P. Hosur. Friedel oscillations due to Fermi arcs in Weyl semimetals. *Phys. Rev. B*, 86:195102, 2012.
- [41] P. Hosur and X. Qi. Recent developments in transport phenomena in Weyl semimetals. *C. R. Phys.*, 14:857, 2013.
- [42] S. Kourtis, J. Li, Z. Wang, A. Yazdani, and B. A. Bernevig. Universal signatures of Fermi arcs in quasiparticle interference on the surface of Weyl semimetals. *Phys. Rev. B*, 93:041109(R), 2016.
- [43] A. C. Potter, I. Kimchi, and A. Vishwanath. Quantum oscillations from surface Fermi arcs in Weyl and Dirac semimetals. *Nat. Commun.*, 5:5161, 2014.
- [44] H. Inoue, A. Gyenis, Z. Wang, J. Li, S. W. Oh, S. Jiang, N. Ni, B. A. Bernevig, and A. Yazdani. Quasiparticle interference of the Fermi arcs and surface-bulk connectivity of a Weyl semimetal. *Science*, 351:1184, 2016.
- [45] R. Batabyal, N. Morali, N. Avraham, Y. Sun, M. Schmidt, C. Felser, A. Stern, B. Yan, and H. Beidenkopf. Visualizing weakly bound surface Fermi arcs and their correspondence to bulk Weyl fermions. *Sci. Adv.*, 2:e1600709, 2016.

- [46] C. Shekhar, A. K. Nayak, Y. Sun, M. Schmidt, M. Nicklas, I. Leermakers, U. Zeitler, Y. Skourski, J. Wosnitza, Z. Liu, Y. Chen, W. Schnelle, H. Borrmann, Y. Grin, C. Felser, and B. Yan. Extremely large magnetoresistance and ultrahigh mobility in the topological Weyl semimetal candidate NbP. *Nat. Phys.*, 11:645, 2015.
- [47] S. Parkin, X. Jiang, C. Kaiser, A. Panchula, K. Roche, and M. Samant. Magnetically engineered spintronic sensors and memory. *Proc. IEEE*, 91:661, 2003.
- [48] X. Huang, L. Zhao, Y. Long, P. Wang, D. Chen, Z. Yang, H. Liang, M. Xue, H. Weng, Z. Fang, X. Dai, and G. Chen. Observation of the chiral-anomaly-induced negative magnetoresistance in 3D Weyl semimetal TaAs. *Phys. Rev. X*, 5:031023, 2015.
- [49] F. Arnold, C. Shekhar, S.-C. Wu, Y. Sun, R. D. d. Reis, N. Kumar, M. Naumann, M. O. Ajeesh, M. Schmidt, A. G. Grushin, J. H. Bardarson, M. Baenitz, D. Sokolov, H. Borrmann, M. Nicklas, C. Felser, E. Hassinger, and B. Yan. Negative magnetoresistance without well-defined chirality in the Weyl semimetal TaP. *Nat. Commun.*, 7:11615, 2016.
- [50] N. J. Ghimire, Y. Luo, M. Neupane, D. J. Williams, E. D. Bauer, and F. Ronning. Magnetotransport of single crystalline NbAs. *J. Phys. Condens. Matter*, 27:152201, 2015.
- [51] J. Klotz, S.-C. Wu, C. Shekhar, Y. Sun, M. Schmidt, M. Nicklas, M. Baenitz, M. Uhlarz, J. Wosnitza, C. Felser, and B. Yan. Quantum oscillations and the Fermi surface topology of the Weyl semimetal NbP. *Phys. Rev. B*, 93:121105(R), 2016.
- [52] S. Murakami. Phase transition between the quantum spin Hall and insulator phases in 3D: emergence of a topological gapless phase. *New J. Phys.*, 9:356, 2007.
- [53] O. Vafek and A. Vishwanath. Dirac Fermions in solids: From high- T_c cuprates and graphene to topological insulators and Weyl semimetals. *Annu. Rev. Condens. Matter Phys.*, 5:83, 2014.
- [54] N. P. Armitage, E. J. Mele, and A. Vishwanath. Weyl and Dirac semimetals in three-dimensional solids. *Rev. Mod. Phys.*, 90:015001, 2018.
- [55] E. Haubold, K. Koepf, D. Efremov, S. Khim, A. Fedorov, Y. Kushnirenko, J. van den Brink, S. Wurmehl, B. Büchner, T. K. Kim, M. Hoesch, K. Sumida,

- K. Taguchi, T. Yoshikawa, A. Kimura, T. Okuda, and S. V. Borisenko. Experimental realization of type-II Weyl state in noncentrosymmetric TaIrTe₄. *Phys. Rev. B*, 95:241108(R), 2017.
- [56] J.A. Wilson and A.D. Yoffe. The transition metal dichalcogenides discussion and interpretation of the observed optical, electrical and structural properties. *Adv. Phys.*, 18:193, 1969.
- [57] Q. H. Wang, K. Kalantar-Zadeh, A. Kis, J. N. Coleman, and M. S. Strano. Electronics and optoelectronics of two-dimensional transition metal dichalcogenides. *Nat. Nanotechnol.*, 7:699, 2012.
- [58] A. D. Yoffe. Layer compounds. *Annu. Rev. Mater. Sci.*, 3:147, 1973.
- [59] R. C. Morris, R. V. Coleman, and R. Bhandari. Superconductivity and Magnetoresistance in NbSe₂. *Phys. Rev. B*, 5:895, 1972.
- [60] B. Sipoš, A. F. Kusmartseva, A. Akrap, H. Berger, L. Forró, and E. Tutiš. From Mott state to superconductivity in 1T-TaS₂. *Nat. Mater.*, 7:960, 2008.
- [61] B. W. H. Baugher, H. O. H. Churchill, Y. Yang, and P. Jarillo-Herrero. Optoelectronic devices based on electrically tunable p-n diodes in a monolayer dichalcogenide. *Nat. Nanotechnol.*, 9:262, 2014.
- [62] X. Qian, J. Liu, L. Fu, and J. Li. Quantum spin Hall effect in two-dimensional transition metal dichalcogenides. *Science*, 346:1344, 2014.
- [63] H. Katzke, P. Tolédano, and W. Depmeier. Phase transitions between polytypes and intralayer superstructures in transition metal dichalcogenides. *Phys. Rev. B*, 69:134111, 2004.
- [64] A. R. Beal and H. P. Hughes. Kramers-Kronig analysis of the reflectivity spectra of 2H-MoS₂, 2H-MoSe₂ and 2H-MoTe₂. *J. Phys. C: Solid State Phys.*, 12:881, 1979.
- [65] B. E. Brown. The crystal structures of WTe₂ and high-temperature MoTe₂. *Acta Crystallogr.*, 20:268, 1966.
- [66] T. Zandt, H. Dwelk, C. Janowitz, and R. Manzke. Quadratic temperature dependence up to 50 K of the resistivity of metallic MoTe₂. *J. Alloys Compd.*, 442:216, 2007.

- [67] J. E. Callanan, G. A. Hope, R. D. Weir, and E. F. Westrum. Thermodynamic properties of tungsten ditelluride (WTe_2) I. The preparation and low-temperature heat capacity at temperatures from 6 K to 326 K. *J. Chem. Thermodyn.*, 24:627, 1992.
- [68] F. Zhang, H. Zhang, S. Krylyuk, C. A. Milligan, Y. Zhu, D. Y. Zemlyanov, L.A. Bendersky, B. P. Burton, A. V. Davydov, and J. Appenzeller. Electric-field induced structural transition in vertical MoTe_2 - and $\text{Mo}_{1-x}\text{W}_x\text{Te}_2$ -based resistive memories. *Nat. Mater.*, 18:55, 2019.
- [69] R. Dahal, L. Z. Deng, N. Poudel, M. Gooch, Z. Wu, H. C. Wu, H. D. Yang, C. K. Chang, and C. W. Chu. Tunable structural phase transition and superconductivity in the Weyl semimetal $\text{Mo}_{1-x}\text{W}_x\text{Te}_2$. *Phys. Rev. B*, 101:140505(R), 2020.
- [70] Z. Fei, T. Palomaki, S. Wu, W. Zhao, X. Cai, B. Sun, P. Nguyen, J. Finney, X. Xu, and D. H. Cobden. Edge conduction in monolayer WTe_2 . *Nat. Phys.*, 13:677, 2017.
- [71] E. Sajadi, T. Palomaki, Z. Fei, W. Zhao, P. Bement, C. Olsen, S. Luescher, X. Xu, J. A. Folk, and D. H. Cobden. Gate-induced superconductivity in a monolayer topological insulator. *Science*, 362:922, 2018.
- [72] X.-C. Pan, X. Chen, H. Liu, Y. Feng, Z. Wei, Y. Zhou, Z. Chi, L. Pi, F. Yen, F. Song, X. Wan, Z. Yang, B. Wang, G. Wang, and Y. Zhang. Pressure-driven dome-shaped superconductivity and electronic structural evolution in tungsten ditelluride. *Nat. Commun.*, 6:7805, 2015.
- [73] Y.-Y. Lv, L. Cao, X. Li, B.-B. Zhang, K. Wang, B. Pang, L. Ma, D. Lin, S.-H. Yao, J. Zhou, Y. B. Chen, S.-T. Dong, W. Liu, M.-H. Lu, Y. Chen, and Y.-F. Chen. Composition and temperature-dependent phase transition in miscible $\text{Mo}_{1-x}\text{W}_x\text{Te}_2$ single crystals. *Sci. Rep.*, 7:44587, 2017.
- [74] W. G. Dawson and D. W. Bullett. Electronic structure and crystallography of MoTe_2 and WTe_2 . *J. Phys. C: Solid State Phys.*, 20:6159, 1987.
- [75] S. M. Oliver, R. Beams, S. Krylyuk, I. Kalish, A. K. Singh, A. Bruma, F. Tavazza, J. Joshi, I. R. Stone, S. J. Stranick, A. V. Davydov, and P. M. Vora. The structural phases and vibrational properties of $\text{Mo}_{1-x}\text{W}_x\text{Te}_2$ alloys. *2D Mater.*, 4:045008, 2017.
- [76] X.-J. Yan, Y.-Y. Lv, L. Li, X. Li, S.-H. Yao, Y.-B. Chen, X.-P. Liu, H. Lu, M.-H. Lu, and Y.-F. Chen. Composition dependent phase transition and its induced

hysteretic effect in the thermal conductivity of $W_x\text{Mo}_{1-x}\text{Te}_2$. *Appl. Phys. Lett.*, 110:211904, 2017.

- [77] D. Kang, Y. Zhou, W. Yi, C. Yang, J. Guo, Y. Shi, S. Zhang, Z. Wang, C. Zhang, S. Jiang, A. Li, K. Yang, Q. Wu, G. Zhang, L. Sun, and Z. Zhao. Superconductivity emerging from a suppressed large magnetoresistant state in tungsten ditelluride. *Nat. Commun.*, 6:7804, 2015.
- [78] Y. Zhou, X. Chen, N. Li, R. Zhang, X. Wang, C. An, Y. Zhou, X. Pan, F. Song, B. Wang, W. Yang, Z. Yang, and Y. Zhang. Pressure-induced Td to 1T' structural phase transition in WTe_2 . *AIP Adv.*, 6:075008, 2016.
- [79] P. Lu, J.-S. Kim, J. Yang, H. Gao, J. Wu, D. Shao, B. Li, D. Zhou, J. Sun, D. Akinwande, D. Xing, and J.-F. Lin. Origin of superconductivity in the Weyl semimetal WTe_2 under pressure. *Phys. Rev. B*, 94:224512, 2016.
- [80] J.-Q. Yan. Flux growth utilizing the reaction between flux and crucible. *J. Cryst. Growth*, 416:62, 2015.
- [81] P. C. Canfield and Z. Fisk. Growth of single crystals from metallic fluxes. *Philos. Mag. B*, 65:1117, 1992.
- [82] J. Yang, J. Colen, J. Liu, M. C. Nguyen, G.-w. Chern, and D. Louca. Elastic and electronic tuning of magnetoresistance in MoTe_2 . *Sci. Adv.*, 3:eaao4949, 2017.
- [83] E. J. Sie, C. M. Nyby, C. D. Pemmaraju, S. J. Park, X. Shen, J. Yang, M. C. Hoffmann, B. K. Ofori-Okai, R. Li, A. H. Reid, S. Weathersby, E. Mannebach, N. Finney, D. Rhodes, D. Chenet, A. Antony, L. Balicas, J. Hone, T. P. Devereaux, T. F. Heinz, X. Wang, and A. M. Lindenberg. An ultrafast symmetry switch in a Weyl semimetal. *Nature (London)*, 565:61, 2019.
- [84] M. Binnewies, R. Glaum, M. Schmidt, and P. Schmidt. *Chemical vapor transport reactions*. Walter de Gruyter, Berlin/Boston, 2012.
- [85] P. Schmidt, M. Binnewies, R. Glaum, and M. Schmidt. *Chemical vapor transport reactions—methods, materials, modeling*. InTech Rijeka, Croatia, 2013.
- [86] A. Eichler and J. Wittig. Pressure dependence of the superconducting transition temperature of lead. *Z. Angew. Phys.*, 25:319, 1968.
- [87] L. J. van der Pauw. A method of measuring the resistivity and Hall coefficient on lamellae of arbitrary shape. *Philips Tech. Rev.*, 20:220, 1958.

- [88] K. Ikeura, H. Sakai, M. S. Bahramy, and S. Ishiwata. Rich structural phase diagram and thermoelectric properties of layered tellurides $\text{Mo}_{1-x}\text{Nb}_x\text{Te}_2$. *APL Mater.*, 3:041514, 2015.
- [89] R. D. Shannon. Revised effective ionic radii and systematic studies of interatomic distances in halides and chalcogenides. *Acta Crystallogr. A*, 32:751, 1976.
- [90] Y.-Y. Lv, B.-B. Zhang, X. Li, B. Pang, F. Zhang, D.-J. Lin, J. Zhou, S.-H. Yao, Y. B. Chen, S.-T. Zhang, M. Lu, Z. Liu, Y. Chen, and Y.-F. Chen. Dramatically decreased magnetoresistance in non-stoichiometric WTe_2 crystals. *Sci. Rep.*, 6:26903, 2016.
- [91] J. M. Ziman. *Electrons and phonons*. Oxford University Press, London, 1960.
- [92] Y. Luo, H. Li, Y. M. Dai, H. Miao, Y. G. Shi, H. Ding, A. J. Taylor, D. A. Yarotski, R. P. Prasankumar, and J. D. Thompson. Hall effect in the extremely large magnetoresistance semimetal WTe_2 . *Appl. Phys. Lett.*, 107:182411, 2015.
- [93] Y. J. Hu, Y. T. Chan, K. T. Lai, K. O. Ho, X. Guo, H.-P. Sun, K. Y. Yip, D. H. L. Ng, H.-Z. Lu, and S. K. Goh. Angular dependence of the upper critical field in the high-pressure $1T'$ phase of MoTe_2 . *Phys. Rev. Mater.*, 3:034201, 2019.
- [94] H.-J. Kim, S.-H. Kang, I. Hamada, and Y.-W. Son. Origins of the structural phase transitions in MoTe_2 and WTe_2 . *Phys. Rev. B*, 95:180101(R), 2017.
- [95] R. C. Dynes. McMillan's equation and the T_c of superconductors. *Solid State Commun.*, 10:615, 1972.